CHALMERS
UNIVERSITY OF TECHNOLOGY

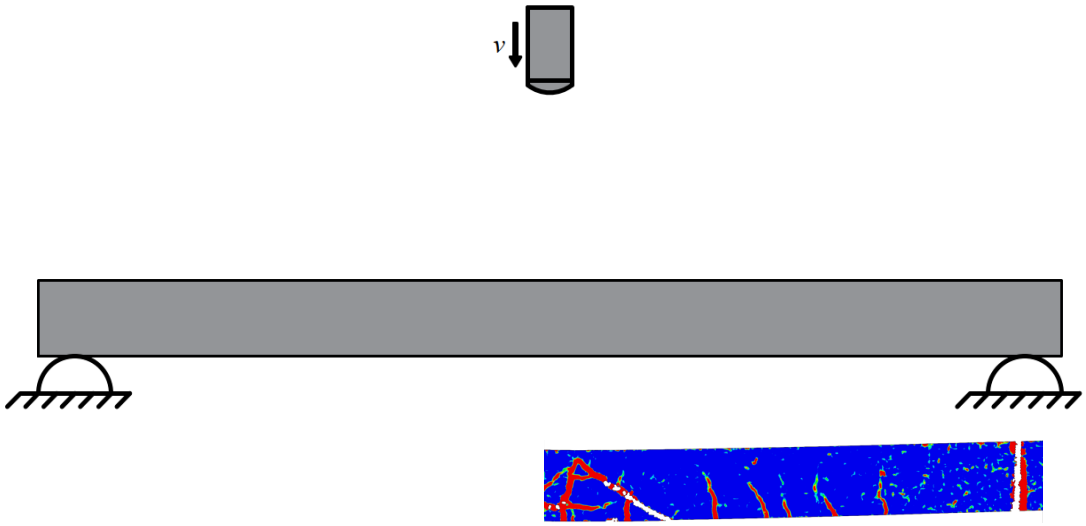

Reinforced Concrete Beams Subjected to Repeated Drop-Weight Impact and Static Load

Master's thesis in the Master's Programme Structural Engineering and Building Technology

SEBASTIAN SYVERSEN
CHRISTER TRINH

DEPARTMENT OF ARCHITECTURE AND CIVIL ENGINEERING
DIVISION OF STRUCTURAL ENGINEERING

CHALMERS UNIVERSITY OF TECHNOLOGY
Gothenburg, Sweden 2023
www.chalmers.se

MASTER'S THESIS ACEX30

Reinforced Concrete Beams Subjected to Repeated Drop-Weight Impact and Static Load

Master's Thesis in the Master's Programme Structural Engineering and Building Technology

SEBASTIAN SYVERSEN
CHRISTER TRINH

Department of Architecture and Civil Engineering
Division of Structural Engineering
Concrete Structure
CHALMERS UNIVERSITY OF TECHNOLOGY
Göteborg, Sweden 2023

Reinforced Concrete Beams Subjected to Repeated Drop-Weight Impact and Static Load

Master's Thesis in the Master's Programme Structural Engineering and Building Technology

SEBASTIAN SYVERSEN

CHRISTER TRINH

Examensarbete ACEX30
Institutionen för arkitektur och samhällsbyggnadsteknik
Chalmers tekniska högskola, 2023

Department of Architecture and Civil Engineering
Division of Structural Engineering
Concrete Structures
Chalmers University of Technology
SE-412 96 Göteborg
Sweden
Telephone: + 46 (0)31-772 1000

Cover:
Strain fields of a reinforced concrete beams that is subjected to a drop-weight impact.

Chalmers Reproservice
Göteborg, Sweden, 2023

Reinforced Concrete Beams Subjected to Repated Drop-Weight Impacts and Static Load

Master's thesis in the Master's Programme Structural Engineering and Building Technology

SEBASTIAN SYVERSEN

CHRISTER TRINH

Department of Architecture and Civil Engineering
Division of Structural Engineering
Concrete Structures
Chalmers University of Technology

ABSTRACT

When it comes to the structural response of reinforcement concrete beams (RC-beams) subjected to impulse loading, a high energy absorption and large plastic deformation capacity is of interest and not necessarily the load capacity that is of interest like it is for statically loaded structures. The aim of this thesis is to deepen the knowledge of the structural response of RC-beams subjected to single and repeated loading. The RC-beams were subjected to single and repeated loading with different drop-weights of 10, 20 and 40 kg from a height of 5 meter. The beams also had different reinforcement diameters of 6, 8 and 10 mm to test how it affects the structural response. The dynamically tested beams were also tested statically to determine the residual capacity. These were then compared to undamaged RC-beams that were statically tested to evaluate any dissimilarities.

A literature study was conducted to understand the structural response of the reinforced concrete beams. The study contained load capacity, plastic rotation capacity, internal work, and deflection of the reinforced concrete beams. The experiments on the beams were performed at Chalmers Laboratory, where the response of the RC-beams was captured with a high-speed camera and analysed with Digital Image Correlation (DIC) both statically and dynamically. Afterwards, the plastic rotation capacity and internal work was determined and compared to the predicted response.

When the beams were subjected to repeated impulse loading, major damage and localized spalling occurred. The excessive damage and spalling made the capturing of the beams using DIC incredibly difficult and it was difficult to compare to hand calculations. The experimental results showed good correlations to the predicted response. However, there were some deviations in some instances, it is difficult to compare and calculate when the RC-beams were subjected to multiple impacts, although it worked well for a singular impact.

Keywords: Reinforced concrete beams, drop-weight impact, repeated impact loading, 2DOF, internal work, plastic deformation, load capacity, plastic rotation capacity, impact loading, static loading, Digital Image Correlation, DIC.

Armerad betongbalkar utsatta för upprepande fallviktsförsök och statisk belastning

Examensarbete inom mastersprogrammet Konstruktionsteknik och byggnadsteknologi

SEBASTIAN SYVERSEN

CHRISTER TRINH

Institutionen för arkitektur och samhällsbyggnadsteknik
Avdelningen för Konstruktionsteknik
Betongbyggnad
Chalmers tekniska högskola

SAMMANFATTNING

När det kommer till den strukturella responsen hos armerade betongbalkar utsatta för impulsbelastning är hög energiabsorption och stor plastisk deformationskapacitet av stort intresse, och det är inte nödvändigtvis lastkapaciteten som är av intresse, som det är för statiskt belastade strukturer.

Syftet med detta examensarbete är att fördjupa förståelsen om den strukturella responsen hos armerade betongbalkar som utsätts för enskild och upprepad belastning. Armerade betongbalkar utsattes för enskilda och upprepade belastningar med olika fallvikter på 10, 20 och 40 kg från en fallhöjd på 5 meter. Balkarna hade också olika armeringsdiametrar på 6, 8 och 10 mm för att undersöka påverkan på den strukturella responsen. De dynamisk belastade balkarna provades också statiskt för att utvärdera residual-kapaciteten, vilka jämfördes med oskadade armerade betongbalkar som provades endast för statisk att utvärdera eventuella skillnader.

En litteraturstudie genomfördes för att förstå den strukturella responsen hos armerade betongbalkar. Studien omfattade lastkapacitet, plastisk rotationskapacitet, inre arbete och nedböjningar av armerade betongbalkar. Experimenten på balkarna utfördes vid Chalmers konstruktions laboratorium, där responsen hos armerade betongbalkarna fångades med en höghastighetskamera och analyserades med sk. ”Digital Image Correlation” (DIC) både statiskt och dynamiskt. Därefter bestämdes plastisk rotationskapacitet och inre arbete, vilka jämfördes med den predikterade responsen.

När balkarna utsattes för upprepad impulsbelastning uppstod stora skador och lokal spjälkning på balkarna. De omfattande skadorna och spjälkningarna gjorde det mycket svårt att analysera balkarna med DIC vilket medförde att det var svårt att jämföra försöktresultaten med handberäkningar. De experimentella resultaten visade en god korrelation med prediktionerna. Det fanns dock vissa avvikelser, det är svårt att jämföra och beräkna när armerade betongbalkar utsätts för upprepade stötar, även om det fungerar bra för ett enskilt fall.

Nyckelord: Armerade betongbalkar, stötbelastning, upprepad stötbelastning, 2DOF, inre arbete, plastisk deformation, lastkapacitet, plastisk rotationskapacitet, statisk belastning, stötlast, Digital Image Correlation, DIC

Contents

Preface

In this master thesis reinforced concrete beams subjected to single and repeated impact loading has been carried out together with subsequent static loading. The experiments were performed under different load conditions to investigate the effect of reinforcement, drop-weight mass, number of impacts and residual capacity on the beams.

The work was carried out between January and June 2023 at Chalmers and Norconsult in Gothenburg. This thesis is part of an ongoing research project in collaboration between Structural Engineering at Chalmers University of Technology and Norconsult. This project has been financed by the Swedish Civil Contingencies Agency and the Swedish Fortifications Agency. The project was supervised by Ph.D Morgan Johansson and examined by Ph.D Joosef Leppänen.

We would like to express our deepest gratitude to Morgan Johansson for his valuable guidance, knowledge, and participation during thesis. We also want to express our deepest gratitude to Joosef Leppänen for his helpful guidance and knowledge and participation during thesis. Further, we want to thank Research Engineers Sebastian Almfeldt and Anders Karlsson for their guidance and assistance during thesis.

Notations

Abbrevations

2DOF	Two-degree of freedom
SDOF	Single-degree of freedom
DIC	Digital image correlation
DIF	Dynamic increase factor
EC	Eurocode
FPS	Frames per second
RC	Reinforced concrete
ULS	Ultimate limit state
WST	Wedge splitting test

Roman upper case letters

A	Area
E	Young´s modulus
E_k	Kinetic Energy
F	Force, Load
$F_{dynamic}$	Dynamic load
F_{static}	Static Load
G_k	Fracture Energy
I	Impulse, First moment of inertia
I_I	Second moment of Inertia
L	Length
M	Moment
R	Internal resistance
R_m	Maximum internal resistance
V	Shear force
W	Work
W_e	External work
W_i	Internal work

Roman lower case letters

a	Acceleration
b	Width of cross-section

c	Dampening coefficient, Concrete cover thickness
d	Effective height cross-section
$f_{0.2}$	0.2% proof stress for the reinforcement steel
f_c	Cylinder compression strength of concrete
f_{ck}	Characteristic cylinder compression strength of concrete
f_{cm}	Mean cylinder compression strength of concrete
$f_{cm,cube}$	Mean cube compression strength of concrete
f_{ct}	Tensile strength of concrete
$f_{ctk0,05}$	Tensile strength; lower characteristic value
$f_{ctk0,95}$	Tensile strength; upper characteristic value
f_{ctm}	Mean tensile strength of concrete
$f_{ct,fl}$	Flexural tensile strength of concrete
$f_{ct,sp}$	Splitting tensile strength of concrete
f_t	Tensile strength of reinforcing steel
g	Gravitational constant
h	Height of beam cross-section, drop-height
k	Linear elastic constant
k_λ	Factor for plastic rotation according to Eurocode
l	Distance along beam
l_0	Distance from zero moment section to point of maximum moment
l_{pl}	Equivalent plastic hinge length
l_y	Length of plastic region
m	Mass
n	Number
p	Momentum of a particle
r	Radius of curvature
t	Time
u	Deflection or deformation
u_{cr}	Deflection or deformation when cracking occurs
u_F	Deflection or deformation under applied force
u_s	Deflection or system point
$\dot{u}$	First time derivative of displacement (velocity)
$\ddot{u}$	Second time derivative of displacement (acceleration)
v	Velocity

x	Distance to neutral axis from top edge
x_0	Distance from zero moment section to point of maximum moment after plastic redistribution

Greek letters

α_R	Stress block factor for average stress
β_R	Stress block factor for resultant location
δ	Displacement
$\dot{\varepsilon}$	Rate of strain
ε	Strain
ε_{cc}	Concrete strain; compression
ε_{ct}	Concrete strain; tension
ε_{cs}	Concrete strain at reinforcing steel
φ	Curvature
κ	Transformation factor
λ	Slenderness
ω	Angular eigenfrequency
ω_{bal}	Balanced mechanical reinforcement ratio
ω_s	Mechanical ratio of tensile reinforcement
$\omega_{s,crit}$	Critical mechanical ratio
ω_s'	Mechanical ratio of compression reinforcement
ϕ	Angle
ρ	Reinforcement ratio parameter, density
σ	Stress
θ	Rotation
$\theta_{pl,x\%}$	Plastic rotation at a given load level

Index

0	Initial
b	Beam
d	Design value
f	Field
imp	Impact
k	Characteristic value
m	Mean value

mid	Midpoint
s	Reinforcing steel
$support$	Support
u	Ultimate value
y	Yield value
el	Elastic
pl	Plastic
$relative$	relative
tot	Total
$'$	Compressive zone
I	State I
II	State II
cr	Cracking
max	Maximum value

1 INTRODUCTION

1.1 Background

Concrete structures that are affected by impulse loading is of interest when determining the structural response of protective structures. The impulse load could be in the form of an explosive load or an impact load from a collision. The structure that is subjected to this type of loading will generally have a different response compared to static loading. To determine the response of a structure subjected to impulse loading, energy equilibrium is used instead of force equilibrium, which is used for static loading. Consequently, using a structure with a large plastic deformation capacity may be preferable compared to using a structure with a large load resistance. This also means that a structure which is suitable to withstand static loading may not be as suitable to withstand the effects of an impulse load. Protective structures can also be subjected to repeated loading, which may result in different failure modes compared to when subjected to a single load. For these reasons understanding the structural response of impulse loading and repeating loading is of interest.

This master thesis is part of an ongoing research field by Swedish Civil Contingencies, Swedish Fortification Agency and the Division of structural engineering at Chalmers University of Technology. This is a continuation of previous master thesis carried out during 2016-2021 and is carried out in collaboration between Chalmers and Norconsult.

1.2 Aim

The aim of this master's thesis is to develop further understanding of how single and repeated impulse loading affects the structural response of concrete structures. Further, the plastic deformation capacity is of interest in the form of energy absorption.

Another aim of this master thesis is to summarize and compare the results of this project with previous similar projects that were carried out at Chalmers between 2016 and 2021.

1.3 Methodology

First, a literature study was performed to gain and then further develop knowledge of the given subject. It contains a survey of theoretical models which explains how to predict the structural response of a beam that is subjected to impact loading and its plastic deformation capacity. Previously written master theses were also studied to get an overview of the structural response in concrete that is subjected to impact loading.

Second, 18 reinforced concrete beams were casted and then harden at least for 28 days prior to testing. Both the concrete and the reinforcement's mechanical properties were evaluated according to standardized tests. The concrete was tested in compression and a wedge splitting test was performed to obtain the fracture energy i.e., to determine the amount of energy needed to fully develop a crack. However, the steel reinforcement was only tested for its tensile capacity.

Third, there were experimental tests done on 18 concrete specimens with varying reinforcement configuration. 12 specimens were tested subjected to single or repeated drop-weight impacts and the residual response was evaluated by subsequent static loading. High-speed cameras were used to capture the development of cracks and deformations in the impact loaded beams. The gathered information was evaluated using digital image correlation (DIC) to obtain parameters related to the structural response. The residual capacities were evaluated on the dynamically tested beams and compared to beams tested statically only. In addition, the static results from the experiments were also compared to the results from previous master theses.

Additionally, the thesis contains a comparison between the experimental results and the predicted response, where the predicted response is performed by using simplified dynamic calculation models in conjunction with a 2DOF system.

1.4 Limitations

This thesis is focused on investigating the dynamic response of a reinforced concrete beam subjected to single and repeated impact loading. However, static loading is also performed on the beams to investigate the residual plastic response. Only simply supported beams with longitudinal reinforcement is studied in the experiment. The beams are subjected to a concentrated load in the midspan with weights of 40 kg, 20 kg, and 10 kg, furthermore, these beams were tested with 6, 5, 4, 2 or 1 impacts of a steel cylinder dropped from a height of 5 m. The number of beams is limited to 18 beams with varying reinforcement diameters of 10 mm, 8 mm, and 6 mm. Thus, any weights, different numbers of impacts and other reinforcement diameters beyond this scope were not treated.

The expected failure mode of the beams in the experiment is bending failure. Consequently, the shear failure of the beams were believed not to be critical and was a reason why transversal stirrups were not used in the manufacturing.

2 MATERIALS

2.1 Concrete

2.1.1 Introduction

Concrete is a composite material consisting of cement, aggregates, and water (Al-Emrani et al., 2013). The typical properties of interest in concrete are the behaviour in tension and compression. The strength in tension is significantly lower than the strength in compression which can be seen in Figure 2.1.

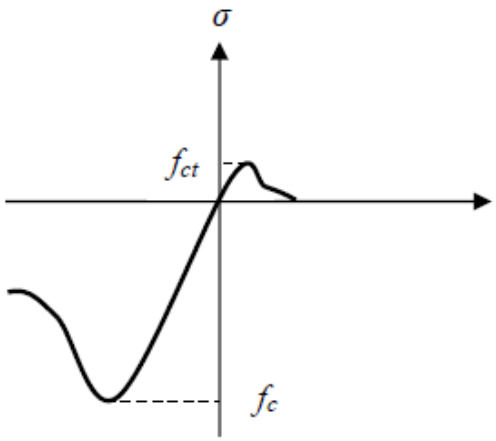

Figure 2.1 *The stress-strain relation for concrete subjected to uniaxial loading where f_c is the compressive strength and f_{ct} is the tensile strength* (Al-Emrani et al., 2013).

2.1.2 Compressive Strength

The compressive strength of concrete is determined by a standardized procedure using either concrete cylinders or cube specimens under uniaxial loading (Al-Emrani et al., 2013). The strength of concrete is obtained after 28 days where factors that influence the result, like specimen manufacturing, specimen placement, and test machine are regulated. In Sweden is it more common to use cubes during testing compared to cylinder specimens. The strength of cubes is approximately 1.2 larger compared to the strength of cylindrical testing, the relation between these can be expressed as

$$f_{cm} = \frac{f_{cm,cube}}{1.20} \tag{2.1}$$

where f_{cm} is the mean value of the compressive strength of a cylinder
$f_{cm,cube}$ is the mean value of the compressive strength of a cube

A stress-strain relation for concrete illustrated in Figure 2.2 can be obtained from material tests by measuring the compression force and the deformation. This illustrates a concrete specimen with different strengths subjected to compressive force. The concrete specimens with lower strength will have larger deformation after maximum stress which results in a more ductile response. Conversely concrete with high

compressive strength have a smaller deformation after maximum stress which results in a more brittle response. The ductile and brittle responses are further examined in Section 3.5.

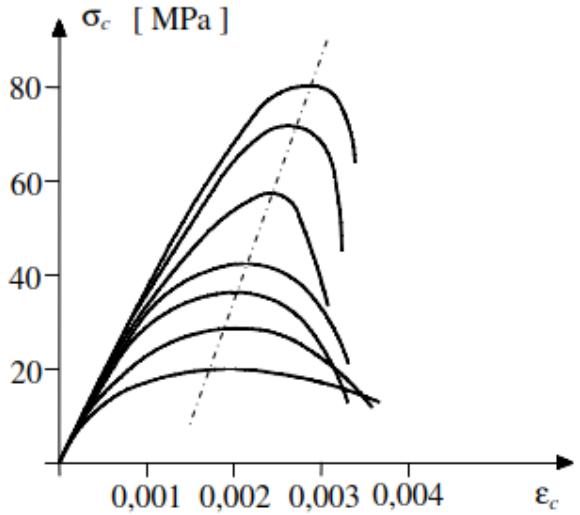

Figure 2.2 *The stress-strain relation for concrete of different strengths subjected to compression* (Al-Emrani et al., 2013).

The compressive strength is also determined by the loading rate where a concrete specimen subjected to a load during a short duration (high load rate) will result in higher concrete strength compared to a specimen in which the load is applied during a long duration (slow load rate). For long load duration, deformations increase with creep and the stress-strain curve becomes more elongated and flattened. This loading rate response of concrete is illustrated in Figure 2.3.

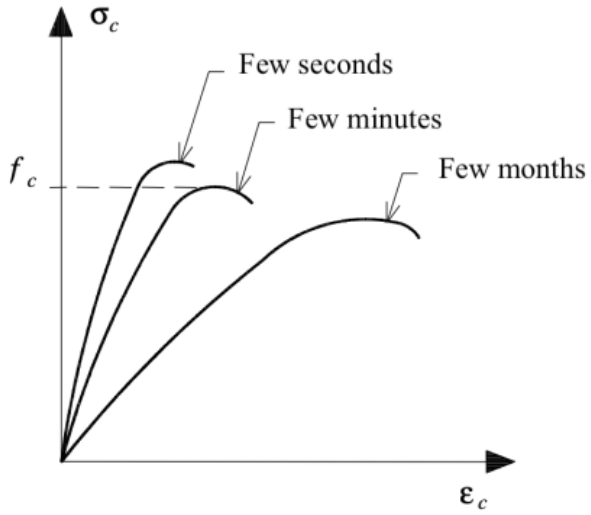

Figure 2.3 *Stress-strain relations for concrete subjected to varying load rates* (Al-Emrani et al., 2013).

2.1.3 Tensile Strength

The tensile strength of concrete can be determined by pure tensioning, splitting, or flexure test Al-Emrani et al., 2013). The result for tensile strength can vary depending on the method used but also if the specimen is of high-performance concrete when tested in pure tensioning. Generally, it is difficult to determine the tensile strength in pure tensioning test. Normally the tensile strength is determined by measuring the compression strength of the concrete and converting it to characteristic tensile strength. According to (CEN, 2005) the mean tensile strength is determined at 28 days from the characteristic compressive strength.

$$f_{ctm} = 0.3 \cdot (f_{ck})^{\frac{2}{3}}, \text{ (for concrete classes} \leq \text{C50/60)} \tag{2.2}$$

$$f_{ctm} = 2.12 \cdot \ln\left(1 + \frac{f_{ck}+8}{10}\right), \text{ (for concrete classes > C50/60)} \tag{2.3}$$

$$f_{ctk0.05} = 0.7 \cdot f_{ctm} \tag{2.4}$$

$$f_{ctk0.95} = 1.3 \cdot f_{cm} \tag{2.5}$$

where $f_{ck} = f_{cm} - 8$ [MPa] is the characteristic compressive strength
f_{ctm} is the mean concrete tensile strength

The mean tensile strength can also be determined by a splitting test:

$$f_{ctm} = 0.9 \cdot f_{ct.sp} \tag{2.6}$$

where $f_{ct.sp}$ is the mean tensile strength determined by splitting test.

Furthermore, the mean tensile strength can be determined by the flexural test, expressed as

$$f_{ctm.fl} = k \cdot f_{ctm} \tag{2.7}$$

where $k = 1.6 - \frac{h}{1000} \geq 1.0$ (with the height, h in [mm])

2.1.4 Modulus of Elasticity

The modulus of elasticity can be determined either by a more accurate method based on the stress-strain relationship of concrete or an approximate method (Al-Emrani et al., 2013). The accurate method is only recommended to use for non-linear structural analysis. In the approximated method, modulus of elasticity can be derived as secant modulus between $\sigma_c = 0$ and $\sigma_c = 0.4 \cdot f_{cm}$, see Figure 2.4. The approximated mean modulus of elasticity can be determined with Equation (2.8).

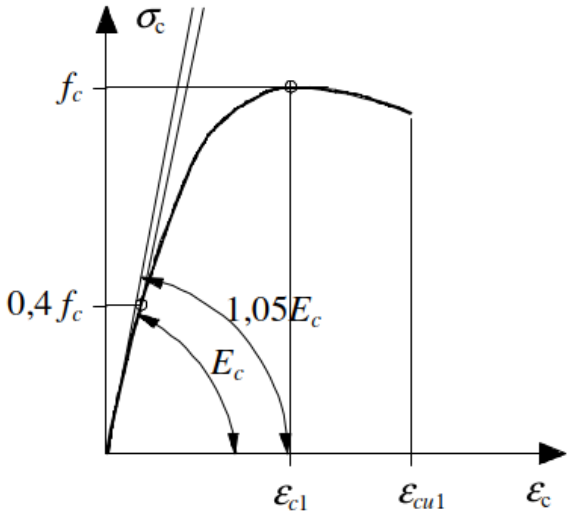

Figure 2.4 *Idealised stress-strain curve for concrete under compression according to EC2* (Al-Emrani et al., 2013).

$$E_{cm} = 22 \cdot \left(\frac{f_{cm}}{10}\right)^{0.3} \tag{2.8}$$

where f_{cm} = the mean compressive strength [MPa]

2.2 Reinforcing Steel

As previously stated in Section 2.1, concrete has a low tensile strength thus, steel reinforcement is used since it has a high tensile strength. Therefore, the steel reinforcement behaviour under tension is of relevance.

According to Engström (2015) reinforcement steel is classified according to several properties such as: strength, fatigue strength, ductility class, size, bendability, weldability etc. Where the most important property for this thesis is the ductility class, since a more ductile response allows for a higher energy absorption when subjected to impulse loads (Johansson & Laine, 2012).

Reinforcement bars can be classified into three distinct categories which depend on characteristic limit strain and characteristic ratio tensile strength to yield strength. This classification is illustrated in Table 2.1.

Table 2.1 *Ductility classes for reinforcement steel* (CEN, 2005).

Class	**A**	**B**	**C**
$\left(\frac{f_t}{f_y}\right)_k$	≥ 1.05	≥ 1.08	≥ 1.15 < 1.35
ε_{suk}	≥ 0.025	≥ 0.05	≥ 0.075

According to Al-Emrani et al. (2013) steel reinforcement can be made to be plain, indented or ribbed. The type will influence the bonding forces between the concrete and steel reinforcement. The steel is either made hot rolled, heat treated or cold worked. The two production methods that are of interest for this thesis are hot rolled and cold worked, which will be presented further in this section.

The two different stress-strain relations can be seen in Figure 2.5. The stress-strain relation for the hot rolled steel reinforcement; has four distinct stages that can be distinguished: It is linear elastic until it reaches its plastic plateau, followed by strain hardening and lastly, where it ruptures (Al-Emrani et al., 2013). In contrast, the cold-worked steel stress-strain relation has no distinctive yield stress and there is a lack of a plastic plateau. Further, there is a difference in strain at failure when comparing hot-rolled to cold-worked steel. Illustrated in Figure 2.5 the strain for hot rolled steel is larger which leads to a more ductile response. The strain hardening and plastic deformation capacity is low in comparison to hot-rolled steel. As mentioned by (Johansson & Laine, 2012) reinforcement with a high ductility is preferred in concrete structures subjected to impulse loading and therefore, a hot-rolled steel reinforcement would be preferable.

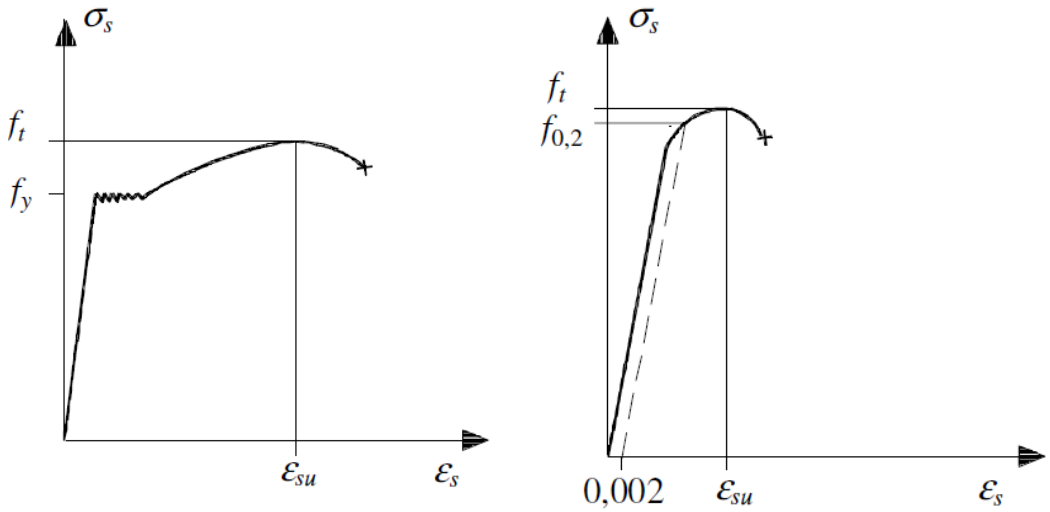

(a) Hot rolled (b) Cold worked

Figure 2.5 *Shows the stress-strain relation for (a) Hot rolled and (b) cold-worked steel* (Al-Emrani et al., 2013).

2.3 Reinforced Concrete

Reinforced concrete is a composite material of concrete and steel that utilizes the benefit of both materials, the compression strength in concrete with the ductility and tensile strength in steel reinforcement. The behaviour of the reinforced concrete can be divided into three stages: state I, state II, and state III, see Figure 2.6.

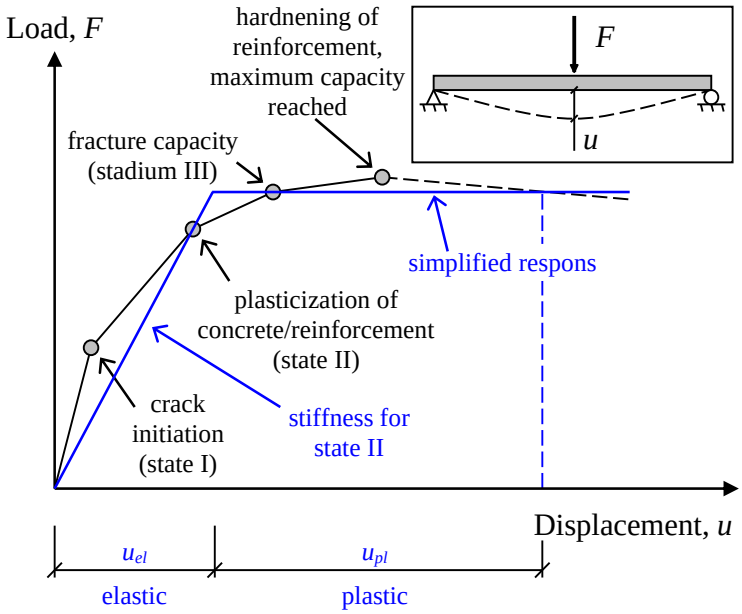

Figure 2.6 The structural response of a reinforced concrete beam and simplified bi-linear response (Johansson & Laine, 2012).

In state I, the reinforced concrete has a linear elastic response. In this state, the steel reinforcement has a small influence on the stiffness and the concrete properties is of most interest. Although, the stiffness of a concrete structure can be increased by more than 20% when including steel reinforcement (Engström, 2015).

In state II, it is assumed that the concrete is cracked while still having a linear elastic response but with lower stiffness (Engström, 2015). The stiffness of a section depends on the reinforcement stiffness and the compressive zone of the concrete. The tensile stress that gets transferred from reinforcement to surrounding concrete will have less steel strain compared to assumed steel strain in a fully cracked section. The cracks will occur at a distance from each other, and the uncracked regions will contribute to the stiffness. This contribution to stiffness is associated with tension stiffening. The tension stiffening will have less of an influence if the applied load is greater than the cracking load. It will also decrease for sustained and repeated loading.

In state III, either the concrete or the steel reinforcement, or both materials have a non-linear response. The structure will have a loss of stiffness and result in a plastic redistribution. The load can increase until the steel reinforcement ruptures or the concrete compressive zone crushes.

The previously explained stages can be explained by a simplified bilinear elasto-plastic response, see Figure 2.6. The section is assumed to be fully cracked initially when the load is applied, and the stiffness is assumed to be in state II until its load capacity is reached (Johansson & Laine, 2012). Afterwards, the concrete section will have an ideally plastic response.

2.4 Strain Rate Effects

Strain rate effect is a phenomenon that explains how mechanical properties of materials such as concrete and steel are affected by high load rate (Johansson, 2000). It is defined as strain rate over time and is denoted by $\dot{\varepsilon}$ and has the unit s^{-1}. An increase in strain rate may lead to an increase in material strength.

The DIF (dynamic increase factor) is a factor that describes how the properties change with varying strain rates. DIF is defined as the ratio between dynamic strength and static strength, seen in Equation (2.9).

$$DIF = \frac{F_{dynamic}}{F_{static}} \tag{2.9}$$

where $F_{dynamic}$ = dynamic stength
F_{static} = static strength

The strain rate changes depending on the type of load that is applied, Johansson & Laine (2012) describe several types of loads, which are presented in Figure 2.7. In this thesis static and dynamic loading is of interest.

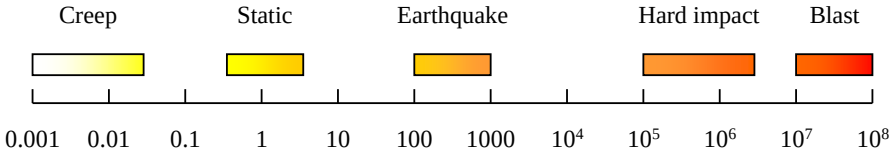

Figure 2.7 *An illustration of strain-rate effects for different activities (Johansson & Laine, 2012).*

2.4.1 Influence on Concrete Strength

The strain rate influences concrete strength which has been studied by numerous researchers. The result of strain rate can be seen Figure 2.8 and Figure 2.9 where the DIF differs from each other and what properties influence the strain rate.

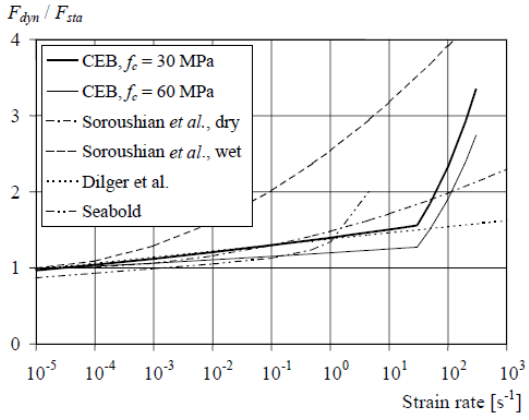

Figure 2.8 *An illustration of the DIF-strain rate relation for concrete in compression* (Johansson, 2000).

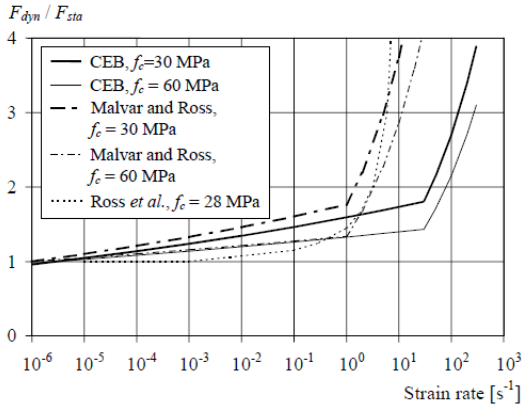

Figure 2.9 *An illustration of the DIF-strain rate relation for concrete in tension* (Johansson, 2000).

As can be seen in Figure 2.8 and Figure 2.9 the pattern of the concrete strength has constant relation until it drastically increases at a specific strain rate, this is referred to as the transition zone. The pattern before and after this zone can be simplified into two strain rate effects, viscous and structural as illustrated in Figure 2.10. The viscous effect is the existence of free water in concrete micropores. When the load is applied slowly on a specimen, cracks can form in the weaker zones and therefore lower energy consumption is demanded.

After the transition zone, there is a larger increase of strength in the concrete with an increasing strain rate. The tensile strength increase can be explained by the inertia effects around crack tips due to changes in stress and energy distribution (Johansson, 2000). The significant increase in concrete strength in compression is a result of inertia confinement effects. This is when concrete is subjected to a fast-loading rate, thus it will not have time to react. This will increase the strength due to multiaxial stress state.

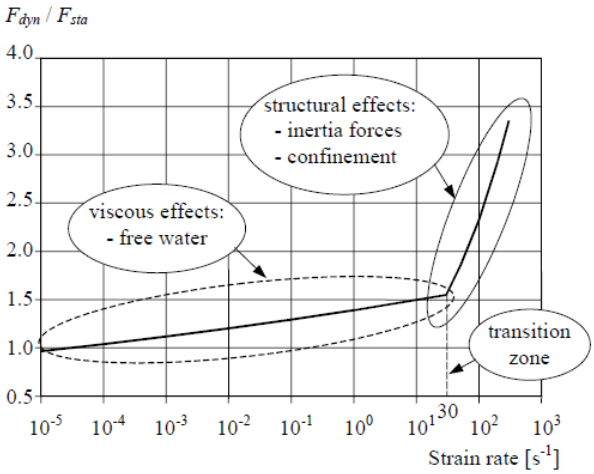

Figure 2.10 *The difference in strain rate effects and showing their stages for concrete* (Johansson, 2000).

2.4.2 Influence on Reinforcement Strength

As mentioned for the concrete, high strain rates influence the steel reinforcement as well. According to Johansson (2000) the strain rate influences a multitude of the properties of steel. Where both the yield and the ultimate stress increase with an increase in strain rate, although young's modulus remain unchanged. The DIF – Strain rate relation can be seen in Figure 2.11.

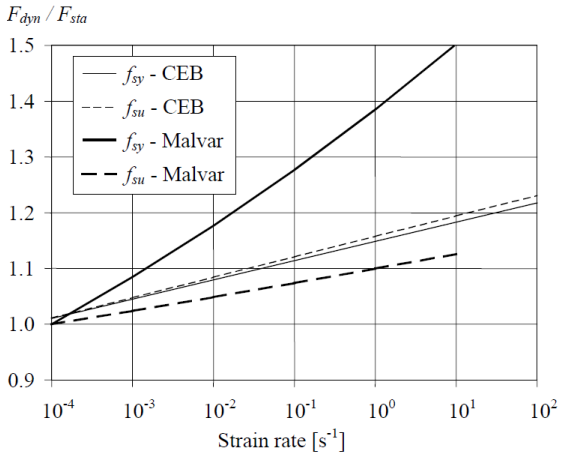

Figure 2.11 *An illustration of the DIF-strain rate relation for reinforcement steel* (Johansson, 2000).

Nonetheless, in Johansson 2000) there was a disparity between the studies when it came to how much the increase from the strain rate effects was. Another disparity that is worth mentioning, is the fact that Malvar suggests that the ultimate strain remains unaffected. On the contrary, CEB suggests the opposite and that the ultimate strain is affected by the strain rate.

3 STRUCTURAL RESPONSE

3.1 Orientation

In this section, the structural response and material properties of concrete, reinforced concrete, and reinforcement steel is treated. The responses can be divided into five distinct subchapters consisting of linear elastic response, plastic response, elasto-plastic response, and brittle and ductile response. The last chapter consists of an introduction to plastic rotation and different methods on how to predict plastic rotation capacity.

3.2 Linear Elastic Response

The characterization of linear elastic response is by having a linear relation in a stress-strain curve (Goodno & Gere, 2021). After unloading, the response of the material returns to its initial state and the stress is equal to zero. This relation can be described by Hooke's law according to Equation (3.1) and the response is illustrated in Figure 3.1.

$$\sigma = E \cdot \varepsilon \tag{3.1}$$

where E = Modulus of Elasticity (Young's Modulus)
σ = Stress
ε = Strain

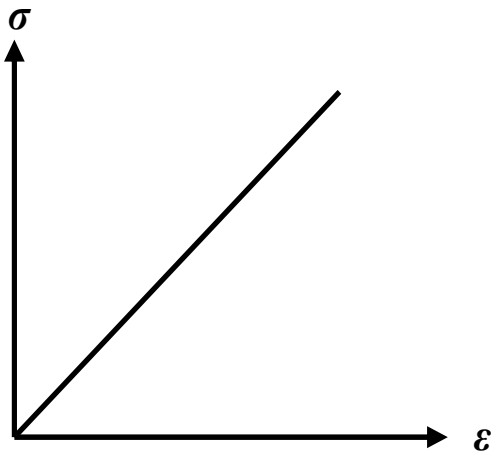

Figure 3.1 Illustration of linear elastic response.

The linear elastic response can also be described by the constant relation between resistance force R and deformation u (Johansson & Laine, 2012). This can be explained by Equation (3.2) and is illustrated in Figure 3.2.

$$R = k \cdot u_{el} \tag{3.2}$$

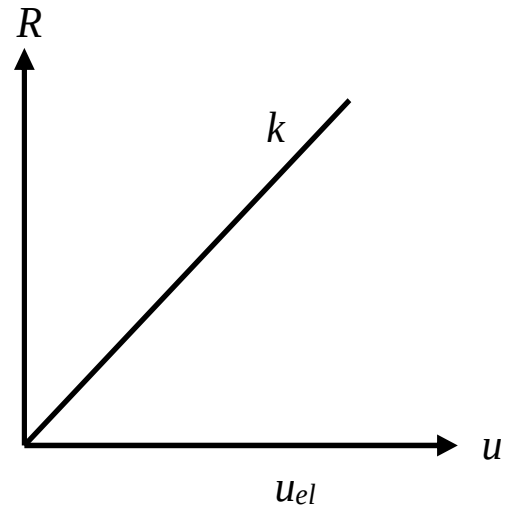

Figure 3.2 Illustration of linear elastic response between internal resistance and deformation.

3.3 Plastic Response

The ideal plastic response is characterized by deformations that cannot be reserved when the structure is unloaded (Johansson & Laine, 2012). The deformation has two conditions which depend on how the external force *F* is in relation to the internal resistance R_m. If the external force *F* is lower than the internal resistance, R_m there will be no lasting deformation. However, if the external force is larger than the internal resistance R_m, the deformations become irreversible. This condition can be described in Figure 3.3 and the Equation (3.3).

$$R(u) = \begin{cases} F \text{ if } u = 0 \\ R_m \text{ if } u > 0 \end{cases} \tag{3.3}$$

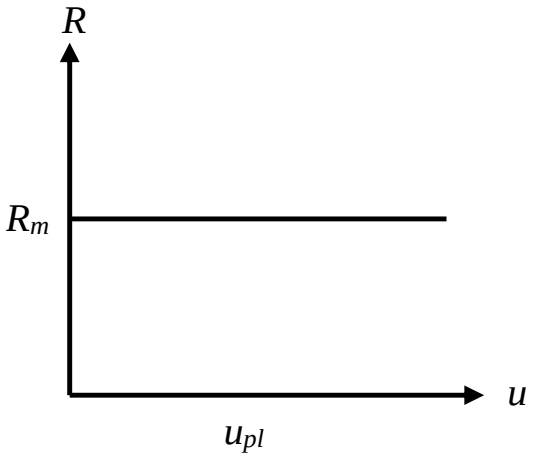

Figure 3.3 Illustration of plastic response between internal resistance and deformation.

3.4 Elasto-Plastic Response

Elasto-plastic response can be described by a combination of elastic and plastic response. As seen in Figure 3.4 a structure will show a linear elastic response in the initial stage. After the maximum internal resistance is reached the structure will plasticize and show a plastic response. After unloading the structure, the linear elastic part will have a reversible response, and the plastic deformation will be irreversible. The relation can be described in Equation (3.4).

$$R(u) = \begin{cases} k \cdot u_{el} \text{ if } u \leq u_{el} \\ R_m \text{ if } u > u_{el} \end{cases} \tag{3.4}$$

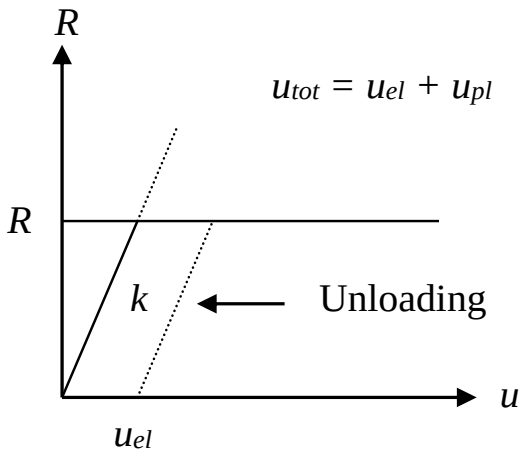

Figure 3.4 Illustration of elasto-plastic between internal resistance R and displacement u.

3.5 Ductile and Brittle Response

To get an understanding of the failure behaviour of a material, the ductile and brittle response of a material can be considered. A brittle failure of a material is characterized by small development of deformations before failure occurs e.g., deformation from shear failure, see Figure 3.5b (Johansson et al., 2021). This is an unfavourable failure mode since the structure loses a big part of its potential energy capacity and therefore its capacity to resist impulse loading. However, a material with a ductile response will result in plastic deformation. This is a favourable failure mode where the structure can have a higher energy absorption through larger deformation e.g., deformation from bending failure, see Figure 3.5a. As illustrated in Figure 3.5 the energy absorption for ductile bending failure $W_{i.M}$ is larger than the energy absorption for brittle shear failure $W_{i.V}$, although the maximum load capacity is the same.

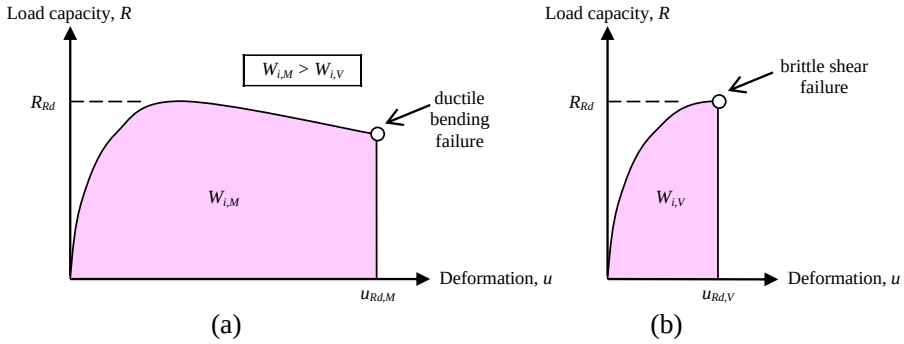

Figure 3.5 Schematic illustration of energy absorption for a loaded structure. Where (a) is for ductile bending failure and (b) for brittle shear failure (Johansson et al., 2021).

3.6 Plastic Rotation

3.6.1 Introduction

To determine the response of a concrete structure subjected to load, plastic rotation can be used to assess if a structure can withstand the load (Johansson & Laine, 2012). The ductile and brittle response can be described with plastic rotation and how large energy absorption a structure has. A ductile behaviour is of interest when a concrete structure is subjected to impulse loading. The ductility is dependent on the reinforcement properties which enables the specimen to form plastic hinges to keep the load-carrying capacity when deformation is increased.

There are different approaches to characterize the plastic rotation depending on if a section or a region is being studied. If a certain section is considered it is assumed that the plastic hinge occurs over this section (Engström, 2015). The plastic rotation is obtained by calculating the rotation of the plastic hinge when the applied load increases from yielding and reaches the collapse mechanism. However, in a structure, the plastic deformation occurs in a plastic region which is a more representative way to describe the plastic rotation.

The plastic rotation can be calculated by integrating the plastic curvature over the length l_{pl}. The plastic rotation will be influenced by the plastic zone l_{pl} and strain distribution in the cross-sections. To define the plastic rotation of a cross-section, the upper limit for the curvature is used which normally is the ultimate concrete strain (Engström, 2015). In the case of low ductility or high steel ratios, the steel strain can be used for ultimate curvature. The curvature for the initiation of plastic deformation can be seen in Equation (3.5).

$$\left(\frac{1}{r}\right)_y = \frac{\varepsilon_{cy}}{x_y} = \frac{\varepsilon_{sy}}{d - x_y} \tag{3.5}$$

where ε_{cy} = concrete strain at the compressive edge when steel starts to yield
ε_{sy} = yield strain of the tensile reinforcement
x_y = depth of the compressive zone when steel starts to yield

When the structure reaches a collapse mechanism the expression of curvature differs depending on which failure takes place. When the concrete strain ε_{cu} is critical it can be expressed as

$$\left(\frac{1}{r}\right)_u = \frac{\varepsilon_{cu}}{x_u} = \frac{\varepsilon_s}{d - x_u} \tag{3.6}$$

where ε_{cu} = ultimate concrete strain at the compressive edge
ε_s= steel rain in the ultimate limit state
x_u= depth of the compressive zone in the ultimate limit state

When the steel strain is critical it can be expressed as

$$\left(\frac{1}{r}\right)_u = \frac{\varepsilon_{cc}}{x_u} = \frac{\varepsilon_{sud}}{d - x_u} \tag{3.7}$$

where ε_{cc} = concrete strain at the compressive edge when the ultimate steel strain is reached
ε_{sud} = ultimate steel strain, design value

Hence, the plastic curvature is obtained by the difference between the ultimate curvature and curvature when yielding starting takes place in steel. This can be expressed as

$$\left(\frac{1}{r}\right)_{pl} = \left(\frac{1}{r}\right)_u - \left(\frac{1}{r}\right)_y \tag{3.8}$$

By incorporating the steel strain in expression, the plastic curvature can be determined as

$$\left(\frac{1}{r}\right)_{pl} = \frac{\varepsilon_s}{d - x_u} - \frac{\varepsilon_{sy}}{d - x_y} \approx \frac{\varepsilon_s - \varepsilon_{sy}}{d - x_u} \tag{3.9}$$

The plastic curvature varies between the sections since the steel strain varies from the yield strain to the maximum steel strain, and for these reasons the plastic rotation will also vary (Engström, 2015).

3.6.2 Moment Distribution Effect on the Plastic Rotation

As explained in Section 3.6 the plastic rotation can be calculated by integrating the plastic curvature over the length l_{pl}. The value of plastic rotation is dependent on distribution of the plastic hinge and the magnitude of the moment over the yielding moment Johansson et al. (2021).

In Figure 3.6 two different cases of simply supported beams is displayed. It is assumed that the beams have the same moment capacity but with different load configuration; a distributed load over the span and a point load in the midspan. In the region where the moment is between the maximal moment M_u and the yielding moment M_y, a plastic hinge with length l_{pl} is assumed to form, Johansson et al. (2021). As can be seen in

Figure 3.6 the moment distribution varies with the load configuration, where a distributed load will result in a parabolic formed moment distribution and point load will result in a triangle formed moment distribution. It can be noted that the length l_{pl} of the plastic hinge will differ for the two cases, where the distance is larger for a distributed load. Therefore, the magnitude of the plastic hinge l_{pl} is also a function of the beam's moment distribution and the moment ratio $\eta_M = M_u/M_y$. The magnitude of the plastic hinge l_{pl} will increase for distributed load compared to a point load, and moment ratio η_M will similarly have the same outcome.

As previously stated, the moment distribution influences the magnitude of the plastic rotation, it is to be noted that the moment distribution, in turn, depends on the loading configuration and the boundary condition of the beam Johansson et al. (2021). Hence, the obtained plastic rotation should be studied within its condition, i.e., not comparing a beam subjected to distributed load to a point load in the midspan.

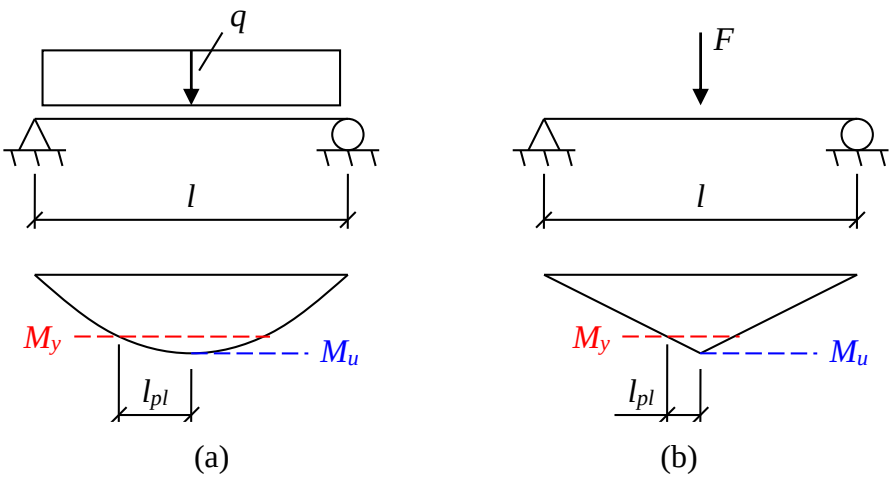

Figure 3.6 *Illustration of plastic hinge l_{pl} for a simply supported beam subjected to (a) distributed load and (b) point in the midspan* (Johansson et al., 2021).

3.7 Methods to Predict Plastic Rotation Capacity

3.7.1 Introduction

There are different ways to determine the plastic rotation capacity of reinforced concrete structures. In this thesis, the methods BK25 (Fortifikationsförvaltningen, 1973), ABC (Betonghandboken, 1990), Eurocode 2 (CEN, 2005) and MSB (Johansson et al., 2021) are used to estimate the plastic rotation. BK25 is derived from an assumption that the beam is subjected to an air blast or impulse load. The ABC method is based on the strength of the reinforcement and its properties, it also considers the position of the plastic hinge. Eurocode 2 is a simplified method based on a point load in the midspan of a simply supported beam, where the result is derived from a graph. Lastly, MSB is derived from Eurocode 2.

3.7.2 BK25

The method in BK25 (Fortifikationsförvaltningen, 1973) is used to predict the plastic rotation capacity in concrete beams and slabs that are subjected to an impulse load or air blast considered as a distributed load. (Johansson & Laine, 2012). The plastic hinge is presumed to be in a region with the length $2l_{Pl}$ and within this region, the curvature is assumed to be constant as seen in Figure 3.7. With this, the plastic rotation can be calculated as

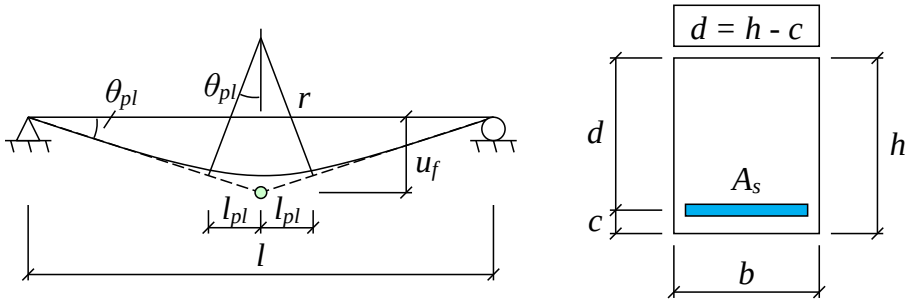

Figure 3.7 Illustrating the different variables in the BK25-method (Johansson & Laine, 2012).

$$l_p = 0.5 \cdot d + 0.15 \cdot l \tag{3.10}$$

$$\theta_{pl} = \frac{l_p}{r} \tag{3.11}$$

where l_p = the length of the plastic hinge, calculated according to Equation (3.10)
d = the effective depth of the cross-section
$\frac{1}{r}$ = the curvature

The maximum allowed curvature is based on allowed steel strain and ultimate strain in the concrete, thus the curvature can be calculated as

$$\frac{1}{r} = \frac{\varepsilon_{cu}}{x} = \frac{\varepsilon_s}{d - x} \tag{3.12}$$

where ε_{cu} = the ultimate strain in the concrete.
ε_s = the mean strain in the steel over the length a
d = the effective depth of the cross-section
x = the effective height of the compression zone

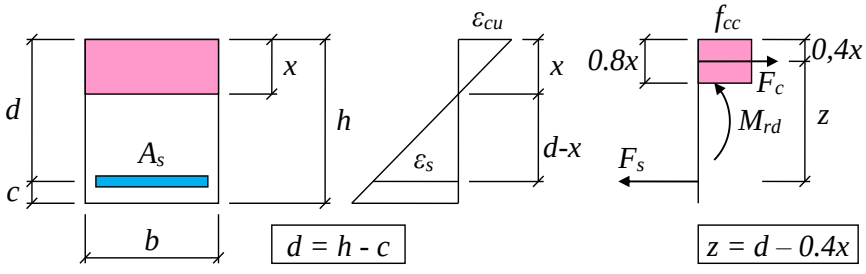

Figure 3.8 Shows the concrete specimen (Johansson & Laine, 2012).

In Figure 3.8, the effective depth d of the cross-section and the effective height of the compression zone x can be seen. In Figure 3.8 a horizontal force equilibrium, $Fc = Fs$ gives

$$f_{cc} \cdot b \cdot 0.8x = f_{st} \cdot A_s \tag{3.13}$$

With the definition of reinforcement ratio

$$\rho = \frac{A_s}{b \cdot d} \tag{3.14}$$

and the reinforcement subjected to tension

$$\omega_s = \frac{A_s}{b \cdot d} \cdot \frac{f_{st}}{f_{cc}} \tag{3.15}$$

This means that the height of the compression zone can be calculated as

$$x = \frac{1}{0.8} \cdot \rho \cdot d \cdot \frac{f_y}{f_{cc}} = \frac{\omega_s \cdot d}{0.8} \tag{3.16}$$

or the ratio $\frac{x}{d}$ as

$$\frac{x}{d} = \frac{\omega_s}{0.8} \tag{3.17}$$

With this, the limit for when different failure modes occur can be calculated as

$$\omega_{s,crit} = \frac{0.8 \cdot \varepsilon_{cu}}{\varepsilon_{cu} + \varepsilon_s} \tag{3.18}$$

If $\omega_s > \omega_{s,crit}$, then the failure mode is crushing of the concrete, thus the rotation capacity is calculated as

$$\begin{aligned} \theta_{pl.f} = \frac{l_p}{r} = \frac{0.5 \cdot d + 0.15 \cdot l}{r} = \frac{0.8 \cdot \varepsilon_{cu}}{\omega_s \cdot d} \cdot (0.5 \cdot d + 0.15 \cdot l) = \\ = \frac{0.4 \cdot \varepsilon_{cu}}{\omega_s} \cdot \left(1 + 0.3 \cdot \frac{l}{d}\right) \end{aligned} \tag{3.19}$$

However, if $\omega_s < \omega_{s,crit}$ then the failure mode is the rupture of the steel reinforcement, and the rotation capacity is instead calculated as

$$\begin{aligned} \theta_{pl.f} = \frac{l_p}{r} = \frac{0.5 \cdot d + 0.15 \cdot l}{r} = \frac{0.8 \cdot \varepsilon_s}{d \cdot (0.8 - \omega_s)} \cdot (0.5 \cdot d + 0.15 \cdot l) \\ = \frac{0.4 \cdot \varepsilon_s}{0.8 - \omega_s} \cdot \left(1 + 0.3 \cdot \frac{l}{d}\right) \end{aligned} \tag{3.20}$$

The Equations (3.19) and (3.20) are only valid for the case where a plastic hinge is developed in the middle of the span. In the case of the plastic hinge occurring over the support, Equation (3.10) is instead written as

$$l_p = 0.5 \cdot d + 0.1 \cdot l_1 \tag{3.21}$$

Where l_1 is the shear span of the beam and can be calculated as

$$l_1 = \frac{M_{sup}}{V_{sup}} \tag{3.22}$$

where M_{sup} = The moment at the support
V_{sup} = The shear force at the support

For a beam subjected to a uniformly distributed load q, with the length l and has a moment capacity over the supports and the span denoted as M_{sup} and M_f, respectively. The following Equations can be derived

$$M_{sup} + M_f = \frac{q \cdot l^2}{2} \tag{3.23}$$

$$V_{sup} = \frac{q \cdot l}{2} \tag{3.24}$$

where M_{sup} can be calculated by

$$M_{sup} = \alpha \cdot M_f \tag{3.25}$$

α is a variable that is dependent on the amount of reinforcement in the span and the field denoted as ρ_{span} and ρ_f, respectively. Thus, α can be expressed as

$$\alpha = \frac{\rho_{span}}{\rho_f} \tag{3.26}$$

The Equations from (3.22) to (3.26) are combined and thus, the length l_1 can be recalculated as

$$l_1 = \frac{\rho_{span}}{\rho_{span} + \rho_f} \cdot \frac{l}{4} \tag{3.27}$$

The rotation capacity over the support is denoted as θ_{sup} can be derived as

$$\theta_{sup} = \frac{l_p}{r} = \frac{0.1 \cdot \left(\frac{\rho_{span}}{\rho_{span} + \rho_f}\right) \cdot \frac{1}{4} \cdot 0.5 \cdot d}{r} = \frac{d}{2 \cdot r} \cdot \left(1 + \frac{1}{20} \cdot \frac{\rho_{span}}{\rho_{span} + \rho_f} \cdot \frac{l}{d}\right) \tag{3.28}$$

Using the same criteria as in Equations (3.19) and (3.20), the failure mode for crushing of the concrete, the plastic rotation capacity can be calculated as

$$\theta_{sup} = \frac{0.4 \cdot \varepsilon_{cu}}{\omega_s} \cdot \left(1 + \frac{1}{20} \cdot \frac{\rho_{span}}{\rho_{span} + \rho_f} \cdot \frac{l}{d}\right) \tag{3.29}$$

And when the rupture of steel reinforcement is governing

$$\theta_{sup} = \frac{0.4 \cdot \varepsilon_s}{0.8 - \omega_s} \cdot \left(1 + \frac{1}{20} \cdot \frac{\rho_{span}}{\rho_{span} + \rho_f} \cdot \frac{l}{d}\right) \tag{3.30}$$

3.7.3 BK25 for Point Load in Midspan

As previously mentioned, the BK25 method is used for a simply supported or fixed beam subjected to a distributed load. This section is considering a simply supported beam subjected to a point load in the midspan which is the case for this thesis. This is achieved by studying the end support of the calculation model and applying the correct distance l_1 for a plastic hinge. This is illustrated in Figure 3.9 and calculated according to the Equations (3.31) to (3.35).

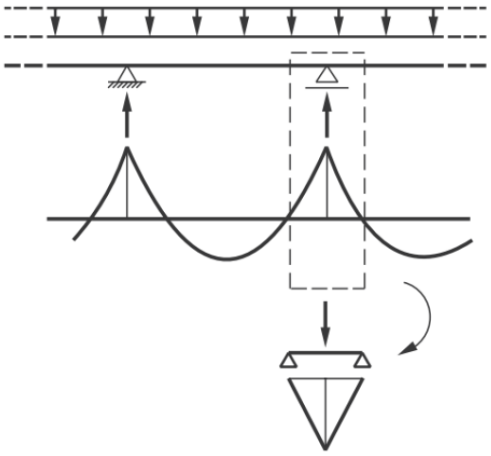

Figure 3.9 *Illustration of how a distributed load is converted into a point load in the midspan* (Johansson et al., 2021).

For a simply supported beam subjected to a point load in the mid span with length l_1 can be defined as

$$l_1 = \frac{l}{2} \tag{3.31}$$

The length of the plastic hinge l_p at the support can be express as

$$l_p = 0.5 \cdot d + 0.1 \cdot l_1 = 0.5 \cdot d + 0.1 \cdot \frac{l}{2} = 0.5d + 0.05l \tag{3.32}$$

The rotation capacity over the support is denoted as $\theta_{s.p}$ can be derived as

$$\theta_{s.p} = \frac{l_p}{r} = \frac{0.5d + 0.05l}{r} = \frac{d}{2 \cdot r} \cdot \left(1 + 0.1 \cdot \frac{l}{d}\right) \tag{3.33}$$

Using the same criteria as in Equations (3.19) and (3.20), the failure mode for crushing of the concrete, the plastic rotation capacity can be calculated as

$$\theta_{s.p} = \frac{0.4 \cdot \varepsilon_{cu}}{\omega_s} \cdot \left(1 + 0.1 \cdot \frac{l}{d}\right) \tag{3.34}$$

And when the rupture of steel reinforcement is governing

$$\theta_{s.p} = \frac{0.4 \cdot \varepsilon_s}{0.8 - \omega_s} \cdot \left(1 + 0.1 \cdot \frac{l}{d}\right) \tag{3.35}$$

3.7.4 Betonghandboken

Prior to the introduction of Eurocode in Sweden, the method used to estimate the plastic rotational capacity was described in Betonghandboken (1990). This method (also referred to as the ABC-Method) is an empirical method where the expression used to calculate the plastic rotation has three factors: A, B and C.

$$\theta = A \cdot B \cdot C \cdot 10^{-3} \tag{3.36}$$

Where the A-factor takes the stirrups, the reinforcement for both compression and tension into consideration. Furthermore, the B-factor considers the steel reinforcements mechanical properties, and the C-factor takes the position of the plastic hinge in relation to the moment curve. Factor A is calculated as

$$A = 1 + 0{,}6 \cdot \omega_v + 1{,}7 \cdot \omega_s' - 1.4 \cdot \frac{\omega_s}{\omega_{bal}} \tag{3.37}$$

$$\omega_v = \frac{A_v}{b \cdot s} \cdot \frac{f_{sv}}{f_{ct}} \tag{3.38}$$

$$\omega_s' = \frac{A_s'}{b \cdot d} \cdot \frac{f_{sc}}{f_{cc}} \tag{3.39}$$

$$\omega_s = \frac{A_s}{b \cdot d} \cdot \frac{f_{st}}{f_{cc}} \tag{3.40}$$

where ω_v is the mechanical reinforcement ratio for stirrups and its calculated according to Equation (3.38).
ω_s' is the reinforcement subjected to compression and is calculated according to Equation (3.39).
ω_s is the reinforcement subjected to tension and is calculated according to Equation (3.40).

A_v = area of shear reinforcement
A'_s = area of reinforcement in compression
A_s = area of reinforcement in tension
f_{sv} = strength of shear reinforcement
f_{sc} = strength of reinforcement in compression
f_{st} = strength of reinforcement in tension
f_{ct} = tensile strength of the concrete
f_{cc} = compression strength of the concrete
b = width of the compression zone of the cross-section
d = effective width of the cross-section
s = distance between the stirrups

The factor ω_{bal} is a factor that takes the balanced mechanical reinforcement ratio into consideration and is calculated as

$$\omega_{bal} = \frac{0.8 \cdot \varepsilon_{cu}}{\varepsilon_{cu} + \varepsilon_{sy}} \tag{3.41}$$

where ε_{cu} = the ultimate strain in the concrete at the edge on the compression side
ε_{sy} = yield limit strain and it is calculated as

$$\varepsilon_{sy} = \frac{f_{st}}{E_s} \tag{3.42}$$

where E_s= young's modulus of the reinforcement steel
f_{st} = the strength of reinforcement in tension

Factor B as previously mentioned considers the mechanical properties of the reinforcement and can be seen in Table 3.1.

Table 3.1 Values for B. Based on (Betonghandboken, 1990).

Reinforcement Type	**B**	**Max A·B**
Ks 60, Ks 40, Ss 26, Ss 26s	1.0	1.7
Ks 60S, Ks 40S[1)]	0.8	1.1
Coldworked steel with $\varepsilon_{su} \geq 3\%$ *and* $\frac{f_{su}}{f_{sy(0.2)}} \geq 1.1$	$0.6 \cdot \left(1 - 0.7 \cdot \frac{\varepsilon_p}{\varepsilon_{su}}\right)$	0.5

[1]) *if* $\frac{f_{su}}{f_{sy(0.2)}} \geq 1.4$ *and* $\varepsilon_{su} \geq 8\%$ *then values for Ks 60 and Ks 40 is used.*

The last factor C considers the position of the plastic hinge. Thus, two different Equations are used depending on if it is over the support or the span, these can be seen in Equations (3.43) and (3.44), respectively.

$$C_{support} = 10 \cdot \frac{l_{0,support}}{d} \tag{3.43}$$

$$C_{span} = 7 \cdot \frac{l_{0,span}}{d} \tag{3.44}$$

where $l_{0,support}$ is the distance from the plastic hinge to the chosen zero-point moment at the support, see Figure 3.10
$l_{0,span}$ is the distance from the plastic hinge to the chosen zero-point moment in the span, see Figure 3.10

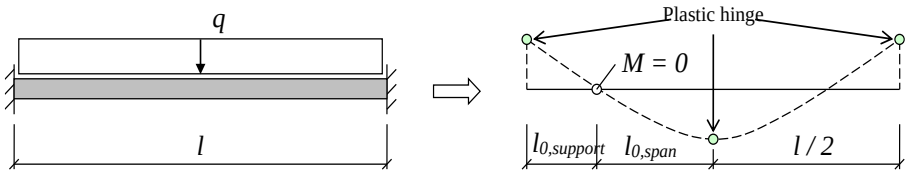

Figure 3.10 An illustration of $l_{0,support}$ and $l_{0,span}$ for the ABC-method (Johansson & Laine, 2012).

3.7.5 Eurocode 2

The method procedure proposed in Eurocode 2 (CEN, 2005) is used to estimate the plastic rotation capacity for a simply supported beam subjected to a point load in the midspan (Johansson et al., 2021). The designed plastic rotation $\theta_{pl,d}$, is given by the ratio x_u/d where x_u is the height of the compressive zone in the ultimate limit state and d is the effective height of the cross-section. The steel and concrete class is also taken into consideration, see Figure 3.11.

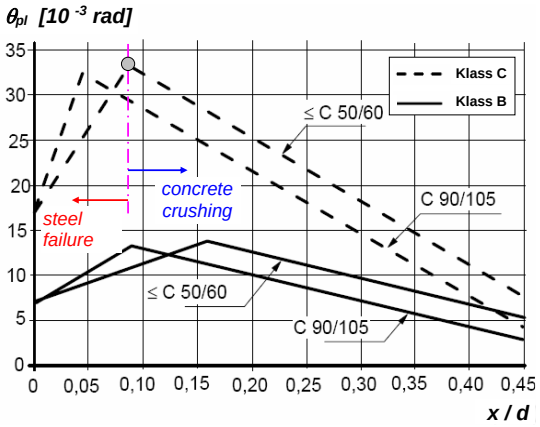

Figure 3.11 An illustration of the different failure modes in comparison to the steel and concrete class (Johansson & Laine, 2012).

The presented method is a simplified and conservative way to calculate the plastic rotation since it considers modelling uncertainties (Engström, 2015). The value obtained from the diagram presented in Figure 3.11 is valid if the shear slenderness ratio, $\lambda = 3$. If not, then the plastic rotation is multiplied by Equation (3.45).

$$k_\lambda = \sqrt{\frac{\lambda}{3}} \tag{3.45}$$

where $\lambda = \frac{x_0}{d}$ (shear slenderness)

x_0 = distance between the considered maximum moment section and the adjacent zero moment section after plastic redistribution, i.e., the final moment distribution

d = effective depth

$$\lambda = \frac{M_{ed}}{V_{ed} \cdot d} \tag{3.46}$$

where M_{ed} = design value of bending moment

V_{ed} = design value of shear force

The plastic rotation in Figure 3.11 is defined as the rotation of a double-sided hinge, which is illustrated in Figure 3.12. Thus, the plastic rotation capacity is calculated as:

$$\theta_{RD,EC2} = \frac{k_\lambda}{2} \cdot \theta_{pl} \tag{3.47}$$

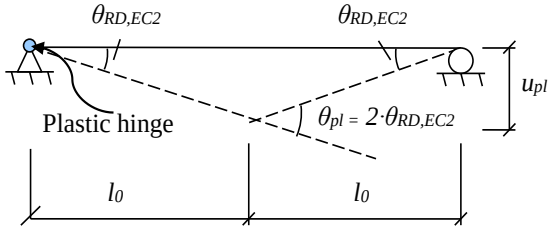

Figure 3.12 Schematic illustration of the plastic rotation for a simply supported beam, inspired by (Johansson et al., 2021).

3.7.6 Background to Eurocode 2 (EC2-detailed)

Plastic rotation using Eurocode 2 method is calculated by considering a continuous beam under a distributed load, see Figure 3.13a Johansson et al. (2021). The plastic rotation for the internal support of the continuous beam is approximately the same as the plastic rotation for a simply supported beam subjected to a point load in the midspan. By using this assumption, the moment-curvature relation can be calculated for different stages of reinforced concrete: stage I ($M \leq M_{cr}$), stage II ($M_{cr} \leq M \leq M_y$) and stage III ($M_y \leq M \leq M_u$). Hence, the plastic rotation can be determined by the difference of total plastic rotation at maximum moment M_u and yielding moment M_y.

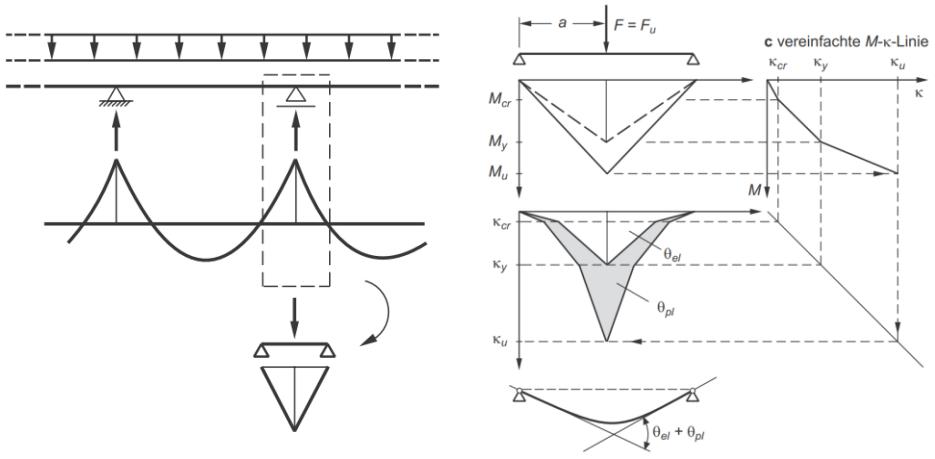

(a) (b)

Figure 3.13 Schematic illustration of the plastic rotation capacity in Eurocode 2: (a) Background to load case, (b) moment-curvature relation $M(\kappa)$ and plastic rotation capacity. From Zilch and Zehetmaier (2010).

The plastic rotation is determined by using the relation seen in Figure 3.13b. The background (EC2-detailed) for these relations is not stated in Eurocode 2 but according to Zilch and Zehetmaier (2010) the following Equations (3.48) to (3.53) served as foundation to calculate the plastic rotation capacity.

$$\theta_{pl} = \beta_n \cdot \beta_s \cdot \frac{\varepsilon_{su}^* - \varepsilon_{sy}}{1 - \frac{x_d}{d}} \cdot \sqrt{\frac{\lambda}{3}} \tag{3.48}$$

where

$$\varepsilon_{su}^* = \min \begin{cases} 0.28 \cdot (\beta_s \cdot \xi_d)^{0.2} \cdot \varepsilon_{su} \\ 1.75 * \xi_d^{\frac{2}{3}} \cdot \left(\frac{1}{\xi_d} - 1\right) \cdot \varepsilon_{su} \end{cases} \tag{3.49}$$

$$\xi_d = \frac{x}{d} \tag{3.50}$$

$$\beta_n = 22.5 \tag{3.51}$$

$$\beta_s = \left(1 - \frac{f_{yk}}{f_{uk}}\right) \tag{3.52}$$

$$\beta_c = \left(\frac{0.0035}{\varepsilon_{cu}}\right) \tag{3.53}$$

The effect of ductile properties f_u/f_y and ultimate steel strain ε_{su} on the plastic rotation has been studied by Johansson et al (2021). The result shown in Figure 3.14 illustrated the plastic rotation for reinforced concrete beams with steel classes of: A, B, C, Ks 40 (1) and KS40 (2).

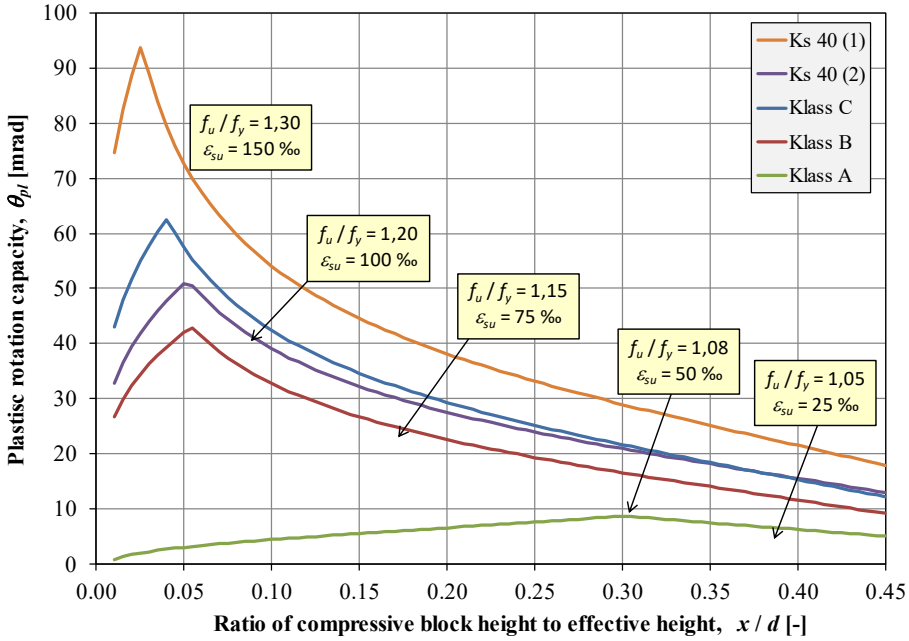

Figure 3.14 *Plastic rotation capacity in relation to x/d ratio with steel classes A, B, C, KS 40 (1) and KS 40 (2).*

By using Equation (3.48) to (3.53), the plastic rotation θ_{pl} in relation to the ratio of compressive block height to effective height x/d can be illustrated in Figure 3.15a. It can be observed that the plastic rotation increases for higher value on the ultimate steel strain where f_u/f_y is constant. The increase of plastic rotation can also be seen in Figure 3.15b for higher value of f_u/f_y where the ultimate steel strain is constant.

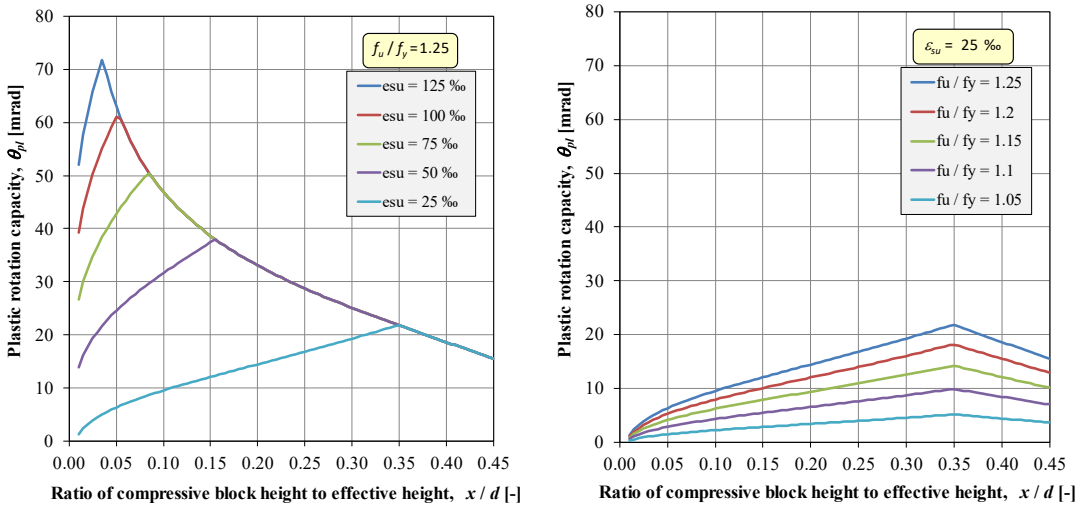

(a) (b)

Figure 3.15 *(a) Plastic rotation capacity in relation to x/d ratio where f_u/f_y is constant. (b) Plastic rotation capacity in relation to x/d ratio where ε_{su} is constant.*

Figure 3.16 is illustrating the plastic rotation capacity based on the EC2-detailed-method where the reinforcements properties from the experiment are being considered.

The dashed lines in the Figure 3.16 are illustrating the plastic rotation relation for class B and C reinforcement. The black dots in the graph are illustrating the x/d ration for respective beam and the type of failure modes the beams are experiencing. The beam with reinforcement of 6 mm reaches failure due to rupture of reinforcement, in contrast to beams with reinforcement of 8 mm and 10 mm reaches failure due to crushing of concrete.

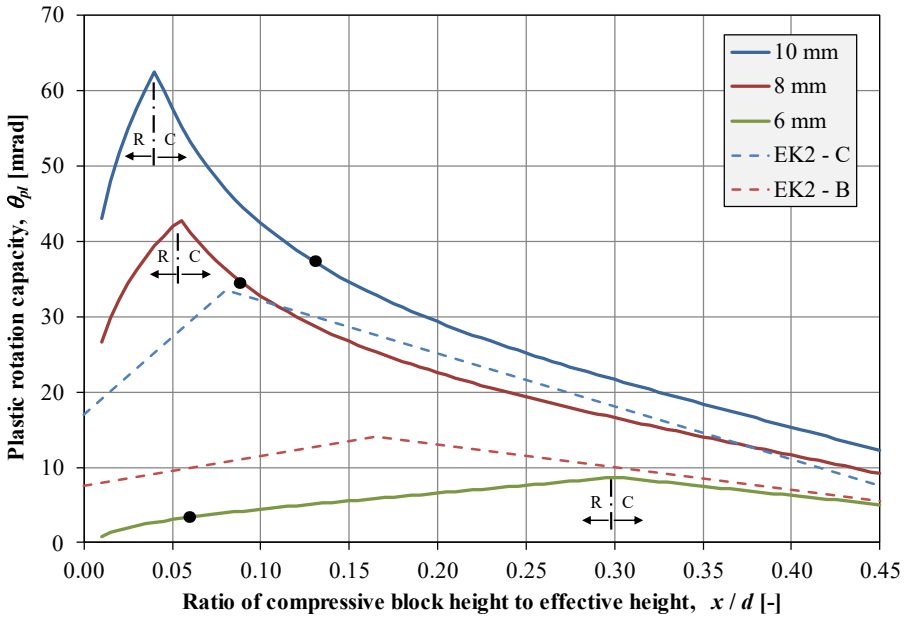

Figure 3.16 *Plastic rotation capacity for beams tested in 3-point bending test when considering reinforcement properties from experiment. R=Rupture of reinforcement and C=Crushing of concrete.*

3.7.7 MSB

According to Johansson et al. (2021) the plastic rotation capacity can be calculated as in Equation (3.54).

$$\theta_{Rd,MSB} = 2 \cdot \theta_{Rd,EC2} = \kappa_{\lambda} \cdot \theta_{pl} \tag{3.54}$$

where $\theta_{Rd,EC2}$ is the plastic rotation from Eurocode 2

Consequently, by using the MSB method will result in twice as large plastic rotation capacity compared to the method presented in Eurocode 2.

3.8 Previous Chalmers Experiments

In this section a summary of plastic rotation capacity of reinforced concrete beams is presented for previous theses performed between 2017 and 2023 at Chalmers University of Technology (Lozano & Makdesi, 2017; Jönsson & Stenseke, 2018; Andersson & Pettersson, 2019; Nigani & Nordström, 2020; Erikson & Gustafsson, 2021; Nozad & Steiner, 2021), see Table 3.2. The beams for these studies have a varied geometry and load configuration which is presented more in detail in Table 3.2. The beams are either tested in a 3-point bending test or in a 4-point bending test. The plastic

rotations capacity obtained from experiment are presented for different levels: 100 %, 95 %, 90 %, and 80 %. The predicted plastic rotation capacities are calculated by using methods explained in Section 3.6.

The Figure 3.17 shows the tested plastic rotation capacity on the beams presented in x-axis in relation to calculated plastic rotation capacity in y-axis. The figures are presented for levels between 100 % and 80 % for EC2-method, however, only level 100 % for BK25-method and ABC-method. The diagonal line in the graphs is used to differentiate whether the results are closer to predicted plastic rotation capacity or the tested plastic rotation capacity. It can be noted that the result that are in the region below the diagonal gives a more conservative result. The results are distinguished in two different load configurations, a 3-point bending test and a 4-point bending test depicted as a triangle and a circle, respectively.

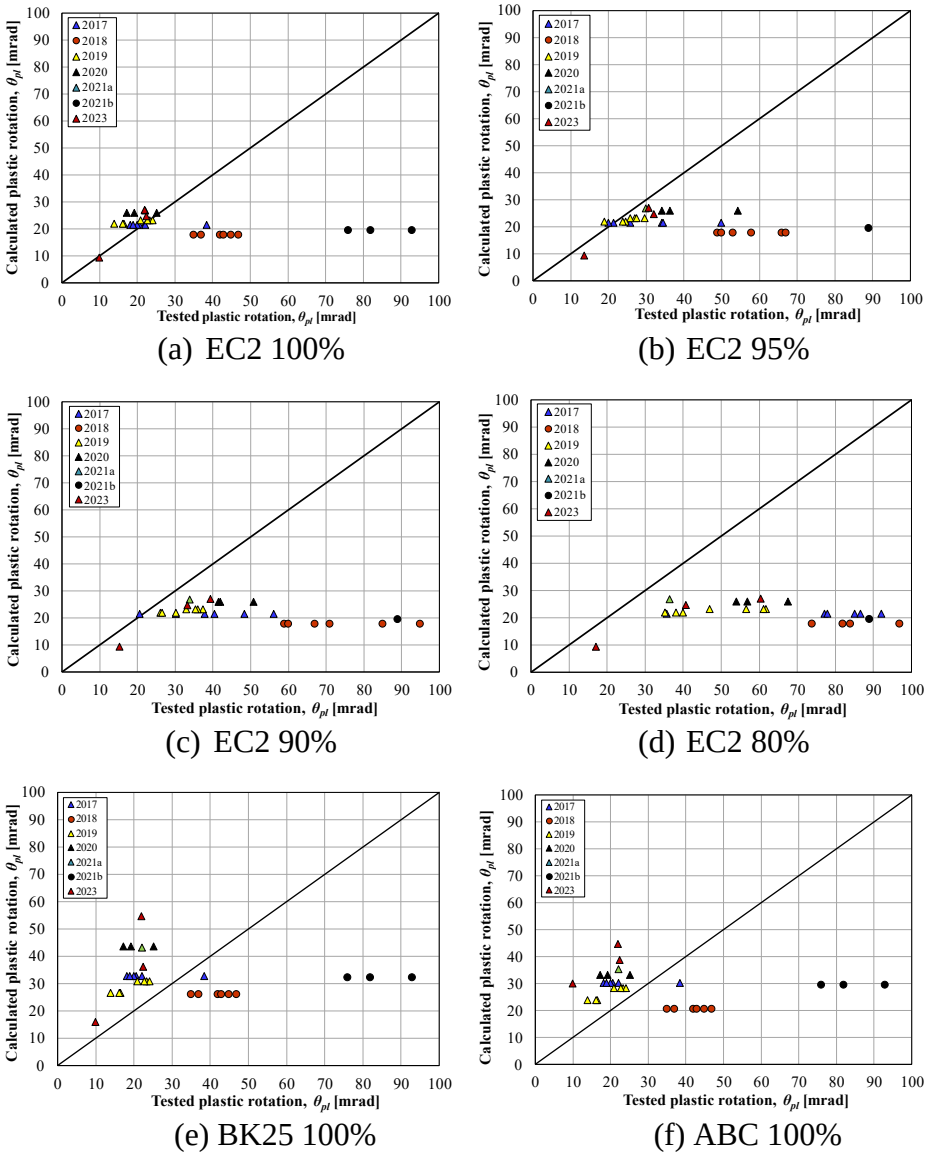

Figure 3.17 Comparison between the calculated plastic rotation capacity and the tested plastic rotation capacity.

Figure 3.17 illustrates the correlation between the estimate plastic rotation capacity, using various methods, and the tested ones. Most of the results are above the diagonal line for level 100 %, thus, it indicates that the estimated plastic rotation is non-conservative. There are some dissimilarities between levels 100 % and 80 % for EC2-method. The result for the tested plastic rotation shifts to the right for respective lower levels. For the case of 80 % the plastic rotation capacity is on the most conservative side. Another observation is that the dispersion between the results increases for respective lower level.

Comparatively, BK25-method and ABC-method indicated a non-conservative way of predicting plastic rotation capacity which seen for the beams that are above the diagonal line. One explanation for the differences might be how the methods are derived. Illustrated in Figure 3.18 the plastic rotation capacity on EC2-method is based on the maximal load capacity and ABC-method are based of 95% of the maximal load capacity. This will yield different distances on the plastic deflection; thus, it will result in different plastic rotation capacities.

It can be observed in that the beams from 2018 and 2021b have a considerably higher plastic rotation capacity from the experiment compared to the predicted plastic rotation capacity. This can be explained by the load configuration, where those beams are subjected to a 4-point bending test. The moment distribution for beams tested in 4-point bending test will yield in a larger plastic hinge compared to beams tested in 3-point bending test, hence, a larger rotation capacity. It is to be noted that the beams from 2021b also used larger reinforcement diameters in comparison to the other beams.

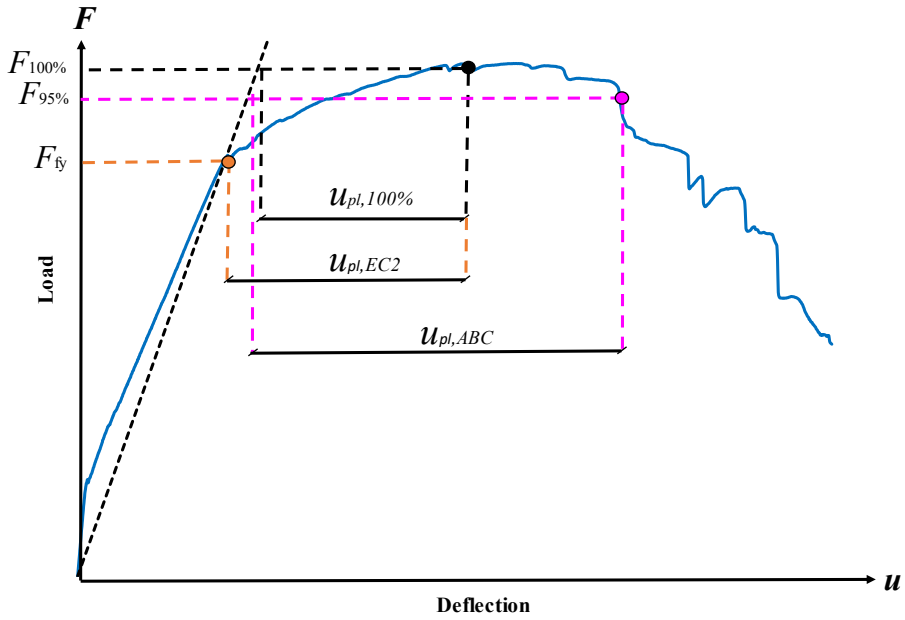

Figure 3.18 Schematic illustration how the different methods are derived regarding the plastic rotation capacity.

In Figure 3.19 the plastic rotation capacity for the beams tested statically only in Chalmers between 2017-2023 are presented. It can be observed that beams tested in 4-point bending test resulted in higher plastic rotation capacity.

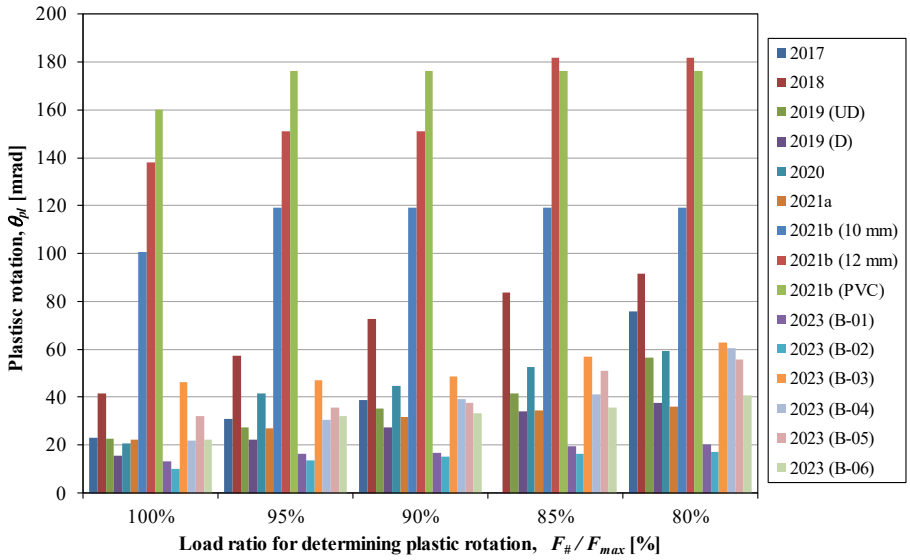

Figure 3.19 Tested plastic rotation capacity for beams tested between 2017 and 2023.

Table 3.2 Summary of measured and calculated plastic rotation capacity for theses between 2017 and 2023.

																Measured plastic rotation						Calculated plastic rotation		
Year	Name	l [mm]	b [mm]	h [mm]	d [mm]	L/a [-]	As [mm²]	εsu [%]	fcm [MPa]	fy [MPa]	ft [MPa]	g [-]	ρ=As/(b*d) [-]	ws [-]	Θ100% [mrad]	Θ95% [mrad]	Θ90% [mrad]	Θ85% [mrad]	Θ80% [mrad]	Θ75% [mrad]	ABC [mrad]	BK25 [mrad]	EC2 [mrad]
2017	B07	1000	100	100	80	2	57	10.8	42.2	575	686	1.19	0.71	0.096	20.5	34.1	40.4	-	77.1	-	30.2	32.7	21.6
2017	B08	1000	100	100	80	2	57	10.8	42.2	575	686	1.19	0.71	0.096	20.0	25.7	37.8	-	77.9	-	30.2	32.7	21.6
2017	B09	1000	100	100	80	2	57	10.8	42.2	575	686	1.19	0.71	0.096	22.1	34.4	48.3	-	92.1	-	30.2	32.7	21.6
2017	B16	1000	100	100	80	2	57	10.8	42.2	575	686	1.19	0.71	0.096	18.2	21.3	30.1	-	35.7	-	30.2	32.7	21.6
2017	B17	1000	100	100	80	2	57	10.8	42.2	575	686	1.19	0.71	0.096	18.9	19.9	20.6	-	85.1	-	30.2	32.7	21.6
2017	B18	1000	100	100	80	2	57	10.8	42.2	575	686	1.19	0.71	0.096	38.4	49.8	56.1	-	86.6	-	30.2	32.7	21.6
2018	Beam nr 7	1000	100	100	80	3	57	10.6	36.8	513	623	1.21	0.71	0.099	47.0	58.0	71.0	76.0	82.0	-	20.4	26.0	17.6
2018	Beam nr 8	1000	100	100	80	3	57	10.6	36.8	513	623	1.21	0.71	0.099	37.0	49.0	67.0	91.0	103.0	-	20.4	26.0	17.6
2018	Beam nr 9	1000	100	100	80	3	57	10.6	36.8	513	623	1.21	0.71	0.099	42.0	66.0	85.0	92.0	97.0	-	20.4	26.0	17.6
2018	Beam nr 16	1000	100	100	80	3	57	10.6	36.8	513	623	1.21	0.71	0.099	35.0	50.0	59.0	73.0	84.0	-	20.4	26.0	17.6
2018	Beam nr 17	1000	100	100	80	3	57	10.6	36.8	513	623	1.21	0.71	0.099	43.0	53.0	60.0	62.0	74.0	-	20.4	26.0	17.6
2018	Beam nr 18	1000	100	100	80	3	57	10.6	36.8	513	623	1.21	0.71	0.099	45.0	67.0	95.0	109.0	110.0	-	20.4	26.0	17.6
2019	S-UD-B1-01	1300	100	100	80	2	57	9.4	33	555	656	1.18	0.71	0.119	20.9	27.0	37.3	41.7	61.7	-	28.3	30.9	23.3
2019	S-UD-B1-02	1300	100	100	80	2	57	9.4	33	555	656	1.18	0.71	0.119	23.3	25.7	36.0	45.5	61.2	-	28.3	30.9	23.3
2019	S-UD-B2-03	1300	100	100	80	2	57	9.4	33	555	656	1.18	0.71	0.119	24.0	29.5	32.9	37.3	46.9	-	28.3	30.9	23.3
2019	S-D-B1-04	1300	100	100	80	2	57	5.8	33	645	664	1.03	0.71	0.138	13.9	18.9	26.1	31.6	35.2	-	23.9	26.6	22.0
2019	S-D-B2-05	1300	100	100	80	2	57	5.8	33	645	664	1.03	0.71	0.138	16.5	24.6	30.1	36.4	38.1	-	23.9	26.6	22.0
2019	S-D-B2-06	1300	100	100	80	2	57	5.8	33	645	664	1.03	0.71	0.138	16.2	23.8	26.5	34.1	39.9	-	23.9	26.6	22.0
2020	01-B1-FRP0-S	1300	100	100	80	2	57	8.7	45.5	543	660	1.22	0.71	0.084	19.2	54.3	41.5	45.7	54.0	-	33.1	43.6	25.9
2020	02-B1-FRP0-S	1300	100	100	80	2	57	8.7	45.5	543	660	1.22	0.71	0.084	25.2	36.2	41.9	50.6	56.8	-	33.1	43.6	25.9
2020	02-B1-FRP0-S	1300	100	100	80	2	57	8.7	45.5	543	660	1.22	0.71	0.084	17.2	34.2	50.8	61.7	67.5	-	33.1	43.6	25.9
2021a	01-S-0FRP	1300	100	100	80	2	57	8.3	55.6	543	661	1.22	0.71	0.069	-	24.5	30.0	33.3	35.4	36.2	35.3	43.1	26.8
2021a	02-S-0FRP	1300	100	100	80	2	57	8.3	55.6	543	661	1.22	0.71	0.069	22.1	29.8	33.8	35.9	36.5	37.4	35.3	43.1	26.8
2021b	Beam 1	2400	200	200	160	3	157	6.4	54	564	656	1.16	0.49	0.051	82.0	109.0	109.0	-	109.0	-	29.3	32.1	19.4
2021b	Beam 2	2400	200	200	160	3	157	6.4	54	564	656	1.16	0.49	0.051	93.0	107.0	107.0	-	107.0	-	29.3	32.1	19.4
2021b	Beam 3	2400	200	200	160	3	157	6.4	54	564	656	1.16	0.49	0.051	76.0	89.0	89.0	-	89.0	-	29.3	32.1	19.4
2021b	Beam 10	2400	200	200	160	3	157	6.4	54	564	656	1.16	0.49	0.051	152.0	171.0	171.0	-	171.0	-	29.3	32.1	19.4
2021b	Beam 4	2400	200	200	159	3	226	9.0	54	535	633	1.18	0.71	0.070	175.0	183.0	183.0	-	183.0	-	27.4	33.0	21.1
2021b	Beam 5	2400	200	200	159	3	226	9.0	54	535	633	1.18	0.71	0.070	106.0	124.0	146.0	-	124.0	-	27.4	33.0	21.1
2021b	Beam 6	2400	200	200	159	3	226	9.0	54	535	633	1.18	0.71	0.070	133.0	146.0	146.0	-	146.0	-	27.4	33.0	21.1
2021b	Beam 7	2400	200	200	159	3	226	9.0	54	535	633	1.18	0.71	0.070	180.0	182.0	182.0	-	182.0	-	27.4	33.0	21.1
2021b	Beam 8	2400	200	200	159	3	226	9.0	54	535	633	1.18	0.71	0.070	162.0	170.0	170.0	-	170.0	-	27.4	33.0	21.1
2021b	Beam 9	2400	200	200	159	3	226	9.0	54	535	633	1.18	0.71	0.070	139.0	177.0	177.0	-	177.0	-	27.4	33.0	21.1
2023	B-02	2600	100	200	160	2	57	2.9	55	546	588	1.0	0.4	0.0	9.9	13.6	15.2	16.3	17.0	-	30.1	15.9	9.3
2023	B-04	2600	100	200	160	2	101	9.8	55	588	688	1.2	0.6	0.1	22.0	30.6	39.4	41.1	60.4	-	44.7	54.7	27.1
2023	B-06	2600	100	200	160	2	157	11.6	55	569	699	1.2	1.0	0.1	22.4	32.1	33.2	35.6	40.8	-	38.7	36.2	24.6

[1] $w_s \approx 0.8 \cdot \frac{x}{d}$

[2] $\frac{L}{a} = 2\ (3-point\ bending\ test), \frac{L}{a} = 3\ (4-point\ bending\ test)$

4 FUNDAMENTALS OF DYNAMICS

4.1 Introduction

Dynamically loaded structures may be affected differently compared to statically loaded. This difference can especially be observed when the structure is subjected to an external load which has a high intensity during a short period (Johansson, 2000). The dynamic load can be categorized either as characteristic impulse loading or characteristic pressure loading. Characteristic impulse loading can be defined as a time-dependent load with infinitely high pressure and infinitesimal duration. In contrast, characteristic pressure load is a pressure load with infinite duration, see Figure 4.1. Realistically, the impulse load occurs amidst these two extreme cases. In this thesis, it is mainly the impulse loading that is of interest in the form of drop-weight impact which will be treated in Section 4.2.

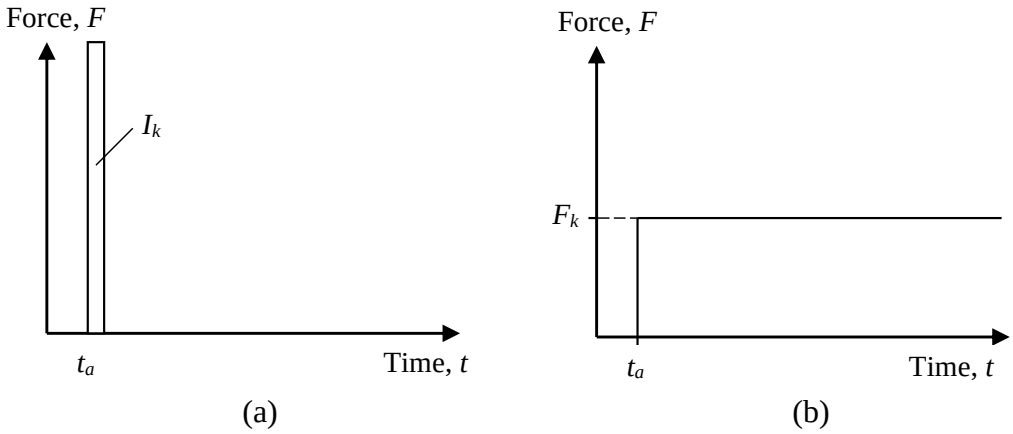

Figure 4.1 *Image (a) shows an impulse load with infinitely high pressure and infinitesimal duration. (b) shows a characteristic pressure load with an infinite duration (Johansson & Laine, 2012).*

4.2 Impulse

The impulse load is defined as an external force that changes the momentum of a body (Johansson & Laine, 2012). Momentum can be defined as

$$p = m \cdot v \tag{4.1}$$

where m = mass [kg]
v = velocity [m/s]

The change of momentum of a body acting under the time $t_0 \leq t \leq t_1$ with an initial velocity v_0 can be calculated as

$$m \cdot v_1 = m \cdot v_0 + \int_{t_0}^{t_1} F(t)dt \tag{4.2}$$

From Equation (4.2) the impulse can be expressed as

$$I = \Delta p = m \cdot \Delta v = \int_{t_0}^{t} F(t)dt \tag{4.3}$$

4.3 Work and Kinetic Energy

If a body is subjected to a Force F and gives a displacement u, the work can be expressed as

$$W = F \cdot u \cdot \cos\varphi = F_x \cdot u \tag{4.4}$$

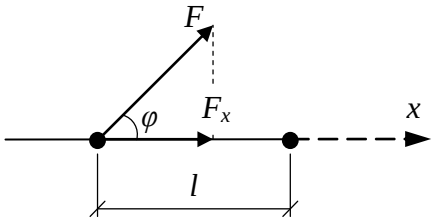

Figure 4.2 Schematic illustration of a particle in motion (Johansson & Laine, 2012).

Where φ is the angle between the force and displacement direction, see Figure 4.2. For a variable force, the work can be expressed as

$$W = \int_0^u F_x(x)dx \tag{4.5}$$

The kinetic energy E_k for a body with a mass m and a velocity, v can be expressed as

$$E_k = \frac{m \cdot v^2}{2} \tag{4.6}$$

Thus, the external work can be defined as

$$W_e = \Delta E_k = \frac{m \cdot v_1^2}{2} - \frac{m \cdot v_0^2}{2} \tag{4.7}$$

By combining Equations (4.3) and (4.7) the external work can be described as

$$W_e = \frac{I_k^2}{2 \cdot m} \tag{4.8}$$

4.4 Internal Work and Energy Equilibrium

For a concrete structure subjected to impulse loading the internal resistance is of interest to withstand the external load (Johansson & Laine, 2012). Thus, the internal energy absorption is of interest, in contrast to load capacity which is the case for a

statically loaded structure. This means that the internal work must be balanced with external work to reach energy equilibrium. This is illustrated in Figure 4.3, where the integrals for external and internal work are shown.

The ability to absorb energy for a structure is dependent on the interplay between the force and the resulting deformation (Johansson & Laine, 2012). That in turn is dependent on the material and geometry properties of a structure. For an impulse-loaded structure, a large deformation capacity is more desirable than having a large load capacity.

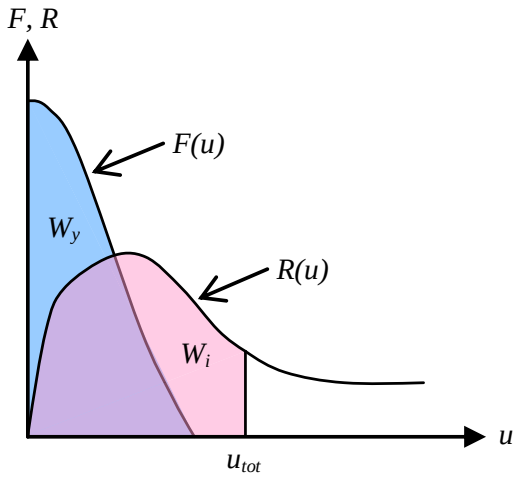

Figure 4.3 *An illustration of the integrated areas, where W_i is the internal work and W_y is the external work (Johansson & Laine, 2012).*

The internal work can be explained with simplified responses divided into elastic, plastic and elastoplastic, see Figure 4.4.

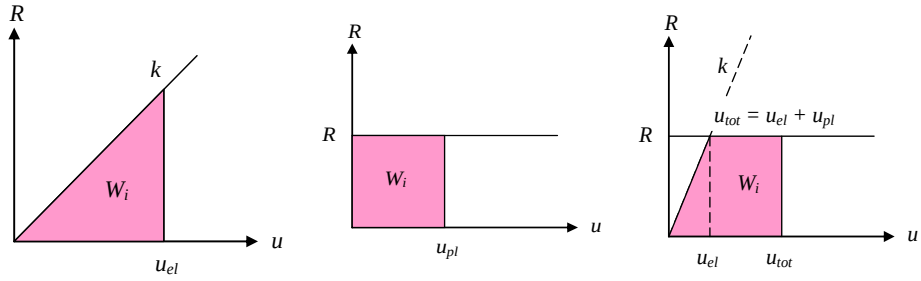

Figure 4.4 *Illustrations of the different responses where (a) is the elastic response, (b) is the plastic response and (c) is the elasto-plastic response (Johansson & Laine, 2012).*

4.4.1 Elastic Response

The internal work with linear elastic response can be calculated with Equation (4.9). As mentioned in Section 3.2 the resistance force is in proportion to displacement and the stiffness is assumed to be constant.

$$W_i = \frac{k \cdot u_{el}^2}{2} \tag{4.9}$$

where k = constant stiffness [N/m]
u_{el} = elastic deformation [m]

Elastic deformation, u_{el}, is needed to resist the external work which can be derived by using equilibrium, i.e., $W_i = W_e$ and Equations (4.8) and (4.9)

$$u_{el} = \frac{I_k}{m \cdot \omega} \tag{4.10}$$

Where ω is the angular eigenfrequency of the system expressed as

$$\omega = \sqrt{k/m} \tag{4.11}$$

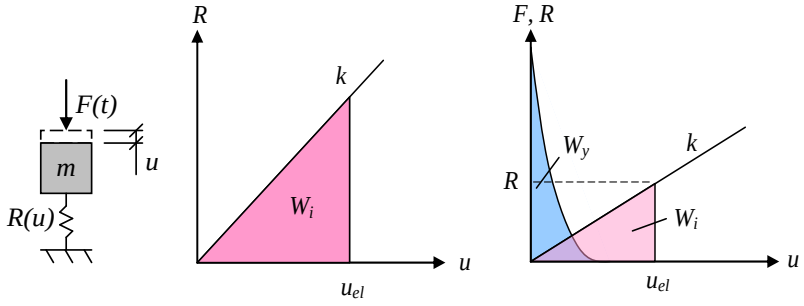

Figure 4.5 *An illustration of the system with a linear elastic response: (a) SDOF-system, (b) force-deflection curve, (c) energy equilibrium between the internal work W_i and the external work W_y (Johansson & Laine, 2012).*

4.4.2 Plastic Response

The internal work with plastic response can be expressed as Equation (4.12). As mentioned in Section 3.3 the resisting force can be assumed as constant.

$$W_i = R(u_{pl}) \cdot u_{pl} = R \cdot u_{pl} \tag{4.12}$$

The plastic deformation is needed to resist the external work and can be expressed as Equation (4.13)

$$u_{pl} = \frac{I^2}{2 \cdot m \cdot R} \tag{4.13}$$

where I = impulse
$m = mass$
R = resisting force

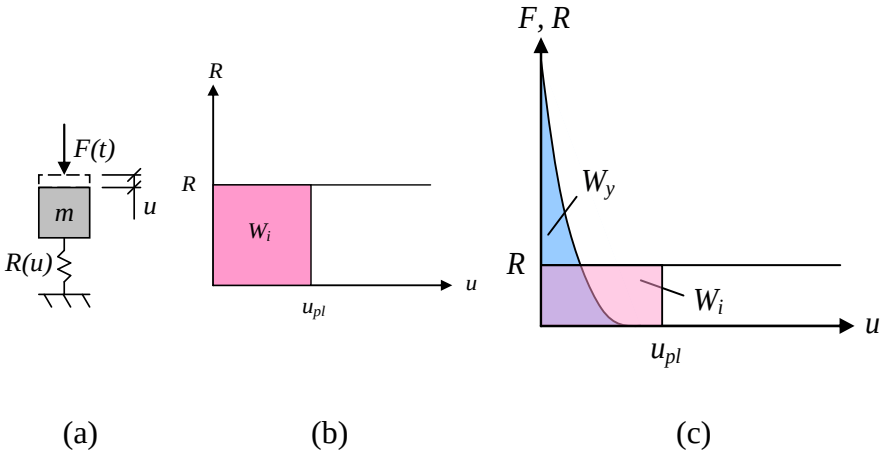

(a) (b) (c)

Figure 4.6 *An illustration of the system with a plastic response: (a) SDOF-system, (b) force-deflection curve, (c) energy equilibrium between the internal work W_i and the external work W_y (Johansson & Laine, 2012).*

4.4.3 Elasto-Plastic Response

The internal work for elasto-plastic response can be calculated according to Equation (4.14). As mentioned in Section 3.4 this response is a more representative way to describe the behaviour of a material, see Figure 4.7.

$$W_i = \frac{1}{2} \cdot R \cdot u_{el,1} + R \cdot u_{pl,1} = \frac{R}{2} \cdot \left(u_{el,1} + 2 \cdot u_{pl,1}\right) \tag{4.14}$$

where R = reaction force
$u_{el,1}$= elastic deformation for elasto-plastic response
$u_{pl,1}$= plastic deformation for elasto-plastic response

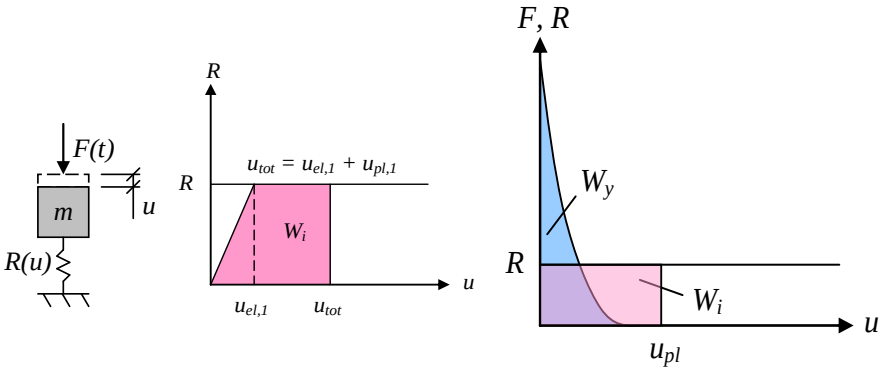

(a) (b) (c)

Figure 4.7 *An illustration of the system with an elasto-plastic response: (a) SDOF-system, (b) force-deflection curve, (c) energy equilibrium between the internal work W_i and the external work W_y (Johansson & Laine, 2012).*

The total deformation can be divided into an elastic and a plastic part. The elastic part can be expressed as

$$u_{el,1} = \frac{R}{k} \tag{4.15}$$

where R = resisting force
k = stiffness

The plastic deformation can be expressed as

$$u_{pl,1} = \frac{I^2}{2 \cdot m \cdot R} - \frac{u_{el,1}}{2} \tag{4.16}$$

where I = impulse
m = mass
R = constant capacity
$u_{el,1}$ = limit for the elastic deformation in elasto-plastic response

4.5 Impact Theory

A concrete structure subjected to impulse loading can be described with masses m_1, m_2 and velocities v_1, v_2, see Figure 4.8. In impact theory the collision between objects can be divided in to two extreme cases, elastic, or plastic behaviour. In the elastic case, the velocities will be different after impact, however, in the plastic case the velocities will be the same, see Figure 4.9. The momentum and kinetic energy will be used to study the behaviour of impulse loading.

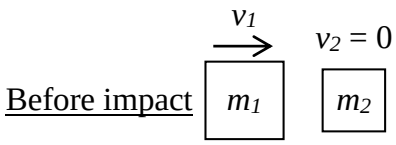

Figure 4.8 *Shows a schematic illustration before the impact of impulse loading. Inspired by (Johansson & Laine, 2012).*

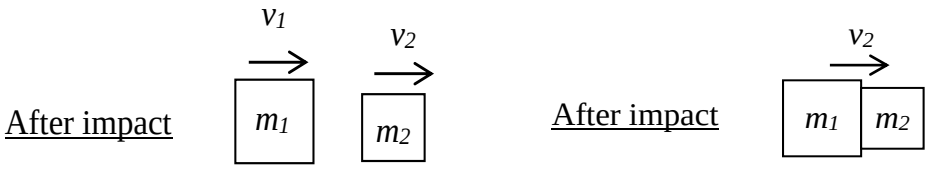

(a) Elastic collision (b) Plastic collision

Figure 4.9 *An illustration after the impact of impulse loading. Where a) illustrates an elastic collision and b) a plastic collision. Inspired by (Johansson & Laine, 2012).*

4.5.1 Elastic Impact

According to Johansson (2014) the momentum and kinetic energy for elastic impact remains the same after impact. The velocities for the bodies after impact can be calculated according to Equations (4.17) and (4.18).

$$v_{el,1} = \frac{m_1 - m_2}{m_1 + m_2} \cdot v_0 \tag{4.17}$$

$$v_{el,2} = \frac{2 \cdot m_1}{m_1 + m_2} \cdot v_0 \tag{4.18}$$

where v_0 = velocity for particle one before impact
$v_{el,1}$ = velocity for particle one after impact
$v_{el,2}$= velocity for particle two after impact
m_1= mass for particle one
m_2= mass for particle two

The kinetic energy for the bodies can be calculated according to Equations (4.19) and (4.20)

$$E_{k,el,1} = \frac{m_1 \cdot v_{el,1}^2}{2} = \cdots = \left(\frac{m_1 - m_2}{m_1 + m_2}\right)^2 \cdot E_{k,0} \tag{4.19}$$

$$E_{k,el,2} = \frac{m_2 \cdot v_{el,2}^2}{2} = \cdots = \frac{4 \cdot m_1 \cdot m_2}{(m_1 + m_2)^2} \cdot E_{k,0} \tag{4.20}$$

where $E_{k,0}$ = kinetic energy before impact

$$E_{k,0} = \frac{m \cdot v_0^2}{2} \tag{4.21}$$

4.5.2 Plastic Impact

For a plastic impact, the momentum will remain the same, however, the kinetic energy will decrease. The reason for the decrease in kinetic energy is because of the transformation to potential energy. The plastic impact results in plastic work which occur in the contact surface between the bodies. The velocities for plastic impact can be calculated according to Equation (4.22).

$$v_{pl} = v_{1,pl} = v_{2,pl} = \frac{m_1}{m_1 + m_2} \cdot v_0 \tag{4.22}$$

where v_0 = velocity for particle one before impact
$v_{pl,1}$= velocity for particle one after impact
$v_{pl,2}$= velocity for particle two after impact
m_1= mass for particle one
m_2= mass for particle two

The kinetic energy can be calculated according to Equation (4.23)

$$E_{k,pl,12} = \frac{(m_1 + m_2) \cdot v_{pl}^2}{2} = \cdots = \frac{m_1}{m_1 + m_2} \cdot E_{k,0} \tag{4.23}$$

4.6 Response during Repeated Impacts

4.6.1 Introduction

To be able to explain the structural response when a concrete structure is subjected to repeated loading the equivalent impulse load with an elasto-plastic response is treated. The elastic response can be neglected in the analysis, therefore only the plastic response in the elasto-plastic response will be treated. It is assumed that the residual deformation capacity will not decrease when the response goes back to the original position. The residual strength of the concrete specimen is finally assessed to determine the structural response for repeated loading.

4.6.2 Plastic and Elasto-Plastic Response

The response for a single impulse load is treated in Section 4.2, where elasto-plastic is a more representative way to describe the behaviour of concrete specimens. In Figure 4.10 an illustration of a structure with mass m can be seen in the force-displacement relation.

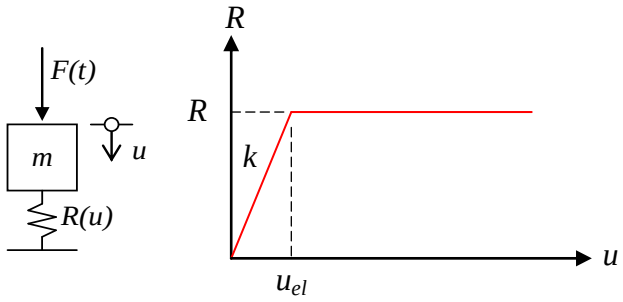

Figure 4.10 An illustration of a structure with the mass m and its force-displacement relation (Johansson & Laine, 2012).

The external work can be calculated using energy equilibrium and Equation (4.14) where a structure is subjected to impulse loading.

$$W_{e,1} = W_{i,1} = W_{1,el} + W_{1,pl} = \frac{R_m}{2} \cdot (u_{1,el} + 2 \cdot u_{1,pl}) \tag{4.24}$$

The total deformation for the impulse load can be expressed as

$$u_1 = u_{1,el} + u_{1,pl} \tag{4.25}$$

The behaviour of the structure subjected to impulse can be seen in Figure 4.11.

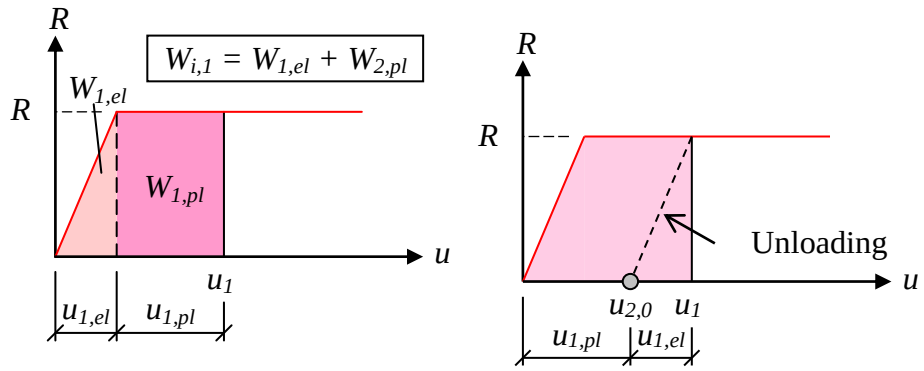

(a) Elasto-plastic response (b) Lasting deformations

Figure 4.11 *Figure (a) shows an elasto-plastic response after first impact and (b) shows lasting deformation after being unloaded* (Johansson, 2014).

When the impulse load is removed the elastic deformation return to its initial stage and the plastic deformation remain which can be expressed as

$$u_{2,0} = u_1 - u_{1,el} = u_{1,pl} \tag{4.26}$$

When the structure is subjected to a subsequent impulse load I_2 the deformation will start from the previous plastic deformation, see Figure 4.12.

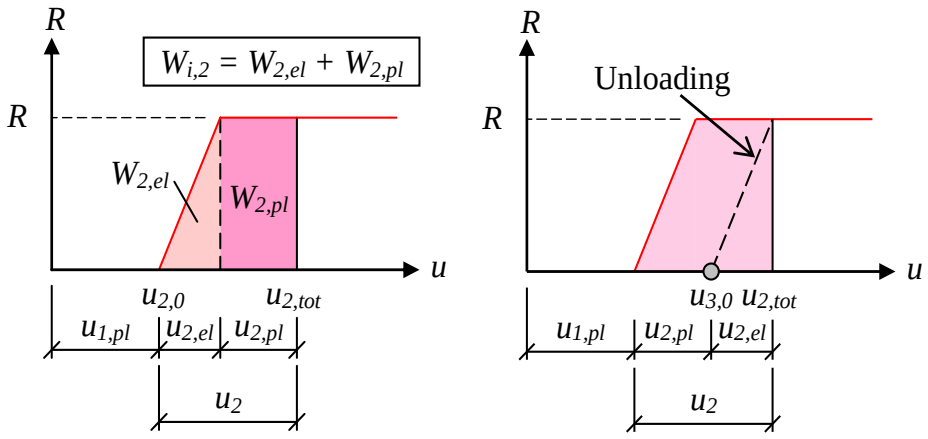

Figure 4.12 *illustrating the phenomena where the new impulse load will start from the previous lasting deformation* (Johansson, 2014).

The new external work can be calculated according to Equation (4.27)

$$W_{e,2} = \frac{R_m}{2} \cdot (u_{2,el} + 2 \cdot u_{2,pl}) \tag{4.27}$$

The deformation u_2 from I_2 and the total deformation $u_{2,tot}$ can be expressed as

$$u_2 = u_{2,el} + u_{2,pl} \tag{4.28}$$

$$u_{2,tot} = u_{2,0} + u_2 = u_{1,pl} + u_{2,el} + u_{2,pl} \tag{4.29}$$

When the impulse load is removed the total deformation can be expressed as

$$u_{3,0} = u_{1,pl} + u_{2,pl} \tag{4.30}$$

4.6.3 Equivalent Impulse Load for Elasto-Plastic Response

By using an equivalent impulse load I_{tot}, the subsequent load that acts on a structure can be converted to a single impulse load (Johansson & Laine, 2012). The equivalent impulse load is only considered for the elasto-plastic case. For a structure with an elasto-plastic response that is subjected to an impulse loading that does not reach the plastic region, the current impulse load will not contribute to an equivalent impulse load. The magnitude of the equivalent impulse load is expressed as Equation (4.40) using the following equations

$$W_{y,i} = W_{i,el} = \frac{I_I^2}{2m} \tag{4.31}$$

where $W_{y,i}$ can be expressed as in Equation (4.8) and $W_{i,el}$ can be expressed according to Equations (4.32) and (4.33)

$$W_{i,el} = \frac{R \cdot u_{i,el}}{2} \tag{4.32}$$

or

$$W_{i,el} = \frac{R^2}{2 \cdot k} \tag{4.33}$$

where $u_{i,el} = \frac{R}{k}$
$k =$ elastic stiffness of the structure

The maximum allowed impulse load where the structure does not sustain any damage can be calculated according to Equation (4.34), by combining energy equilibrium and Equation (4.8)

$$I_{el} = \sqrt{R \cdot m \cdot u_{el}} = R \cdot \sqrt{\frac{m}{k}} = \frac{R}{\omega} \tag{4.34}$$

where ω = the angular frequency
m = the mass

If the impulse load is larger than I_{el} the structure will have lasting damage that is considered in the calculation. The total external work can be expressed according to Equation (4.35)

$$W_{y,tot} = n \cdot W_{el} + \sum_{i=1}^{n} W_{i,pl} \tag{4.35}$$

By combining Equations (4.12), (4.31) and (4.32) it can be expressed as

$$\frac{1}{2 \cdot m} \sum_{i=1}^{n} I_i^2 = R\left(n \cdot \frac{u_{el}}{2} + u_{tot,pl}\right) \tag{4.36}$$

The plastic deformation can be derived from Equation (4.36)

$$u_{tot,pl} = \frac{1}{2} \cdot \left(\frac{1}{R \cdot m} \sum_{i=1}^{n} I_i^2 - n \cdot u_{el}\right) \tag{4.37}$$

The plastic deformation can also be expressed with an equivalent impulse load as

$$u_{tot,pl} = \frac{1}{2}\left(\frac{1}{R \cdot m} \cdot I_{tot}^2 - u_{el}\right) \tag{4.38}$$

By combining Equations (4.37) and (4.38) gives

$$I_{tot} = \sqrt{\sum_{i=1}^{n} I_i^2 - (n-1) \cdot R \cdot m \cdot u_{el}} \tag{4.39}$$

Hence, Equation (4.40) can now be expressed as

$$I_{tot} = \sqrt{\sum_{i=1}^{n} I_i^2 - (n-1) \cdot I_{el}^2} = \sqrt{\sum_{i=1}^{n} (I_i^2 - I_{el}^2) + I_{el}^2} \tag{4.40}$$

Where if $I_1 > I_{el}$ then the impulse load should be considered.

4.6.4 Residual Strength

The magnitude of an impulse load can be calculated with Equation (4.41) when considering a damaged structure before it reaches failure. If the studied structure has sustained $n - 1$ impulses, the magnitude of the next impulse load can be expressed as

$$I_n = \sqrt{I_{tot}^2 - \sum_{i=1}^{n} (I_i^2 - I_{el}^2)} \tag{4.41}$$

If the remaining plastic deformation $u_{tot,pl}$ and the remaining deformation $u_{n,0}$ is known, before the next impulse load is applied, the magnitude of the next impulse load be expressed as

$$I_n = \sqrt{2 \cdot R \cdot m \cdot u_{n,pl}} \tag{4.42}$$

where $u_{n,pl} = u_{tot,pl} - u_{n,0}$

5 DISCRETE MODEL FOR DYNAMIC ANALYSIS

5.1 Introduction

To describe the response of a reinforced beam subjected to impulse loading a single-degree-of-freedom-system (SDOF) can be used respectively for the beam and the drop-weight. To get a better understanding of the behaviour of the beam the SDOF-system is transformed into a two-degree-of-freedom (2DOF). The theory in this section is based on (Johansson & Laine, 2012) and (Johansson, 2014).

5.2 SDOF System

A dynamic single degree of freedom referred to as a SDOF-system, consisting of a mass m that is subjected to time-dependent force $F(t)$ (Johansson and Laine, 2012). For the system to be in equilibrium there is a static and dynamic force denoted as $R_{sta}(u)\ and\ R_{dyn}(\dot{u})$ respectively, to resist the external force. The resistance force consists of an internal static resistance $R(u)$ and viscous damper $c(\dot{u})$, see Figure 5.1a. For impulse loading, the duration is relatively short and thus, the viscous damper can be assumed to be neglected. Hence, the dynamic force will also be neglected because it is dependent on viscous damper. This leads to that the inner resistance force together with the maximum displacement is of interest which can be seen in Figure 5.1b.

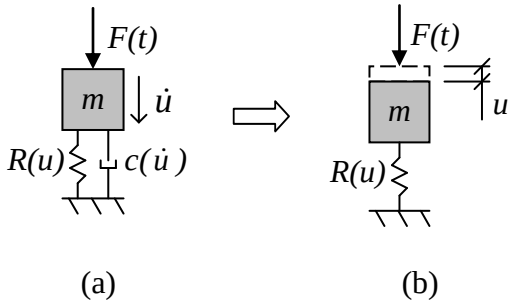

Figure 5.1 An illustration (a) of an SDOF system and (b) where the viscous damper is neglected (Johansson & Laine, 2012).

5.2.1 Central Difference Method

To solve equations of motion presented in Section 5.4.1 for a structure subjected to dynamic loading, the central difference method is an explicit method that is used (Johansson, 2012). This is used to obtain an approximate solution to solve differential equations in a 2DOF system. As previously explained the damping c is assumed to be neglected and is therefore not considered for the central difference method calculations which gives a conservative approximation.

5.3 Transforming the Beam to SDOF

To be able to apply the previously explained SDOF-system for an impulse-loaded beam, the beam together with external loads need to be transformed into an equivalent

SDOF-system. A beam with a linear elastic material property and subjected to static load will have a deformed shape which is a function of the load arrangement and the boundary condition (Johansson & Laine, 2012). The deformed shape remains the same regardless of the load level, which leads to the deflections along the beam can be described with only one point, the system point u_s, see Figure 5.2. It is common to place the system point where the maximum deflections occur or place the system point in the middle of the beam. The deflection u_s at the system point will be equal to the deflection u_{SDOF} in SDOF system.

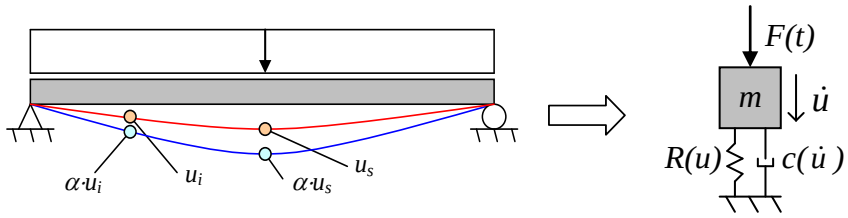

Figure 5.2 The beam is transformed into an equivalent SDOF-system (Johansson & Laine, 2012).

To transform a beam to an equivalent SDOF system the mass m, damping c, resistance force $R(u)$ and external force $F(t)$ are applied in the system point, see Figure 5.3.

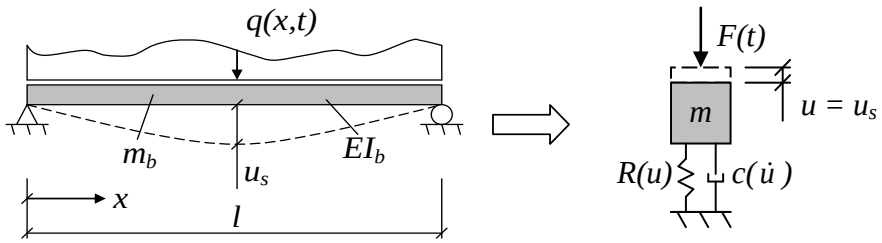

Figure 5.3 Parameters for a beam are transformed into a SDOF-system (Johansson & Laine, 2012).

Furthermore, transformations factors κ_F, κ_m, κ_k are multiplied with the external load, mass, and stiffness of the beam, respectively (Johansson & Laine, 2012). The implementation of transformation factors is used to ascertain that the kinetic energy and work subjected to the beam, is equivalent to the kinetic energy and work in the SDOF-system.

The work in the SDOF system is dependent on the internal resistance $R(u)$, the external force $F(t)$, and kinetic energy is dependent on the mass. The energy of the beam is dependent on the external force, internal resistance, and mass. With a linear elastic response, the transformation between the beam and the SDOF system can be expressed as

$$m = \kappa_m \cdot m_b \tag{5.1}$$

$$c = \kappa_c \cdot c_b \tag{5.2}$$

$$k = \kappa_k \cdot k_b \tag{5.3}$$

$$F = \kappa_F \cdot F_b \tag{5.4}$$

where c_b= damping of the beam
m_b= mass of the beam
k_b= stiffness of the beam
κ_m= transformation factor for the mass
κ_c = transformation factor for the dampening
κ_k = transformation factor for the stiffness
κ_F = transformation factor of the force

Hence, for an arbitrary system, it can also be expressed as

$$m \cdot \ddot{u} + c \cdot \dot{u} + k \cdot u = F(t) \tag{5.5}$$

to

$$\kappa_m \cdot m_b \cdot \ddot{u} + \kappa_c \cdot c_b \cdot \dot{u} + \kappa_k \cdot k_b \cdot u = \kappa_F \cdot F_b(t) \tag{5.6}$$

Since an impulse loading occurs in a short duration, the dampening can be assumed to be neglected, therefore, the Equations (5.5) and (5.6) can be rewritten as

$$\kappa_m \cdot m_b \cdot \ddot{u} + \kappa_k \cdot R_b(u) = \kappa_F \cdot F_b(t) \tag{5.7}$$

where R_b = response of the beam subjected to static loading.

Thus, Equation (5.7) can be rewritten as

$$\frac{\kappa_m}{\kappa_F} \cdot m_b \cdot \ddot{u} + \frac{\kappa_k}{\kappa_F} \cdot k_b \cdot u = F_b(t) \tag{5.8}$$

According to (Johansson & Ekengren, 2014) the factor κ_k can be assumed to equal κ_F. Hence the equation can now be expressed as

$$\kappa_{mF} \cdot m_b \cdot \ddot{u} + k_b \cdot u = F_b(t) \tag{5.9}$$

where $\kappa_{mF} = \frac{\kappa_m}{\kappa_F}$

The transformation factor depends on the loading conditions, boundary condition and deformed shape i.e., elastic, or plastic case. In this thesis only simply supported cases subjected to a point load in the middle are considered. These conditions are presented in Table 5.1.

Table 5.1 *Transformation factors for a beam subjected to a 3-point bending (Johansson & Laine, 2012).*

Strain Range	Load Factor, κ_F	Mass Factor, κ_m	Load-mass factor, κ_{mF}
Elastic	1.00	0.49	0.49
Plastic	1.00	0.33	0.33

5.4 2DOF-System

The collision between the drop-weight and the beam can be described with the SDOF-system as previously explained in Section 5.2. To get a more realistic interpretation of the beam subjected to impulse loading the separated system can be coupled by using a 2DOF-system, see Figure 5.4.

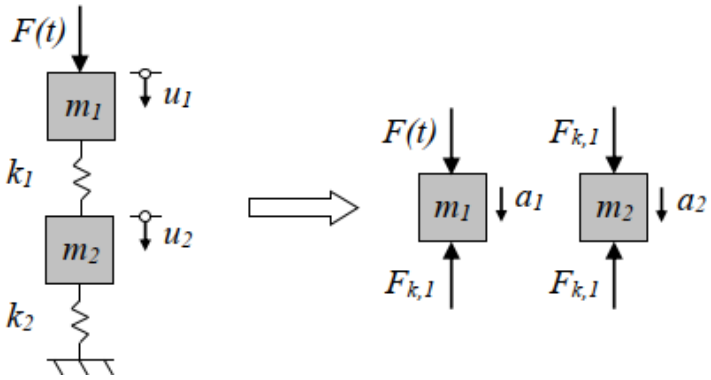

Figure 5.4 *An illustration of the separated system being coupled using a 2DOF-system (Jönsson & Stenseke, 2018).*

5.4.1 Equation of Motion For a 2DOF System

To describe the impulse loading acting on the beam a 2DOF-system is discretized into two free bodies, one SDOF-system for the beam and one SDOF-system for the drop-weight, see Figure 5.4.

By using Newton's second law with force equilibrium, Equations (5.10) and (5.11) can be expressed as

$$F_1(t) - F_{k,1} = m_1 \cdot \ddot{u}_1 \tag{5.10}$$

$$F_2(t) - F_{k,2} = m_2 \cdot \ddot{u}_2 \tag{5.11}$$

Furthermore, these Equations can be expressed as Equations (5.12) and (5.13) when incorporating the stiffness of the springs, and displacement.

$$m_1 \cdot \ddot{u_1} + k_1(u_1 - u_2) = F_1(t) \tag{5.12}$$

$$m_2 \cdot \ddot{u_2} + k_2 \cdot u_2 + k_1(u_1 - u_2) = F_2(t) \tag{5.13}$$

Equations (5.12) and (5.13) can also be expressed in a matrix as Equation (5.14)

$$\begin{bmatrix} m_1 & 0 \\ 0 & m_2 \end{bmatrix} \begin{bmatrix} \ddot{u_1} \\ \ddot{u_2} \end{bmatrix} + \begin{bmatrix} k_1 & -k_1 \\ -k_1 & k_2 + k_1 \end{bmatrix} \begin{bmatrix} u_1 \\ u_2 \end{bmatrix} = \begin{bmatrix} F_1(t) \\ F_2(t) \end{bmatrix} \tag{5.14}$$

Or

$$\boldsymbol{M\ddot{u} + Ku = F(t)} \tag{5.15}$$

5.4.2 2DOF for a Reinforced Beam and Drop-Weight

To explain the impact of the drop-weight with the reinforced beam, transformation factors from Section 5.3 is incorporated with Equation (5.14). The external force acting on the two bodies is assumed to be neglected. The impulse loading is described as the initial velocity of body 1, in this case, the drop-weight. For elastic response, it gives the following Equation (5.16)

$$\begin{bmatrix} \kappa_{m,1} m_1 & 0 \\ 0 & \kappa_{m,2} m_2 \end{bmatrix} \begin{bmatrix} \ddot{u_1} \\ u_2 \end{bmatrix} + \begin{bmatrix} \kappa_{F,1} k_1 & -\kappa_{F,1} k_1 \\ -\kappa_{F,1} k_1 & \kappa_{F,1} k_2 + \kappa_{F,2} k_1 \end{bmatrix} \begin{bmatrix} u_1 \\ u_2 \end{bmatrix} = \begin{bmatrix} 0 \\ 0 \end{bmatrix} \tag{5.16}$$

For an elasto-plastic response, it can be expressed as

$$\begin{bmatrix} \kappa_{m,1} m_1 & 0 \\ 0 & \kappa_{m,2} m_2 \end{bmatrix} \begin{bmatrix} \ddot{u_1} \\ \ddot{u_2} \end{bmatrix} + \begin{bmatrix} R_1 & -R_1 \\ -R_1 & R_1 + R_2 \end{bmatrix} = \begin{bmatrix} 0 \\ 0 \end{bmatrix} \tag{5.17}$$

To get a representative understanding of the elasto-plastic response for the 2DOF-system, the conditions presented in Section 3.4 need to be expanded. In theory, when the drop-weight gets in contact with the reinforced concrete, the drop-weight moves upwards after the impact and creates tension in the spring system. In reality, there is no spring between the drop-weight and reinforced beams, hence, no tension between the bodies. This behaviour can be considered by putting the stiffness equal to zero as expressed in Equation (5.18).

$$R_i = \begin{cases} k_i \cdot u \; if \; u \leq u_{el} \\ R_{m,i} \; if \; u > u_{el} \\ 0 \; if \; u \leq 0 \end{cases} \tag{5.18}$$

The internal resistance for the reinforced beam and the drop-weight are derived differently. For a reinforced concrete beam, the internal resistance can be derived from the maximum moment in the ultimate limit state for a simply supported beam with a point load at the midspan. This can be expressed as in Equation (5.19).

$$R_{m,2} = \frac{4 \cdot M_u}{L} \tag{5.19}$$

where M_u = moment in ultimate limit state
L = span length

During impact loading the beam is also affected by its self-weight which will result in lower internal resistance, this is illustrated in Figure 5.5. The reduction of internal resistance can be expressed in Equation (5.20)

$$R_{m,2,red} = R_{m,2} - \frac{g_{beam} \cdot L}{2} \tag{5.20}$$

where g_{beam} = self-weight of the beam

The stiffness of the beam, k_2 can be calculated with elementary cases expressed as

$$k_2 = \frac{48 E_{cm} I_{II}}{L^3} \tag{5.21}$$

where I_{II} = the moment inertia in state II

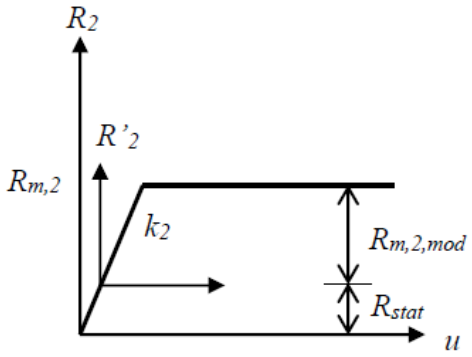

Figure 5.5 An illustration showing the reduction in internal resistance due to static load from self-weight (Lozano & Makdesi, 2017).

To determine the internal resistance of the drop-weight the strength of the material is multiplied by the impact area as expressed in Equation (5.22) (Lovén & Svavarsdóttir, 2016).

$$R_{m.1} = f \cdot A_{imp} \tag{5.22}$$

The strength of material f, can either be the compressive strength of concrete f_{cm} or yielding of the reinforcement f_{ym}, which can be expressed as

$$f_{cm} \cdot A_{imp} \leq R_{m,1} \leq f_{ym} \cdot A_{imp} \tag{5.23}$$

The stiffness of the drop-weight can be calculated as

$$k_1 = \frac{E_{sm} A}{L} \tag{5.24}$$

where E_{sm}= young's modulus for the steel
A = cross-section of the drop-weight
L = length of the drop-weight

6 EXPERIMENT PROCEDURE

6.1 Introduction

The experimental procedure in this project was to create 18 beams with varying reinforcement of 6, 8, 10 mm, see Table 6.1. Afterwards, these beams were divided into four different series based on type of loading and what drop-weight they were subjected to; thus, named Reference beams, Series-I10, Series-I20, and Series-I40 and the drop height was 5.0 meters for all beams tested dynamically. To examine the residual response of the dynamically tested beams, they were statically tested to failure and static tests were performed on undamaged beams to act as reference beam; these tests were done using a 4-point bending test. Some dynamically tested beams suffered excessive damage and was deemed to be too damaged to be tested. Three undamaged beams were also tested in a 3-point bending test to measure the internal work.

Table 6.1 Name of the different concrete specimens. 3p = 3-point bending test and 4p = 4-point bending test

Type of Loading	**Series**	**Beam**	***Φ* [mm]**	**Drop-Weight [Kg]**	**Number of impacts**	**Static test**
Static	Reference beams	B-02 B-04 B-06	6 8 10	-	-	3p
		B-01 B-03 B-05	6 8 10	-	-	4p
Impact + Static	I10	B-07 B-08 B-09a B-09b B-10a B-10b	6 6 8 8 10 10	10	5 4 6 6 5 4	- 4p - - - 4p
	I20	B-11a B-11b B-12 B-13	6 6 8 10	20	1 1 2 2	- - 4p 4p
	I40	B-15 B-16	8 10	40	1 1	4p 4p

6.2 The Geometry of the Specimen

The length of the beams was 2800 mm with a cross-section of 100x200 mm, see Figure 6.1. Four longitudinal reinforcement was placed 40 mm from top respective bottom edge to the centre of reinforcement bars. This was done with three different configurations of ϕ6 mm, ϕ8 mm and ϕ10 mm, result in a vertical concrete cover of 37 mm, 36 mm, and 35 mm, respectively. The horizontal concrete cover is 20 mm for respective beam.

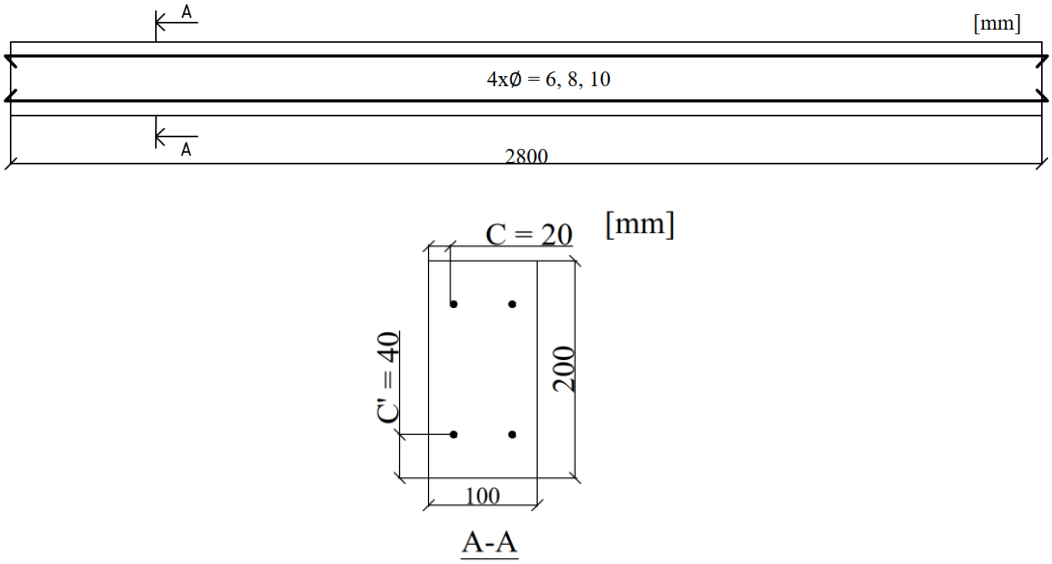

Figure 6.1 Geometry of the specimen.

6.3 Preparations before Casting

At first, the moulds were created according to Figure 6.1, the specific procedure of how these were made is described Appendix A. The newly made moulds were oiled thoroughly on all sides to prevent the concrete from sticking to the mould. Furthermore, to get the reinforcement to be at the desired location according to Figure 6.1, a T-section of timber board was used to keep the reinforcement in place, see Figure 6.2.

Figure 6.2 An illustration showing the T-section used to get an accurate concrete cover.

Thereafter, the reinforcement was cut, and the remaining edge pieces were kept to perform a pulling test, more on this in section. The reinforcement bars were placed into the designated predrilled holes and then placed into the T-section. The reinforcement was then hung up with steel wires and attached to an overlaying support, see Figure 6.3.

Figure 6.3 An illustration showcasing how the reinforcement was hung up with steel wires to the overlaying support.

Each concrete form had three overlaying supports placed on top of the form to keep the sides from buckling, two of them were placed 0.70 m from the edge and the third one was placed near the middle at approximately 1.3 m from the edge. This support was not directly placed exactly in the middle since this was the area in which the drop-weight was designed to impact the beam. Thus, an effort was made to keep the surface in this area as even as possible.

Besides the concrete moulds, forms for the material properties tests were also prepared. Both the concrete cubes used for the compressive strength tests and cubes to test the fracture energy with wedge-splitting tests were oiled thoroughly, see Figure 6.4.

Figure 6.4 An illustration of the casting of cubes used for wedge splitting tests.

6.4 Casting

A concrete class of C40/50 was ordered and delivered by Thomas concrete group; the material properties can be seen in Table 6.2. The beams were cast from the same concrete batch, and it contained a retarder to delay the hydration process to ensure workability throughout the entire casting process. Thereafter, the concrete was poured into the mould and vibrators were used to vibrate the concrete in the mould, see Figure 6.5.

Table 6.2 Shows the parameters for the concrete C40/50.

Concrete Class	Water Cement Ratio	Largest aggregate size	Consistency Class	Cement Type
C40/50	0.4	16 mm	S4	Std. Cem

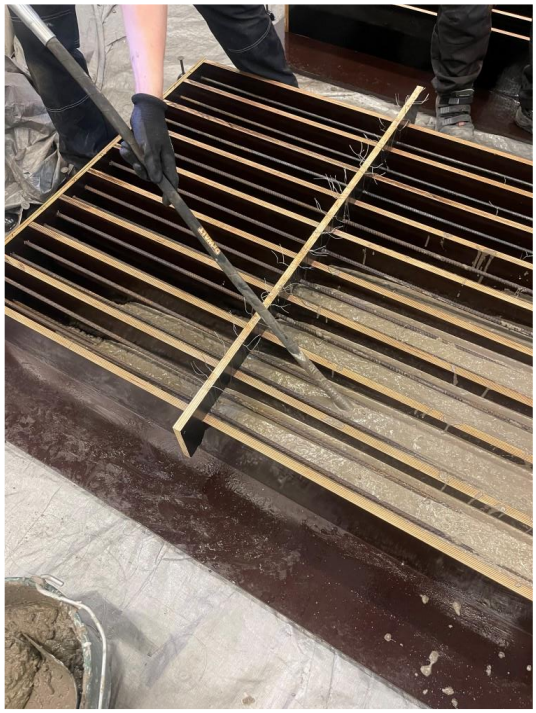

Figure 6.5 The vibrators that mixed the concrete in the forms.

Moreover, once the moulds had been filled with concrete, the surface was smoothed out and lifting anchors were placed at roughly 0.35 m from each beam edge, see Figure 6.6.

Figure 6.6 An illustration showing where the lift anchors were placed.

The filled concrete moulds were covered with a plastic sheet to prevent shrinkage cracks in the concrete during curing, see Figure 6.7. Finally, the previously mentioned material test moulds were filled, and material tests are further explained and evaluated under Section 6.6.

Figure 6.7 An illustration showing the covered concrete.

6.5 Painting of the Beams

The specimens were first painted white and then thoroughly painted with a specially made brush that creates a speckled pattern, see Figure 6.8. This was done to create an even distribution between the black dots and the white background since this is needed for the Digital Image Correlation (DIC) to study the beams under loading.

(a) (b)

Figure 6.8 (a) an illustration of speckled pattern and (b) painting brush.

6.6 Material Properties for Concrete

The concrete cubes were tested in two separate ways, one for compressive strength and one for fracture energy. All the concrete cubes for the compressive strength test and the fracture energy tests (WST-tests) were demoulded and placed in water approximately 72 hours from casting. From the compressive strength results, the tensile strength and modulus of elasticity could be calculated according to (2.2) and (2.8), respectively. The compressive and fracture energy tests were performed according to (CEN, 2009) and (Löfgren et. al., 2004), respectively.

The compressive strength tests were performed on 9 cubes in total, where 3 of them were tested at 28 days after casting, 3 cubes were tested at 57 days after casting, i.e., when the experiment occurred, and the remaining 3 cubes were tested at 64 days. The cylindric compressive strength is obtained by Equation (2.1) and can be seen in Appendix C. Three cubes with an indent were tested for fracture energy on day 57 after casting, see Figure 6.9. The results for both the compression tests and the fracture energy tests can be seen Appendix C.

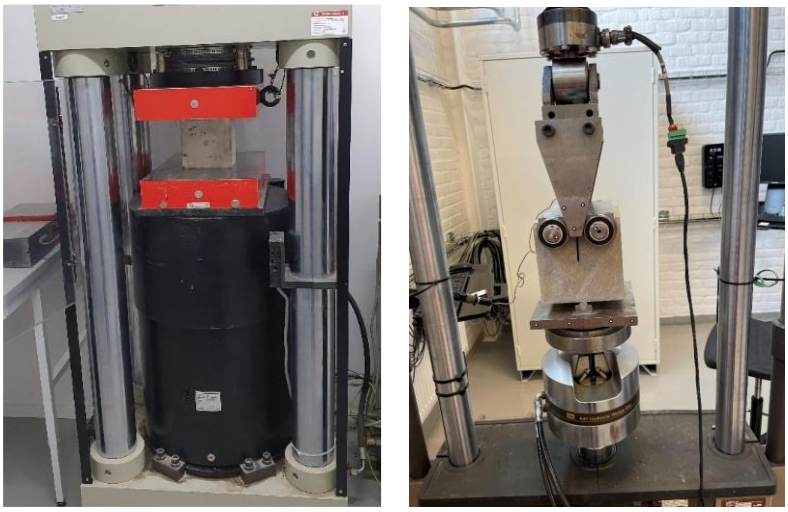

(a) (b)

Figure 6.9 Material test on concrete cubes: (a) compressive test and (b) Wedge splitting test.

6.7 Testing of Reinforcement

In this thesis three different types of reinforcement diameters are used namely, ϕ6 mm, ϕ8 mm and ϕ10 mm. Six reinforcement bars of each type were tested and evaluated to obtain steel properties, see Table B.1 to Table B.3. The stress-strain relationships can be seen in Appendix B. The tested reinforcement bars were roughly 330 mm long and was placed 50 mm into the machine on each side, this configuration can be seen in Figure 6.10. Two different deformation rates were used to obtain results for yielding and until the bar reaches failure. The yielding test was performed with a slower rate of 2 mm/min and an extensometer was used to obtain the strains in a detailed and accurate manner. Further, when yielding had been reached the extensometer was removed and a higher load rate of 20 mm/min was applied until the bar reached failure. The test results can be seen in section 8.3 and Appendix B.

Figure 6.10 The test-setup for the tensile tests.

6.8 Dynamic Testing and Set-up

The dynamic tests were carried out between day 55 and 62 after casting. The beams were subjected to impacts of varying drop-weights with a drop-height of 5 m, see Table 6.3. The three drop-weights had the shape of a cylinder with a diameter at the head of 200 mm and an accelerometer was placed inside, see Figure 6.11.

Table 6.3 The drop-weight parameters.

Drop-weight	Mass [kg]	Diameter [mm]	Length [mm]
1	10	120	112
2	20	120	227
3	40	120	458

Figure 6.11 An image showing the different drop-weights.

The beams were placed onto roller supports that restricted the orthogonal movement from the painted surface and downward movement, although the beams were allowed to freely move upwards, see Figure 6.12. The roller supports were fixed to the concrete pavement to ensure that the beams were placed symmetrically and thus, that the drop-weight would impact the beam in the same spot every time. The test set-up consisted of two high-speed cameras, where the first camera captured roughly half the beam with frame rate of 5000 fps. The second camera captured the drop-weight at a frame rate of 36000 fps.

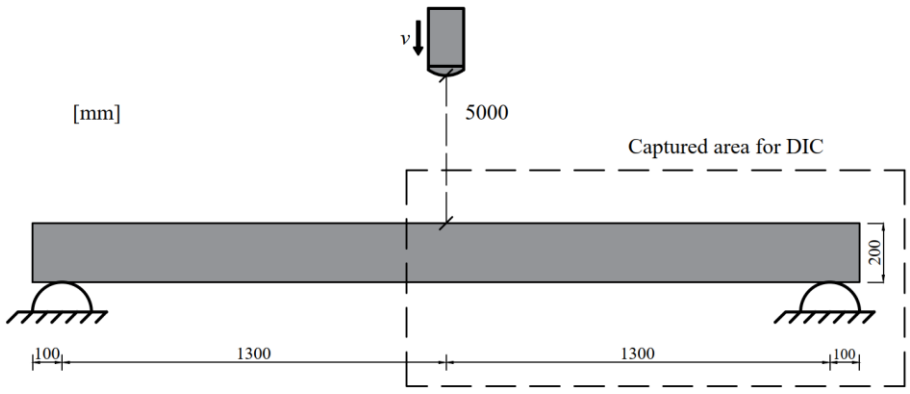

Figure 6.12 Showing the dynamic test setup.

6.9 Static Testing and Set-up

The aim for the static tests was to evaluate the residual capacity of beams that were tested dynamically and compare them to reference beams with the reinforcement configuration. The static tests were performed on two separate days, the 4-point bending tests for the reference beams were performed on 63 days after casting and the damaged beams 67 days after casting. Furthermore, the 3-point bending tests were performed on day 68 after casting.

A camera was set-up for the static tests, see Figure 6.13. The camera was rolled to a marked spot, roughly 1.4 m in front of the beam and a laser was used to pin-point the accuracy of the camera to the middle of the beam.

For the 4-point bending tests, two rollers were placed 1.0 m in from each side of the beam. Therefore, the test configuration was 1.0 m, 0.6 m and 1.0 m, see Figure 6.13. For 3-point bending test, the roller was placed directly in the middle of the beam at 1.3 m, see Figure 6.14. For both of these tests, the rollers were placed on steel plates with dimensions 225x70x25 mm and to distribute and thus, avoiding local damage to the beam.

Both the static tests used the same loading-script. The applied load was done through deformation-controlled loading and started out with the rate of 2 mm/min for the first 20 mm, the rate was then increased to 5 mm/min until the beams either reached failure or the applied force dropped to 50 % of its maximum. Further, the beams had an initial sequence where the load was applied until 5 kN and then unloaded to 1 kN before applying the loading-script.

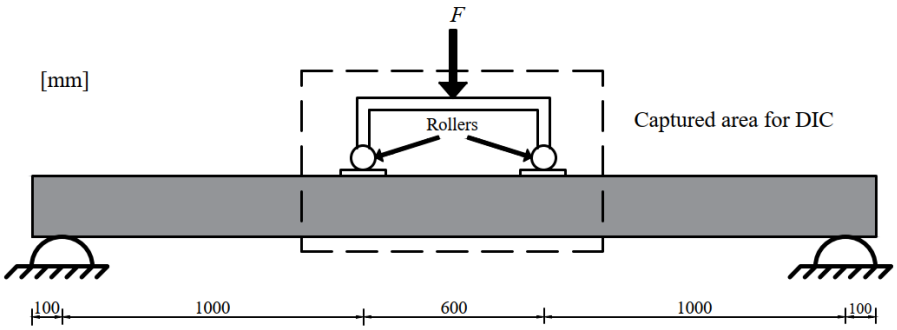

Figure 6.13 The test setup for 4-point bending test.

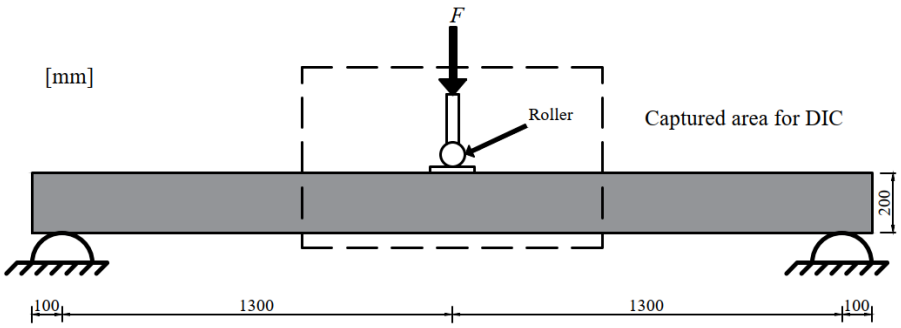

Figure 6.14 The test setup for 3-point bending test.

7 PREDICTED RESPONSE

7.1 Static Response

7.1.1 Orientation

The predictions for the static response include, ultimate limit state, cracking moment and cracking load, load-deflection curves, and plastic rotation. For load-deflection curves both 3-point bending, and 4-point bending is evaluated while results for the plastic rotation capacity is limited to the 3-point bending tests only.

7.1.2 Ultimate Limit State

The load capacity of the reinforced concrete beam is calculated according to the recommendation presented in (Al-Emrani et al., 2013) and calculation presented in (Lozano & Makdesi, 2017), see Appendix M. The ultimate concrete strain is assumed, and the reinforcement is assumed to be yielding for beam with reinforcement diameters of 10 mm and 8 mm. Rupture of tensile reinforcement is assumed for beam with reinforcement diameters of 6 mm. For the compressive zone, the stress-strain relation is assumed to be parabolic. The model used for the reinforced concrete is illustrated in Figure 7.1.

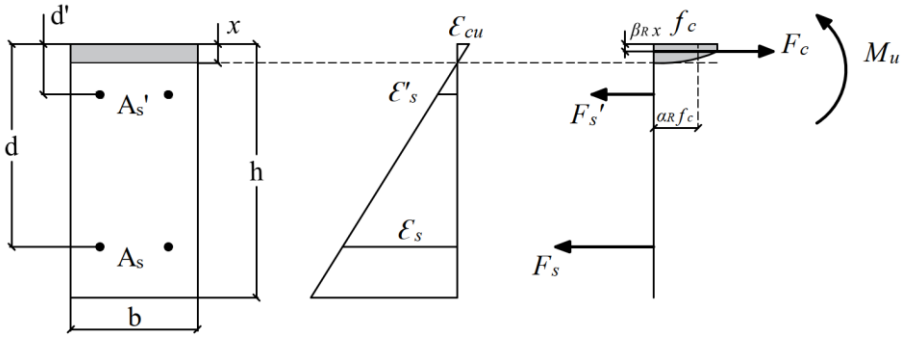

Figure 7.1 Calculation model used for bending moment capacity of concrete section.

The equilibrium conditions for the cross-section can be calculated as in Equation (7.3). From Equation (7.3) the height of the compressive zone was obtained and inserted in Equation (7.4) to calculate the ultimate moment capacity.

Seen in Appendix M it was found that the compressive zone was above the centre of gravity for the top reinforcement which will result in tensile stresses in the top reinforcement. This assumption was considered in an additional calculation to obtain the ultimate moment capacity. To get a more representative response of the ultimate load capacity the self-weight g_1 of the beam is considered in the calculation of ultimate moment capacity and expressed in Equation (7.5).

$$g_1 = g \cdot \rho \cdot A_c \tag{7.1}$$

$$M_g = \frac{g_1 \cdot L^2}{8} \tag{7.2}$$

$$\alpha_R \cdot f_{cm} \cdot b \cdot x = \sigma_s \cdot A_s + \sigma'_s \cdot A'_s \tag{7.3}$$

$$M_u = \alpha_R \cdot f_{cm} \cdot b \cdot x \cdot (d - \beta_R \cdot x) + \sigma'_s \cdot A'_s \cdot (d - d') \tag{7.4}$$

$$M_{u.red} = M_{u.1} - M_g \tag{7.5}$$

where α_R= stress block factor, = 0.81 in ULS
β_R = stress block factor, = 0.416 in ULS
f_{cd} = design compressive strength for concrete
A'_s = area of top steel in cross-section
σ'_s = stress in top steel
A'_s = area of top steel in cross-section
A_s = area of bottom steel in cross-section
σ_s = stress in bottom steel
d' = effective height for the top reinforcement
d = effective height for the bottom reinforcement
x = height of the compressive zone
b = width of the cross-section
ρ = density of reinforced concrete
g = the acceleration of gravity

The steel strain is derived from the strain distribution for top and bottom reinforcement and calculated as

$$\varepsilon_s = \frac{d - x}{x} \cdot \varepsilon_{cu} \tag{7.6}$$

$$\varepsilon'_s = \frac{x - d'}{x} \cdot \varepsilon_{cu} \tag{7.7}$$

where ε_s = steel strain for the bottom reinforcement
ε'_s = steel strain for the top reinforcement
ε_{cu} = ultimate strain for the concrete

The steel stress is derived from the strains in Equations (7.6) and (7.7) by implementing a bilinear relationship to represent the stress-strain relationship. The steel stress can be seen in Equation (7.8).

$$\sigma_s = \begin{cases} E_{sm} \cdot \varepsilon_s & if \quad \varepsilon_s \leq \varepsilon_{sy} \\ f_{ym} + \dfrac{\varepsilon_s - \varepsilon_{sy}}{\varepsilon_{su} - \varepsilon_{sy}} \left(f_{um} - f_{ym}\right) & if \quad \varepsilon_s > \varepsilon_{sy} \end{cases} \tag{7.8}$$

where E_{sm} = The mean modulus of elasticity for steel
f_{ym} = mean steel strength
f_{um} = mean ultimate tensile strength
ε_{sy} = yield steel strain
ε_{su} = ultimate steel strain
ε_s = steel strain

The ultimate load can be derived from the ultimate moment in Equation (7.9) for a simply supported beam in 3-point bending, which is expressed as

$$F_{u.3p} = \frac{4 \cdot M_{u,red}}{L} \tag{7.9}$$

and for a simply supported beam in 4-point bending expressed as

$$F_{u.4p} = \frac{2 \cdot M_{u,red}}{L_F} \tag{7.10}$$

where L and L_F is the distance between the support and load application.

The ultimate load and ultimate moment capacity can be seen in Table 7.1 for the 3-point and 4-point bending case. The table is divided into a case where only bottom reinforcement is considered, and one where both the top and bottom reinforcement is included in the calculations.

Table 7.1 Ultimate moment capacity and ultimate load capacity for reinforcement diameters of 6 mm, 8 mm and 10 mm.

ϕ diamater [mm]	**Considered reinforcement layers**	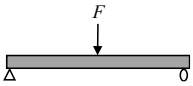		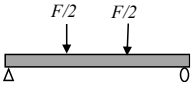	
		$M_{u,red}$ [kNm]	**$F_{u.3p}$ [kN]**	**$M_{u,red}$ [kNm]**	**$F_{u.4p}$ [kN]**
6	Bottom only	5.2	7.9	5.2	10.3
	Top and bottom	5.8	8.9	5.2	11.5
8	Bottom only	9.2	14.2	9.2	18.5
	Top and bottom	10.1	15.6	10.1	20.2
10	Bottom only	13.7	21.1	13.7	27.3
	Top and bottom	14.2	21.9	14.2	28.5

7.1.3 Cracking Moment and Cracking Load

The cracking moment was calculated by using the flexural tensile concrete strength and assuming the moment inertia to be in state I as described in (Al-Emrani et al., 2013). This can be seen in Equation (7.11) .

$$M_{cr} = \frac{f_{ct.fl} \cdot I_I}{h/2} \tag{7.11}$$

$$M_{cr,red} = M_{cr} - M_g \tag{7.12}$$

where $f_{ct.fl}$ = mean flexural tensile strength

I_I = moment of inertia in state I
h = height of the beam

The cracking force is calculated as Equations (7.13) and (7.14) for a simply supported beam in 3-point bending and 4-point bending, respectively. The cracking moment and cracking load are presented in Table 7.2.

$$F_{cr.3p} = \frac{4 \cdot M_{cr,red}}{L} \tag{7.13}$$

$$F_{cr.4p} = \frac{2 \cdot M_{cr,red}}{L_F} \tag{7.14}$$

where L and L_F is the distance between the support and load application.

The yielding moment is calculated similarly to the ultimate moment capacity in Equation (7.4). The steel strain in the bottom reinforcement ε_{sy} in the section when yielding occurs is known, and the concrete strain ε_{cc} is unknown. The stress block factor α_R and β_R are also unknown due to that they are a function of concrete strain ε_{cc}. The strains in Equations (7.15) and (7.16) are calculated by first assuming the position of the neutral axis x_y. Afterwards the stress blockers can be calculated for these strain distributions. The initial assumption of the neutral axis x_y is performed iteratively to obtain a horizontal equilibrium calculated as in Equation (7.17). When the condition for horizontal equilibrium is fulfilled the yielding moment and the yielding loads can be calculated as Equations (7.18), (7.20) and (7.21), respectively. These results are presented in Table 7.2.

$$\varepsilon_{cc.y} = \frac{x_y}{d - x_y} \cdot \varepsilon_{sy} \tag{7.15}$$

$$\varepsilon'_{sy} = \frac{d' - x_y}{d - x_y} \cdot \varepsilon_{sy} \tag{7.16}$$

$$\alpha_R \cdot f_{cm} \cdot b \cdot x_y - f_{ym} \cdot A_s - \sigma'_s \cdot A'_s \approx 0 \tag{7.17}$$

$$M_y = \alpha_R \cdot f_{cm} \cdot b \cdot x_y \cdot \left(d - \beta_R \cdot x_y\right) + \sigma'_s \cdot A'_s \cdot (d - d') \tag{7.18}$$

$$M_{y,red} = M_y - M_g \tag{7.19}$$

$$F_{y.3p} = \frac{4 \cdot M_{y,red}}{L} \tag{7.20}$$

$$F_{y.4p} = \frac{2 \cdot M_{y,red}}{L_F} \tag{7.21}$$

where L and L_F is the distance between the support and load application.

Table 7.2 Summary of cracking moment, yielding moment, cracking load and yielding load for reinforcement diameters of 6 mm, 8 mm and 10 mm.

		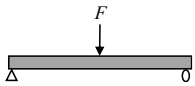		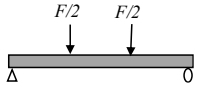	
ϕ *d*iamater [mm]	**State**	**$M_{cr,red}$ or $M_{y,red}$ [kNm]**	**F_{cr} or F_y [kN]**	**$M_{cr,red}$ or $M_{y,red}$ [kNm]**	**F_{cr} or F_y [kN]**
6	Onset of cracking	2.8	4.3	2.8	5.6
	Onset of yielding	4.0	6.1	4.0	7.9
8	Onset of cracking	2.9	4.4	2.9	5.7
	Onset of yielding	8.4	12.9	8.4	16.7
10	Onset of cracking	3.0	4.5	3.0	5.9
	Onset of yielding	12.6	19.4	12.6	25.2

7.1.4 Load-Deflection Curves

To predict the behaviour of the beam subjected to an external load, a load-deflection curve is presented by calculating the stiffness and combining it with the ultimate load from Section 7.1.2. The stiffness is in either state I or state II for concrete in 3-point bending expressed as

$$k_{I.3p} = \frac{48 \cdot E_{cm} \cdot I_I}{L^3} \tag{7.22}$$

$$k_{II.3p} = \frac{48 \cdot E_{cm} \cdot I_{II}}{L^3} \tag{7.23}$$

For 4-point bending it is expressed as

$$k_{I.4p} = \frac{6 \cdot E_{cm} \cdot I_I}{{L_F}^2 \cdot L \cdot (3 - \frac{4 \cdot L_F}{L})} \tag{7.24}$$

$$k_{II.4p} = \frac{6 \cdot E_{cm} \cdot I_{II}}{{L_F}^2 \cdot L \cdot (3 - \frac{4 \cdot L_F}{L})} \tag{7.25}$$

The second moment of inertias is calculated as

$$I_{II} = b \cdot \frac{x_{II}^3}{3} + (\alpha - 1) \cdot A_s' \cdot (x_{II} - d')^2 + \alpha \cdot A_s (d - x_{II})^2 \tag{7.26}$$

and the position of the neutral axis is obtained by solving for x_{II} in Equation (7.27)

$$b \cdot \frac{x_{II}^2}{2} + (\alpha - 1) \cdot A_s' (x_{II} - d') = \alpha \cdot A_s (d - x_{II}) \tag{7.27}$$

Both bi-linear and tri-linear load-deflection curves were used to predict the response. For the case with tri-linear response, the beam is assumed to have stiffness in state I until cracking has occurred, afterwards, it will behave linearly until it reaches the ultimate load where it behaves plastically. For the case with bi-linear response, the beam is assumed to start with the stiffness in state II until it reaches the ultimate load and has a plastic behaviour afterwards. These responses can be seen in Figure 7.2 and the value of stiffness can be seen in Table 7.3.

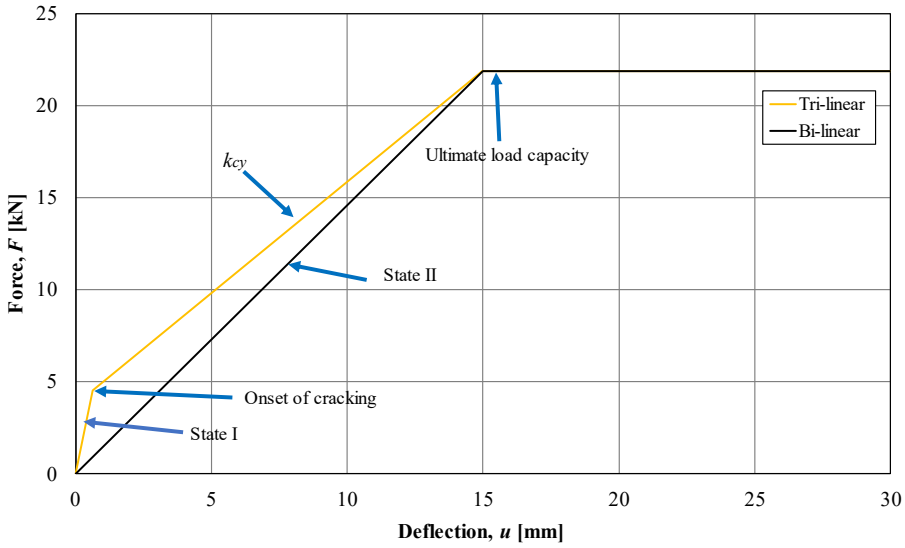

Figure 7.2 *Load-deflection curve for tri-linear and bi-linear response for the beam with reinforcement diameter of 10 mm in 3-point bending test.*

Table 7.3 *Summary of predicted stiffnesses for the load-deflection curves for reinforcement diameters of 6 mm, 8 mm and 10 mm.*

ϕ [mm]	F			F/2 F/2		
	k_I [kN/mm]	k_{II} [kN/mm]	k_{cy} [kN/mm]	k_I [kN/mm]	k_{II} [kN/mm]	k_{cy} [kN/mm]
6	6.9	0.6	0.3	4.0	0.4	0.2
8	7.0	1.0	0.8	4.1	0.6	0.4
10	7.2	1.5	1.2	4.2	0.8	0.7

7.1.5 **Plastic Rotation**

The plastic rotation capacity is obtained by the different methods previously presented in Section 3.7 for simply supported beam with a point load in the midspan. As explained in Section 7.1.2 the top reinforcement is subjected to tension, however, in the calculation of plastic rotation this assumption is neglected in all methods except for the for the case EC2, $\phi 6\ mm$, EC2-detailed, $\phi 6\ mm$ and in the ABC_T-method. The plastic rotations for respective method are presented in Table 7.4 and explained in detail in Appendix M.

Table 7.4 Summary of plastic rotations and plastic deformations for reinforcement diameters of 6 mm, 8 mm and 10 mm.

Method	**Plastic rotation θ_{pl} [mrad]**	**Plastic deformation u_{pl} [mm]**
EC2, $\phi 6\ mm$ [1)]	8.1	10.5
EC2, $\phi 8\ mm$	27.1	35.2
EC2, $\phi 10\ mm$	24.6	32.0
EC2-detailed, $\phi 6\ mm$	2.8	3.6
EC2-detailed, $\phi 8\ mm$	28.4	36.9
EC2-detailed, $\phi 10\ mm$	30.8	40.0
MSB, $\phi 6\ mm$	16.0	21.0
MSB, $\phi 8\ mm$	54.2	70.5
MSB, $\phi 10\ mm$	49.3	64.1
ABC, $\phi 6\ mm$	28.9	37.6
ABC, $\phi 8\ mm$	44.7	58.2
ABC, $\phi 10\ mm$	38.7	50.3
ABC_T, $\phi 6\ mm$ [2)]	52.0	67.0
ABC_T, $\phi 8\ mm$ [2)]	51.2	66.6
ABC_T, $\phi 10\ mm$ [2)]	48.5	63.0
BK25, $\phi 6\ mm$	15.9	20.7
BK25, $\phi 8\ mm$	54.7	71.1
BK25, $\phi 10\ mm$	36.2	47.1

[1)] *EC2, $\phi 6$ mm is calculation based on reinforcement class B.*

[2)] *ABC_T is the case including top reinforcement.*

7.2 Dynamic Response

7.2.1 2DOF Prediction

In this subchapter the prediction for the dynamic response is presented. The 2DOF prediction was made to be able to get a rough estimate of behaviour for the deflection over time relations, these were then compared to the dynamic test results.

The 2DOF-model is being used to describe the dynamic response of the beam subjected to drop-weight impact. 2DOF calculation are based on an excel-script from Johansson (using the central difference method) which was adjusted to this thesis. The result of the deflection over time for the first drop-weight impact are presented in Figure 7.3. It can be observed that increased reinforcement diameters amount resulted in decreased maximum deflection for all cases.

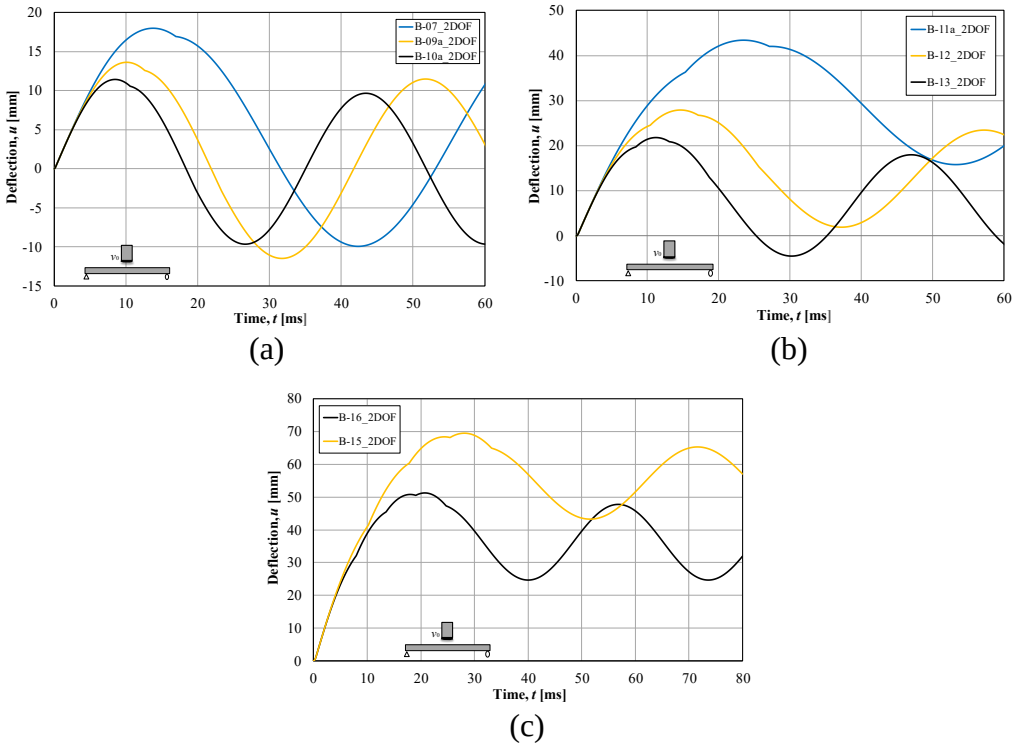

Figure 7.3 Predicted midpoint deflection over time with drop weight impact of: (a) 10 kg, (b) 20 kg and (c) 40 kg.

In Table 7.5 the maximum, elastic deflection, plastic deflection, and the resistance force are presented for the first drop-weight impact. The total plastic deformations for repeated impacts are also presented. The prediction for repeated impact is based on a theory from Jönsson & Stenseke (2018) where the plastic deformation for first impact is multiplied with a constant k according to Equation (7.28) to obtain the total plastic deformation for each impact.

Table 7.5 Summary of the 2DOF results after first impact.

Series	Beam	m [kg]	Impacts [-]	$R_{m,2,mod}$ [kN]	u_{max} [mm]	u_{el} [mm]	u_{pl} [mm]	$u_{pl,tot}$ [mm]
I10	B-07	10	5	8.9	17.9	14.8	3.2	19.5
	B-08	10	4	8.9	17.9	14.8	3.2	14.8
	B-09a	10	6	14.3	13.8	15.2	0	0
	B-09b	10	6	14.3	13.8	15.2	0	0
	B-10a	10	5	15.6	11.3	15.1	0	0
	B-10b	10	4	15.6	11.3	15.1	0	0
I20	B-11a	20	1	8.9	42.9	14.8	28.5	28.5
	B-12	20	2	14.3	27.9	15.2	12.7	26.7
	B-13	20	2	15.6	21.8	15.1	6.7	14.2
I40	B-15	40	1	14.3	69.5	15.2	54.3	54.3
	B-16	40	1	15.6	51.3	15.1	36.2	36.2

$$k = 1.1^{(n-1)} \tag{7.28}$$

where n is the number of impacts obtained.

8 EXPERIMENTAL RESULTS

8.1 Orientation

The results from material tests, dynamic tests and static tests are treated in this chapter. For the material tests, both concrete and steel reinforcement was tested, the values from the material tests were later used in the predictions. The dynamics tests contain an evaluation over the relative midpoint deflection, followed by the effect of different drop-weights, effect of reinforcement diameter, and lastly strain fields. The statical tests contains a summary of the load capacity, plastic rotation capacity, residual capacity of damaged beams and the internal work for the beams.

8.2 Concrete Properties

The values for concrete properties were obtained according to methods explained in Section 2.1. The experiments of dynamic and static test occurred at 57 days and therefore the concrete properties were tested on that day. Three concrete cubes remained and were tested a week after the initial test during drop-weight testing. The wedge splitting test was performed at 57 days. The results for these tests can be seen in Table 8.1.

Table 8.1 Average concrete properties for specimens tested at 28 days, 57 days, and 64 days. Values of f_{ctm} and E_{cm} are based on the compression strength of the concrete f_{cm}.

Age [days]	Mean compressive strength f_{cm} [MPa]	Mean tensile strength f_{ctm} [MPa]	Modulus of Elasticity E_{cm} [GPa]	Fracture energy G_F [Nm/m^2]
28	55.3	3.9	36.8	-
57	58.3	4.1	37.3	150
64	58.7	4.1	37.4	-

8.3 Steel Properties

The values for steel properties were obtained according to Section 2.2 and the average result can be seen in Table 8.2. For the steel reinforcement of 6 mm, the proof stress $f_{0.2}$ was used instead of yielding stress f_y which was used for 8 mm and 10 mm.

Table 8.2 Average steel properties for reinforcement of different diameters.

Specimen	ε_{su} [‰]	$f_{0.2}$ or f_y [%]	f_u [MPa]	f_u/f_y [-]	E_s [GPa]
Ø6 mm	29	546	588	1.08	200
Ø8 mm	98	588	688	1.17	206
Ø10 mm	116	569	699	1.23	203

8.4 Dynamic Testing

8.4.1 Orientation

In this subchapter the dynamic testing is presented from the data captured with high-speed cameras during impact loading on the beams. This data was processed in GOM Correlate (GOM, 2019) software to calculate the relative midpoint deflection over time both for single and repeated impact loading. The cracks after impact loading are evaluated with strain fields from the software, both for single and repeated loading.

8.4.2 Relative Midpoint Deflection over Time

8.4.2.1 Orientation

To calculate the relative midpoint deflection over time, different result points were defined on the concrete surface in GOM Correlate 2019 software (GOM, 2019), see Figure 8.1 for schematic illustration. One result point was aimed to be placed in the midspan of the beam for respective impact, however, due to local damages that occurred after repeated impact loading this midpoint was sometimes placed a small distance from the middle and a reference point was allocated a couple decimetres to the right of the midpoint. The reference point was used to scale the midpoint deflection if the result of the midpoint (due to concrete spalling) could not be captured during testing. Two points at the support was placed to calculate the average deflection $u_{support}$ at the support. Due to the dynamic response of the beam subjected to impact loading, the beam was not always in contact with the support. Therefore, the relative midpoint deflection is used here to describe the global response of the beam. The relative midpoint deflection was calculated by taking the difference between midpoint and average support deflection seen in Equation (8.1).

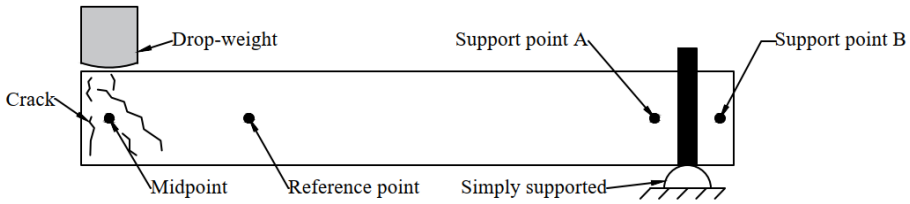

Figure 8.1 Schematic illustration of positioning of result points on concrete surface in beam subjected to impact loading.

$$u_{relative} = u_{mid} - u_{support} \tag{8.1}$$

In Figure 8.2 the midpoint, relative midpoint and average support displacement are shown for the case of beam B-07 plotted against time to illustrate the shift in deflection that occurs between 5 ms and 10 ms. A similar shift occurs for all beams tested, but the exact time of occurrence varies depending on drop-weight mass and reinforcement configuration used in the beams. After the drop-weight impacts the beam, the beam part at the support first lifts upwards before it is pressed down and again gets in contact with the support. The relative midpoint rebounds after around 17 ms and result as a global upwards movement in the beam. This leads to that the beam at the support lifts again around 27 ms. This rebound response occurs for all beams during impact loading.

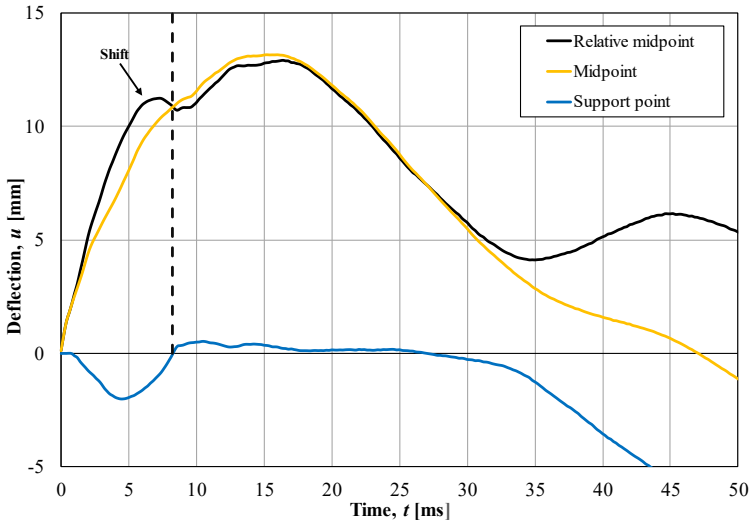

Figure 8.2 *A plot showcasing the shift during impact in correlation to midpoint and support point for beam B-07.*

Figure 8.3 illustrates the relative midpoint together with the scaled midpoint over time for repeated impact loading. Due to local spalling, the midpoint was not always captured or was influenced by heavy noise in the GOM Correlate 2019 (GOM, 2019) software. To complement the missing midpoint data, a reference point was defined to get an approximate description of the midpoint deflection. This was achieved with two different approaches: one where the average ratio was calculated between the relative midpoint and the reference point to scale the missing midpoint for repeated impact. The other method was used when the initial part of the midpoint was captured followed by a lot of noise. Then the average ratio was calculated between the initial stage and maximum deflection instead, see Figure 8.3. The scaled midpoint deflection is displayed as dotted lines in the graph and denoted with the letter "*S*" after the beam name. The figure also exhibits an oscillating phenomenon, where the local amplitude of the oscillation is an indication of the remaining plastic deflection after impact.

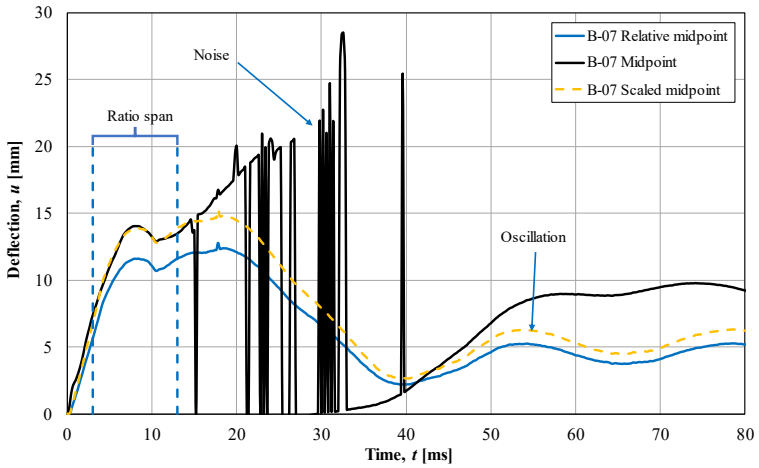

Figure 8.3 *An image describing the scaled midpoint in comparison with relative midpoint.*

8.4.2.2 Summary of Total and Plastic Deflections

In this subsection the maximum deflection u_{max}, total maximum deflection $u_{max,tot}$, the additional plastic deflection Δu_{pl} and total plastic deflection $u_{pl,tot}$ are presented for all beams subjected to repeated impact, see Table 8.3. In the following sections a comparison between the beams is presented with regard of varied reinforcement ratio, drop-weight mass, and number of impacts.

Table 8.3 A summarization of the maximum deflection, maximum total plastic deflection, additional plastic deflection and total plastic deflection.

Beam	Drop	$u_{\max}$ [mm]	Δu_{pl} [mm]	$u_{pl,tot}$ [mm]	$u_{max,tot}$ [mm]
B-07	1	12.9	6.2	6.2	12.9
	2	15.3	5.5	11.7	21.5
	3	16.1	4.7	16.4	27.8
	4	19.5	6.7	23.1	35.9
	5	27.6	14.0	37.1	50.7
B-08	1	13.1	6.3	6.3	13.1
	2	14.4	4.9	11.2	20.7
	3	15.3	4.7	15.8	26.5
	4	17.9	5.8	21.6	33.8
B-09a	1	9.8	2.0	2.0	9.8
	2	10.4	-0.2	1.9	12.4
	3	11.0	0.4	2.3	12.8
	4	11.6	1.3	3.6	13.9
B-09b	1	9.5	3.1	3.1	9.5
	2	10.0	0.5	3.6	13.2
	3	-	0.3	3.9	-
	4	12.9	-1.1	2.8	16.8
	5	11.6	13.1	15.9	14.4
	6	20.5	6.1	22.0	36.4
B-10a	1	8.3	1.7	1.7	8.3
	2	8.7	0.0	1.7	10.4
	3	9.3	1.1	2.8	10.9
	4	11.3	-0.6	2.1	14.0
	5	12.6	1.1	3.2	14.7
B-10b	1	8.3	3.0	3.0	8.3
	2	9.0	0.3	3.3	12.0
	3	-	1.2	4.5	-
	4	12.7	0.2	4.7	17.2
B-11a	1	196.8	-	-	196.8
B-11b	1	94.6	-	68.3	94.6
B-12	1	22.6	6.7	6.7	22.6
	2	29.0	7.5	14.2	35.7
B-13	1	17.8	2.8	2.8	17.8
	2	23.5	2.2	5.0	26.3
B-15	1	76.0	55.2	55.2	76.0
B-16	2	49.4	25.5	25.5	49.4

8.4.2.3 **Effect of Reinforcement Diameter**

In this subsection the effect of reinforcement diameter is evaluated for the first impact of each beam.

The relative midpoint deflections over time are presented in Figure 8.4 for beams subjected to a drop-weight of 10 kg. The plastic deflection and maximal deflection are presented in Table 8.3.

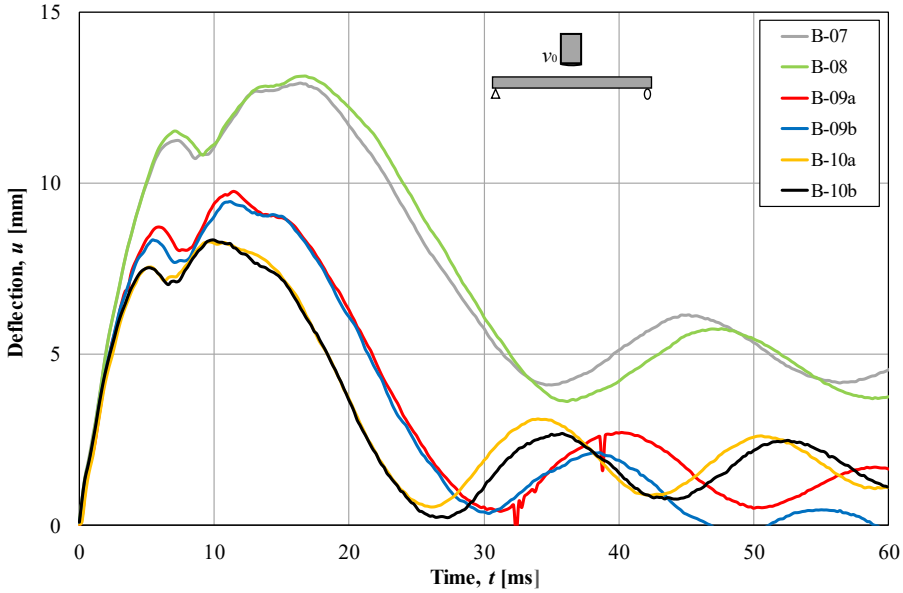

Figure 8.4 *Illustrates the relative midpoint deflect over time for beams subjected to a drop-weight of 10kg.*

The magnitude of the deflections varies for the beams with different reinforcement diameters, see Figure 8.4. As expected, increased reinforcement diameters amount resulted in decreased maximum deflection. However, the dynamic behaviour of the beams was similar, the deflections reach its maximum deflection rapidly and then oscillate with a slower rate afterwards. The beams with 8 mm and 10 mm reinforcement bars oscillates around a similar, very small deflections, thus indicating that the plastic deflection in these cases were close to negligible.

The relative midpoint deflections over time for beams subjected to drop-weight of 20 kg are presented in Figure 8.5. The plastic deflection and maximal deflection are presented in Table 8.3.

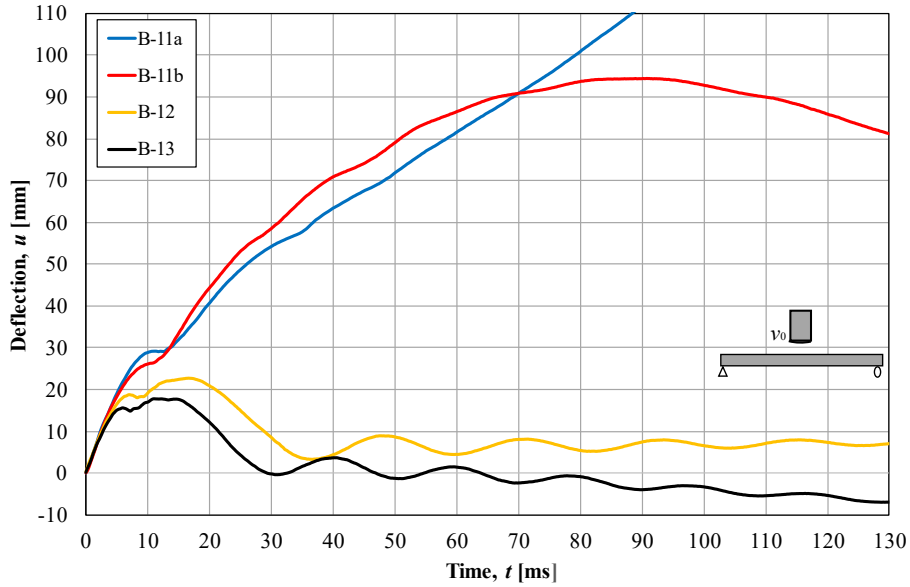

Figure 8.5 *Illustrates the relative midpoint deflect over time for beams subjected to a drop-weight of 20 kg.*

The effect of reinforcement is noticeable in series-I20 where the beam with reinforcement diameters of 10 mm display lower deflection over times compared to beams with reinforcement diameters of 8 mm and 6 mm. The beams B-12 and B-13 shows a similar behaviour in deflection over time compared to beams in series-I10. The deflection increases rapidly and then oscillate around the final plastic deflection after it reaches it maximum deflections. Beams B-11a and B-11b shows a different response in deflection over time, where the deflection for beam B-11a obtained larger final midpoint deflection due to final failure; the beam broke into two parts with both bottom and top reinforcement torn off. For beam B-11b, a large midpoint deflection was obtained as well but here final failure was not reached; the bottom reinforcement was torn off but some of the residual capacity remained thanks to intact top reinforcement. This is the result of using a rubber sheet placed above the contact surface of the drop-weight and beam B-11b. The impulse that beam B-11b experience was thereby somewhat more prolonged in time, which in this case resulted in less drastic response compared to beam B-11a. It shall also be noted that the impulses for beams B-11a and B-11b is assumed to be the same.

The relative midpoint deflections over time are presented for beams subjected to drop-weight of 40 kg in Figure 8.6. The plastic deflection and maximal deflection are shown in Table 8.3.

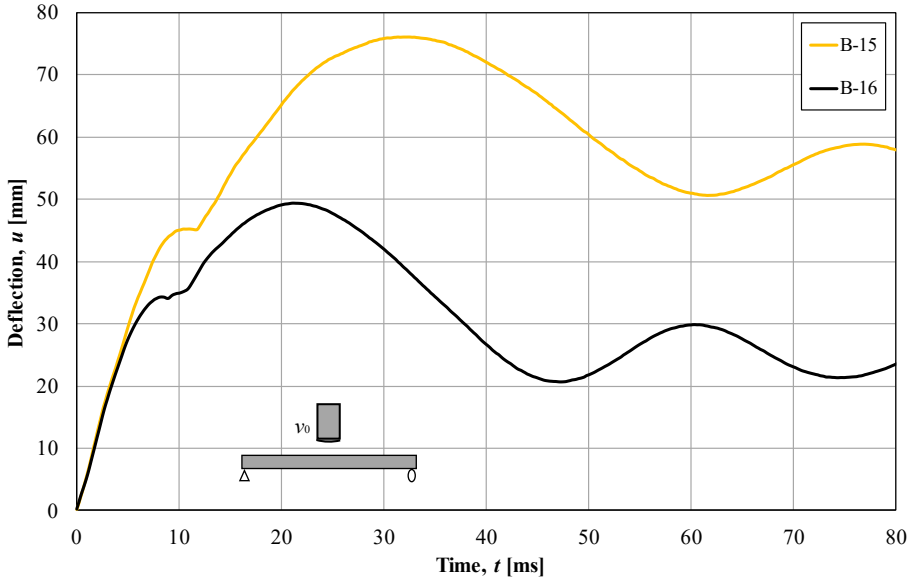

Figure 8.6 *Illustrates the relative midpoint deflect over time for beams subjected to a drop-weight of 40kg.*

Figure 8.6 illustrates a similar behaviour for the deflections as in series-I10 and series-I20 where beams with larger reinforcement result in a smaller deflection over time. The deflection over time increases rapidly and then oscillate after it reaches it maximum deflection. However, the oscillation occurs at a higher deflection compared to series-I10 and series-I20.

8.4.2.4 Effect of Drop-Weight

The result presented in this section are beams with the same reinforcement diameters subjected to drop-weights of 10 kg, 20 kg, and 40 kg after first impact.

The relative midpoint deflections over time are presented for beams with reinforcement diameters of 6 mm in Figure 8.7. The plastic deflection and maximal deflection are presented in Table 8.3.

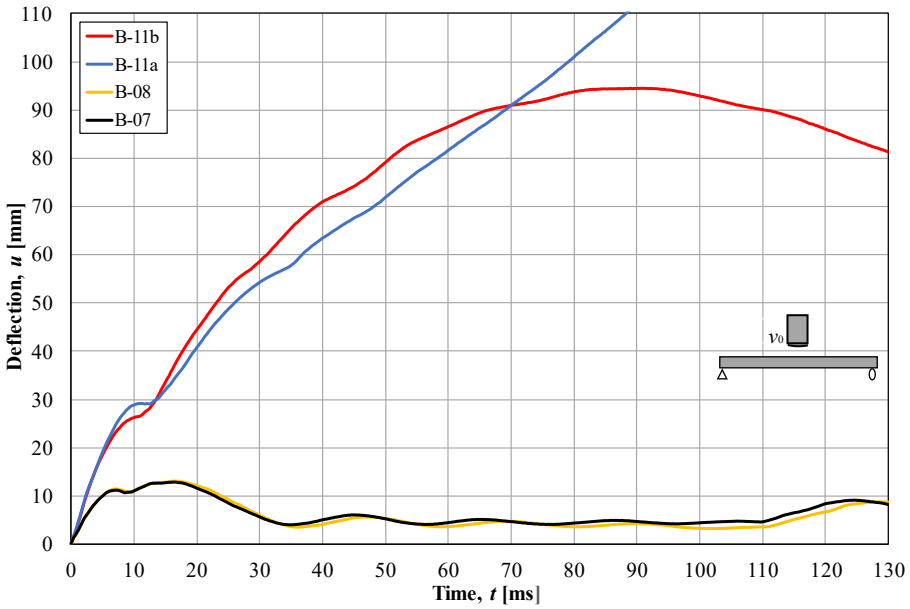

Figure 8.7 *Illustrates the relative midpoint deflect over time for beams subjected to a drop-weight of 10 kg, and 20 kg for reinforcement diameter of 6 mm.*

The result illustrates that the beams subjected to a drop-weight of 10 kg results in smaller deflections over time compared to the beams subjected to 20 kg. The behaviour of beams B-11a and B-11b is previously explained in Section 8.4.2.3.

The relative midpoint deflections over time are presented for beams with reinforcement diameters of 8 mm in Figure 8.8.

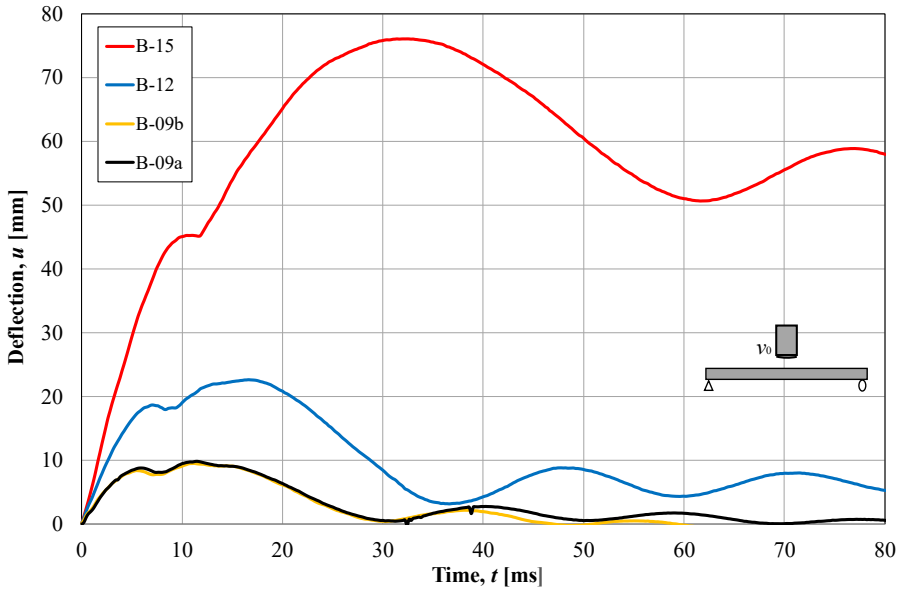

Figure 8.8 *Illustrates the relative midpoint deflect over time for beams subjected to a drop-weight of 10 kg, 20 kg, and 40 kg for reinforcement diameter of 8 mm.*

The result illustrates that an increase in drop-weight mass result in an increase in deflection over time. However, the increase in deflection over time is not in direct proportion to the increase in drop-weight mass. It can be observed that the deflection increases with a higher rate in the initial stage for beams subjected to a heavier drop-weight. It is also noticeable that the oscillating part for beam B-15 occurs at a higher deflection compared to the beams subject to a lower drop-weight mass.

The relative midpoint deflections over time are presented for beams with reinforcement diameters of 10 mm in Figure 8.9.

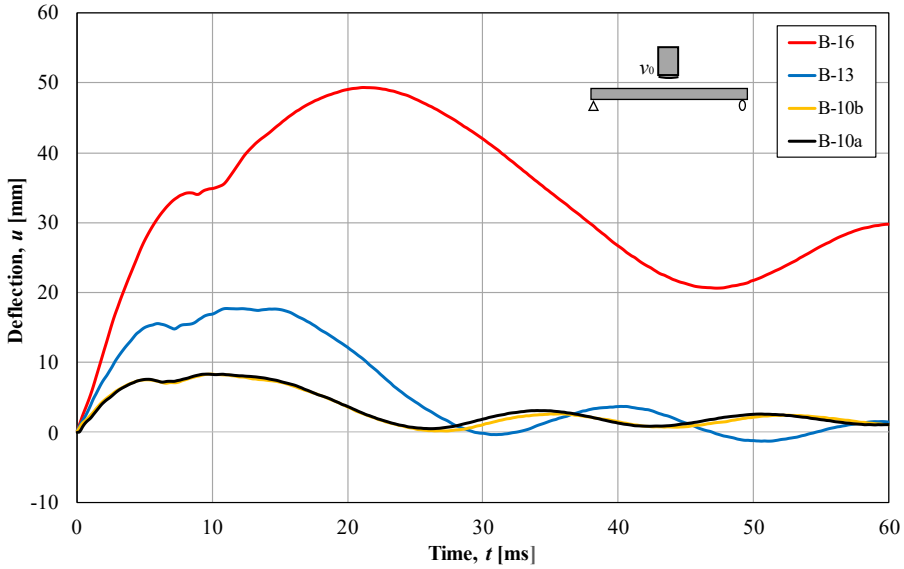

Figure 8.9 *Illustrates the midpoint deflect over time for beams subjected to a drop-weight of 10 kg, 20 kg, and 40 kg for reinforcement diameter of 10 mm.*

Similarly, the result illustrates that increase in drop-weight mass result in increased deflection over time. It can be observed that the deflection increases with a higher rate in the initial stage for beams subjected to a heavier drop-weight. It is also noticeable that the oscillating part for beam B-16 occurs at a higher deflection compared to beams subjected to a lower drop-weight mass.

8.4.2.5 Midpoint Deflection over Time during Repeated Impacts

In this section the result for beams subjected to repeated impacts are presented.

The relative midpoint deflection over time for beams in series-I10 are presented for each impact, see Figure 8.10 to Figure 8.12. The results are summarized in Table 8.3.

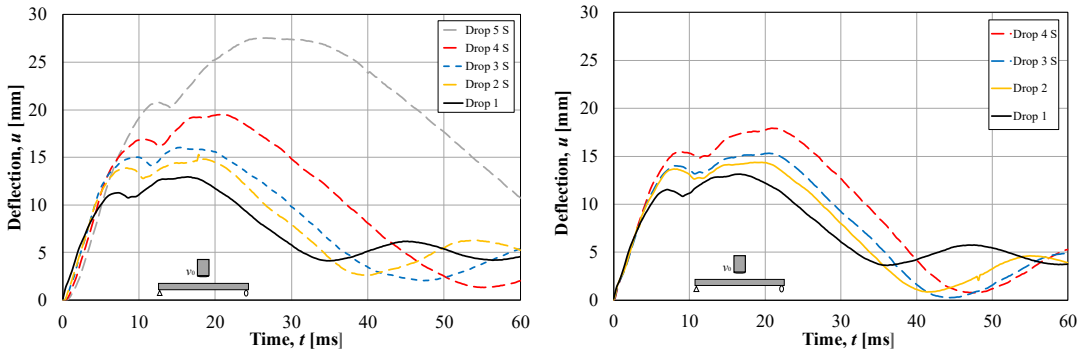

(a) B-07 (b) B-08

Figure 8.10 Illustrates the relative deflection over time for beams B-07 and B-08 during repeated impact loading.

As can be seen in Figure 8.10 the deflection over time increases for each additional impact. The behaviour of the deflections is similar between the drops, where the deflections increase rapidly until it reaches its maximum deflection. However, for beam B-07 there is a large increase in deflection between drop 5 compared to the previous drops. The reason for this difference is that at drop 5, the beam experienced severe local damages on the compressive zone.

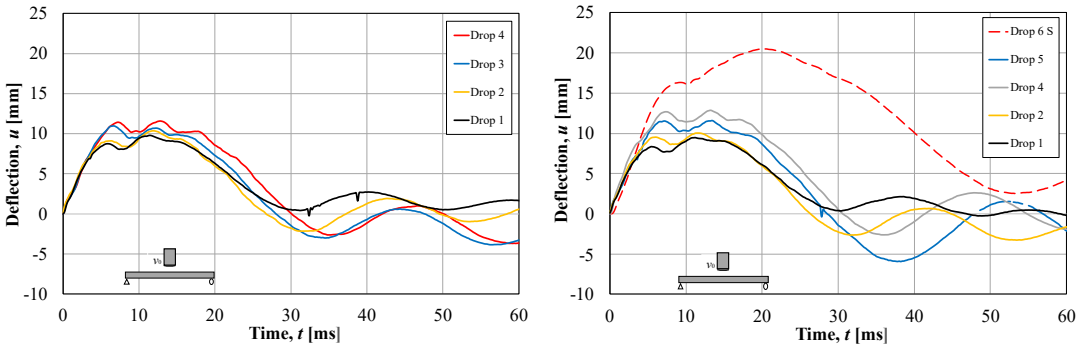

(a) B-09a (b) B-09b

Figure 8.11 Illustrates the relative deflection over time for beams B-09a and B-09b during repeated impact loading.

As illustrated in Figure 8.11 the deflections increase for each additional impact. For beam B-09b there is a larger increase in deflection at drop 6 in comparison to the previous drops. The reason for this difference is that the beam experienced severe local damages on the compressive zone. It is to be noted that drop 5 for beam B-09b resulted in lower deflection over time compared to drop 4. The reason for this has not been investigated in detail.

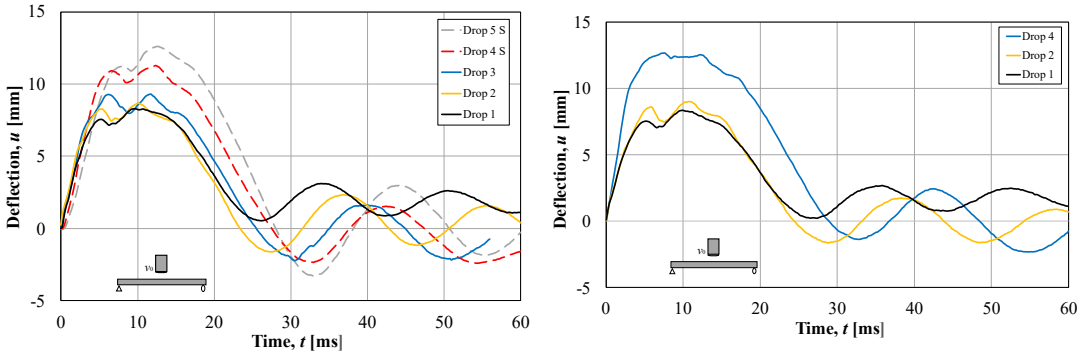

(a) B-10a (b) B-10b

Figure 8.12 Illustrates the relative deflection over time for beams B-10a and B-10b during repeated impact loading.

As illustrated in Figure 8.12 the deflection increases for each drop and the deflections increases rapidly until it reaches it maximum. It is to be noted that the result for drop 3 of beam B-10b was not captured. It can be observed that the increase in deflection between each drop is lower compared to beams B-09b, B-09a, B08 and B-07.

The relative deflection over time is presented for the beams in series-I20 for each impact in Figure 8.13 and summarized in Table 8.3.

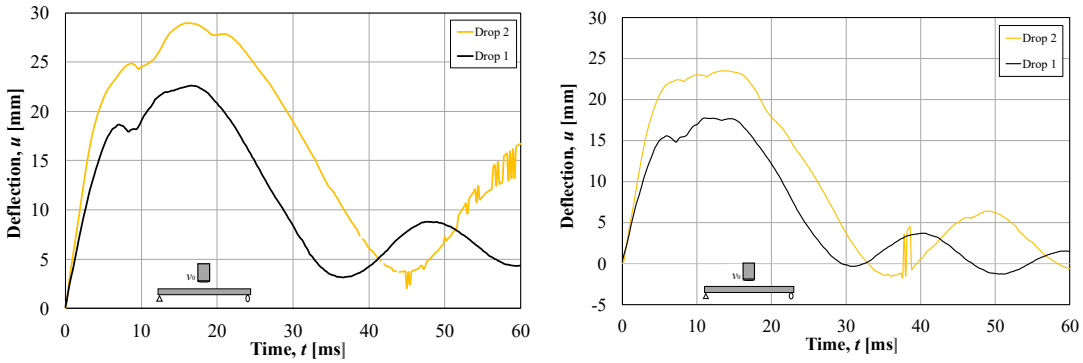

(a) B-12 (b) B-13

Figure 8.13 Showcasing the relative deflection over time for beams B-12 and B-13 during repeated impact loading.

As can be seen in Figure 8.13 the relative deflection over time increases for each drop and the deflection increases rapidly until it reaches it maximum. It can be observed that the increase in deflection between the drop is larger compared to beams in series-I10.

8.4.3 Effect on Plastic Deflection at Repeated Loading

The result for additional plastic deflection and total plastic deflection for beams in series-I10 are presented in Figure 8.14 and summarized in Table 8.3.

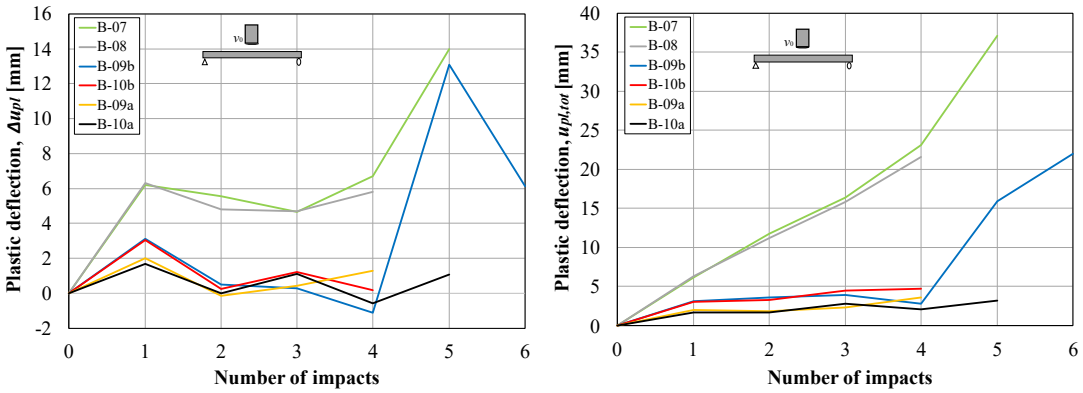

(a) Additional plastic deflection (b) Total plastic deflection

Figure 8.14 *(a) An illustration of the additional plastic deflection after each impact. (b) An illustration of the total plastic deflection after each impact.*

The response of the additional plastic deflection differs between the beams, see Figure 8.14a. The beams with reinforcement diameters of 6 mm result in higher additional plastic deflection compared to beams with reinforcement diameters of 8 mm and 10 mm. It can be observed that the additional plastic deflection is generally larger for the first impact compared to the second and third impact. The beams show a relatively constant response between second and fourth impact for beams with reinforcement diameters of 8 mm and 10 mm. Beams B-07 and B-08 has a similar response between the first impact and fourth impact. Another interesting observation is that beams B-09b and B-10a illustrate a negative plastic deflection after the fourth impact. The reason for this response has not been investigated in detail; however, one theory behind this response can be explained by experiment procedure. The beams had to be adjusted after each drop-weight impact and a hydraulic lifter was placed under the middle of the beam to place the beams into the right position. This procedure might have changed the beams original position in height and resulted as lower additional plastic deflection after repeated impact. It can be observed for beam B-09 after the fourth impact that the relative midpoint deflection oscillates around a lower plastic deflection compared to the first impact, see Figure 8.15. This supports the proposed theory about the unexpected response of the plastic deflection at repeated impact.

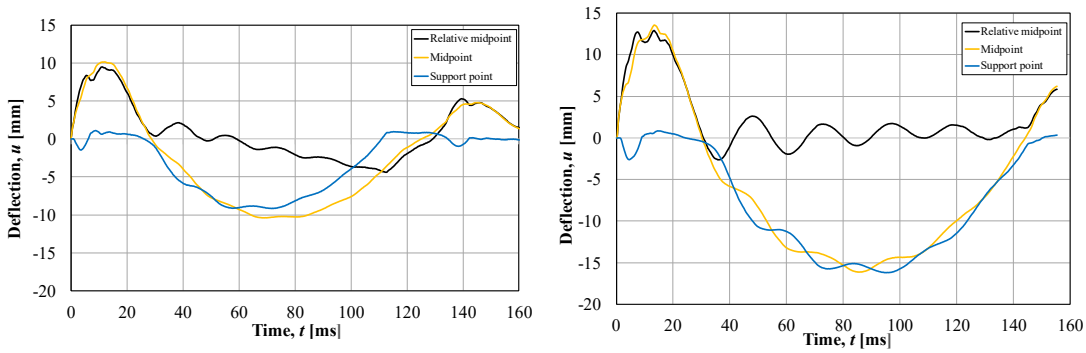

(a) (b)

Figure 8.15 *a) An illustration of the additional plastic deflection for beam B-09b after first impact. b) An illustration of the additional plastic deflection for beam B-09b after fourth impact.*

8.4.1 Strain Fields

8.4.1.1 Introduction

To evaluate the crack pattern from the impact loading, GOM Correlate (GOM, 2019) was used to assess the strain field on the surface of the beams. To get a representative behaviour of the cracks only major strains are evaluated in the analysis. The upper limit of strains was set to 2 % and the lower limit were set to 1.2 % to remove as much noise as possible in the analysis.

8.4.1.2 Effect of Reinforcement Diameter

The initial strain fields for some beams in series-I10 due to the first impact are presented in Figure 8.16. Flexural cracks appear under the impact area after 0.4 ms for all beams: in addition, beam B-10a also displays a horizontal crack. Bending cracks on the upper region of the beams are noticeable after 0.8 ms for all beams and closes after 3.0 ms. Bending cracks around the bottom region develops after 1.6 ms and more develops after 5.0 ms. It can be observed that strain fields in beam B-07 are more visible compared to the other beams.

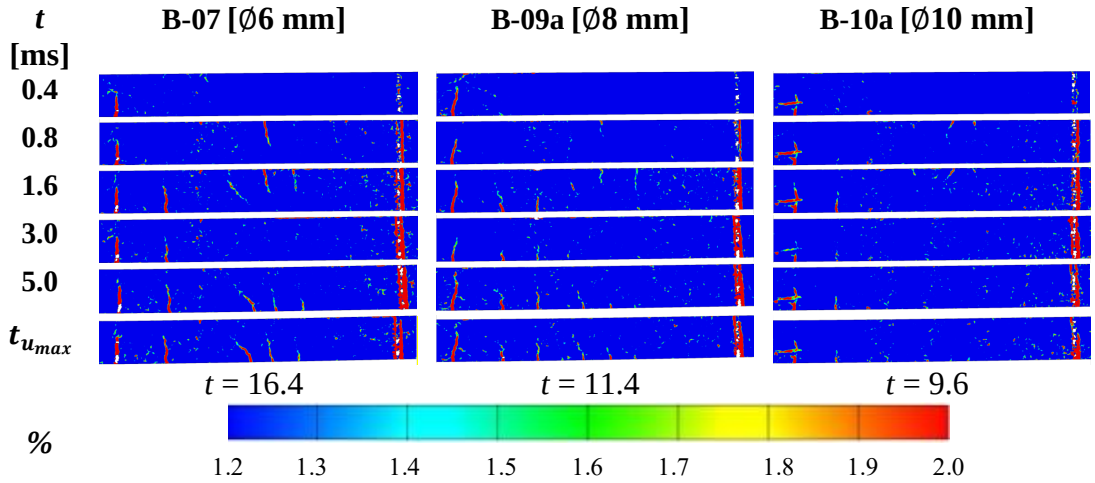

Figure 8.16 *The strain fields for different time intervals for beams of reinforcement diameter 6 mm, 8 mm, and 10 mm.*

8.4.1.3 Effect of Drop-Weight Mass

The strain fields for beams with a reinforcement diameter of 8 mm after first impact, see Figure 8.17. The beams are subjected to a drop-weight of 10 kg, 20 kg, and 40 kg.

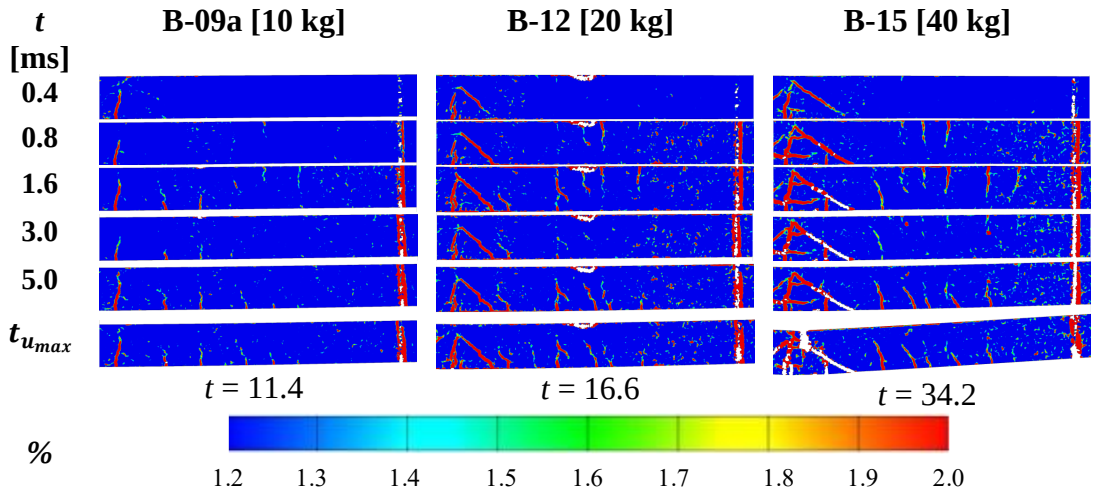

Figure 8.17 *The strain fields for beams with a reinforcement diameter of 8 mm, subjected to a drop-weight of 10 kg, 20 kg, and 40 kg.*

Flexural cracks and shear cracks are displayed under the impact area after 0.4 ms for beams B-12 and B-15. However, in beam B-09a only flexural crack developed. Two horizontal cracks are noticeable for beam B-15 beneath the impact zone. Bending cracks on the upper region of the beams are displayed after 0.8 ms for beams B-12 and B-15. Beam B-09a develops bending cracks on the upper and lower region of the beam after 1.6 ms. The bending cracks on the upper region closes for all beams after 3.0 ms. It can be observed that beams subjected to heavier drop-weight mass result in earlier development of cracks in the upper and lower region of the beams.

8.4.1.4 Effect of Repeated Impacts

The strain field for beams subjected to repeated impacts are presented in this section. The plastic deflection for each drop is presented, seen in Figure 8.18.

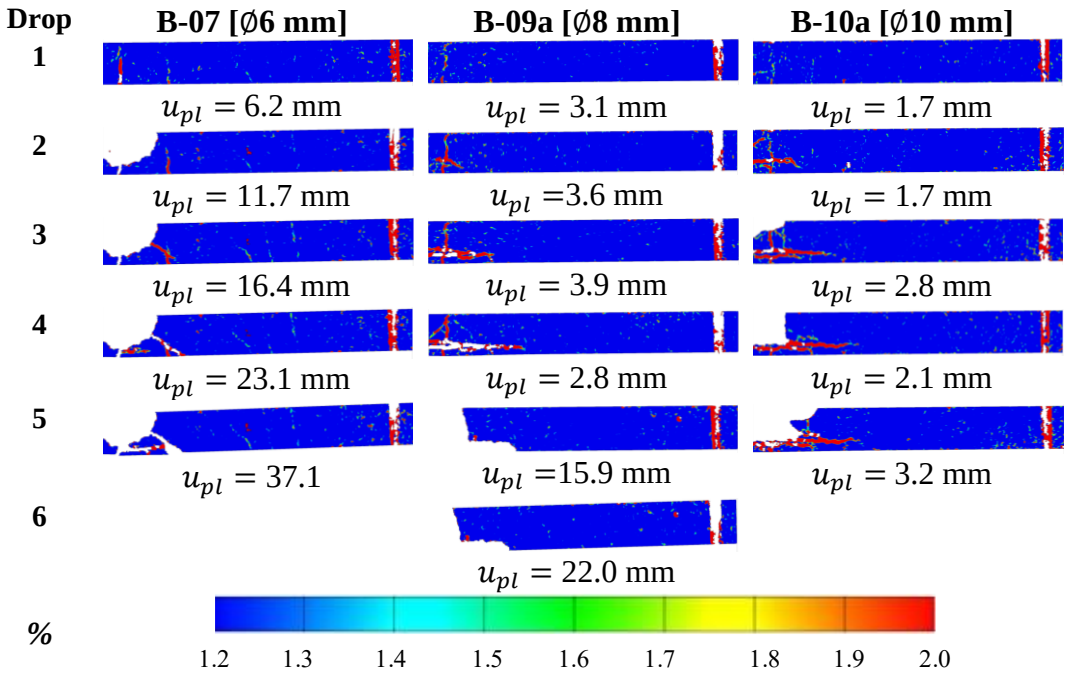

Figure 8.18 *The strain fields of plastic deflection for beams with reinforcement diameter of 6 mm, 8 mm, and 10 mm subjected to a repeated drop-weight impact of 10 kg.*

All beams developed a flexural crack under the impact area after the first impact. Beam B-07 develop white regions on top of the beam which can be seen after the second drop due to local crushing and spalling of concrete. Flexural cracks, shear crack, and horizontal cracks can be seen after the second drop for beams B-09a and B-10a. After the third drop beam B-07 develops a shear crack under impact area, however, beams B-09a and B-10a develops a distinct horizontal crack. B-10a displays white regions after the third drop where part of the compressive zone has been removed. Similarly, B-09a develops white regions on top and bottom of the beam after the fifth drop, due to damages in the compressive zone and spalling of concrete.

8.5 Static Testing

8.5.1 Orientation

The load-deflection relationship for both damaged and undamaged beams, as well as plastic rotation, and internal work are presented within this subsection. For the load-deflection relationship the beams were loaded until it reached 50 % of its ultimate load capacity. The static test on the undamaged beams were made for 3+3 beams, tested in 3- and 4-point bending, respectively, see Section 6.1. The static tests were used to evaluate the ultimate load capacity and, plastic deformation capacity for the undamaged beams and the residual capacity for the beams previously subjected to impact loading. Some of the dynamically tested beams were not tested statically since the amount of damage obtained by the impact loading was severe and the remaining residual capacity was deemed to be too low to be of interest. To evaluate the damaged beams a 3-point bending test would be ideal since these beams were subjected to a drop-weight in the midspan. However, since the damaged beams suffered major local crushing of concrete to the compressive zone, all these beams were tested in a 4-point

bending test. Therefore, two different static test setups for the reference beams were used to make a fair assessment of the static result.

8.5.2 Undamaged Beams

Load-deflection relationship are presented for the reference beams in Figure 8.19 and Figure 8.20 for 3- and 4-point bending, respectively. The results for the load-deflection curves are summarized in Table 8.4. It is to be noted that the deflection u_F displayed in Figure 8.19 and Figure 8.20 is the deflection under the point load and not the midpoint deflection on the beams.

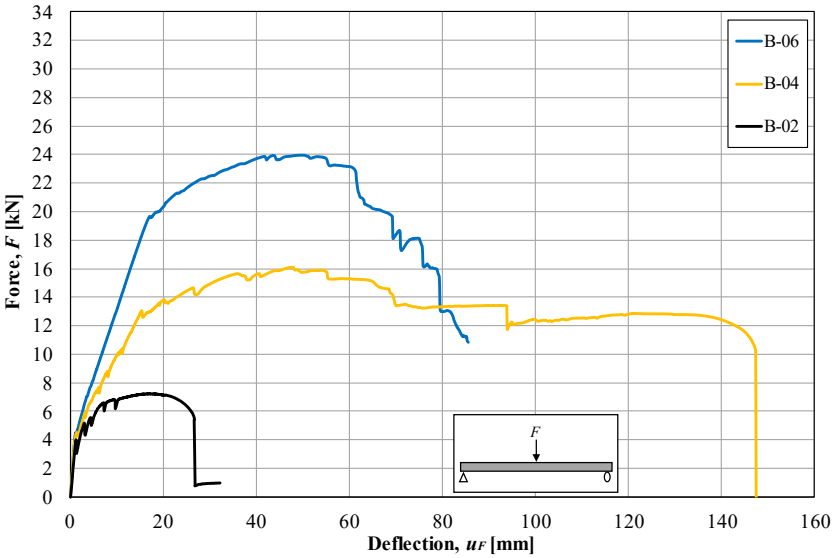

Figure 8.19 An illustration of the load-deflection curve subjected to a 3-point bending tests for reference beams with a diameter of 6 mm, 8 mm, and 10 mm.

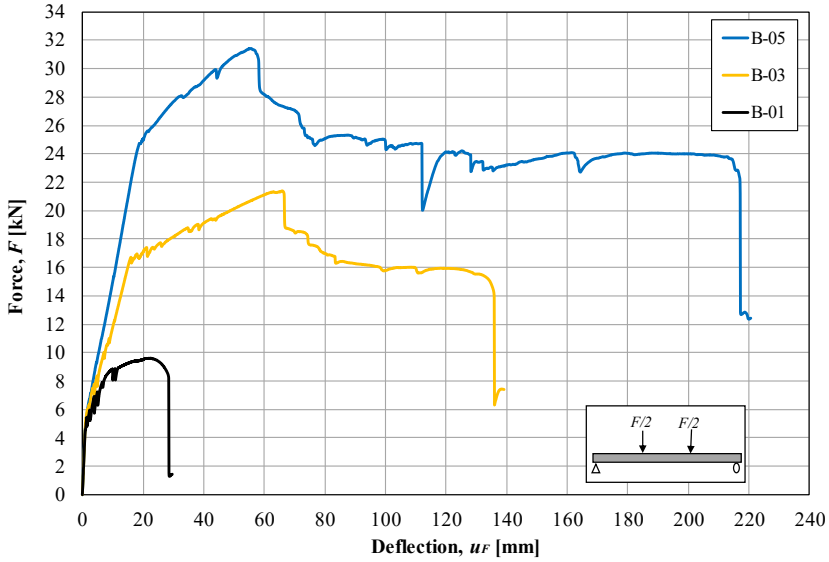

Figure 8.20 An illustration of the load-deflection curve subjected to a 4-point bending tests for reference beams with a diameter of 6 mm, 8 mm, and 10 mm.

As illustrated in Figure 8.19, the behaviour of the beams differs from each other in 3-point bending test. It can be observed that the ultimate load capacity increases for beams with larger reinforcement diameter. All three beams behave similarly in state I and the stiffness for the beams change when state II is reached. The beam with larger reinforcement shows a larger stiffness both in state II and state III. Beam B-02 reaches its maximum load capacity for a lower load in comparison to beams B-04 and B-06 and has sudden drop afterwards. The sudden drop in load capacity for B-02 was due to rupture of the bottom tensile reinforcement. Beam B-04 shows larger ultimate load capacity and obtained a more ductile response compared to B-02. Beam B-04 shows a sudden drop at $u \approx 90$ mm, which was due to crushing of concrete, see Section 8.5.3 for more details. Beam B-06 obtained the highest load capacity, however, the testing was stopped after it reached 50 % of its maximum load. The decrease of load capacity was due to crushing of concrete in the compressive zone.

The beams in Figure 8.20 shows the behaviour for beams in 4-point bending test and exhibits the same general behaviour regarding ultimate load capacity and stiffness as beams in 3-point bending test. Beam B-01 reaches its ultimate load capacity for lower load in comparison to the others and has sudden drop afterwards. The sudden drop for beam B-01 was due to rupture of the bottom tensile reinforcement. Beam B-03 shows larger ultimate load capacity and obtained a more ductile response compared to beam B-01. Beam B-05 shows the highest ultimate load capacity and obtained a more ductile response compared to the other beams. Both beam B-03 and B-05 shows a sudden drop around the maximum load which were due to crushing of concrete.

Table 8.4 A summary of the results of reference beams tested in 3-point and 4-point bending test.

Beam	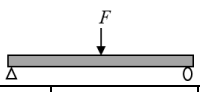				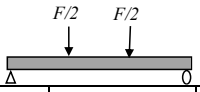			
	F_{max} **[kN]**	u_{max} **[mm]**	k_I **[kN/mm]**	k_{II} **[kN/mm]**	F_{max} **[kN]**	u_{max} **[mm]**	k_I **[kN/mm]**	k_{II} **[kN/mm]**
B-02	7.3	32.2	4.7	0.4	-	-	-	-
B-04	16.1	115.4	3.6	0.6	-	-	-	-
B-06	24.0	85.6	3.6	1.0	-	-	-	-
B-01	-	-	-	-	9.6	29.5	3.7	0.4
B-03	-	-	-	-	21.4	139.3	3.3	0.8
B-05	-	-	-	-	31.4	178.4	4.9	1.1

8.5.3 Failure Mode during Static Testing

In this section the failure mode of beam B-05 are presented during different drastic changes in load-deflection relationship. As illustrated in Figure 8.21 and Figure 8.22 different points are marked when sudden drops occur in the graph. The first drop between A1 and B1, crushing of concrete at the compressive zone occurred. Between A2 and B2, the beam experience spalling of concrete under the beam. The beam reached failure by rupture of reinforcement which could not be captured with DIC but confirmed by inspection at the end of the test.

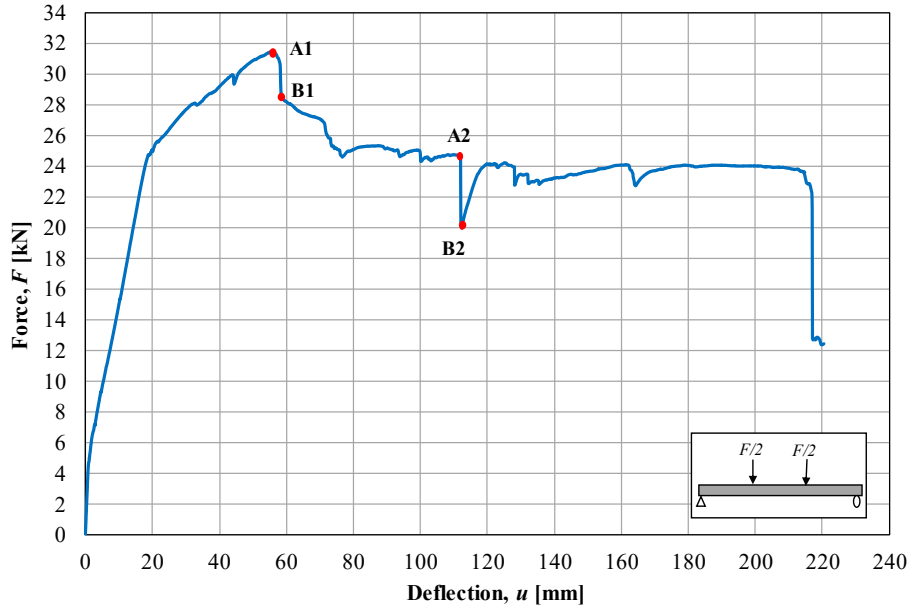

Figure 8.21 Illustrating vital points for the load-deflection curve.

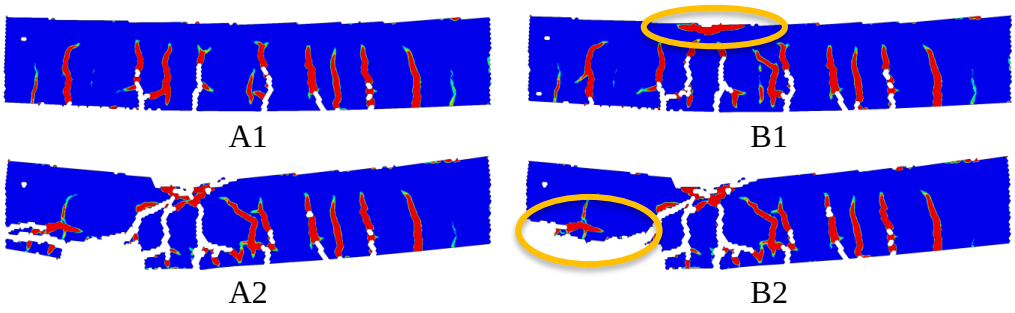

Figure 8.22 Images of the vital points in DIC shown in Figure 8.21.

8.5.4 Damaged Beams

A total of six damaged beams were tested in a 4-point bending test to determine the residual capacity. The reason why not all damaged beams were tested is due to the fact that some beams suffered severe localized damage to the compressive zone. As can be seen in the figures is that the curves are shifted in x-axis, this is the remaining plastic deflection after the repeated drop-weight impact. A summary of the static tests can be found in Table 8.5, it contains ultimate load capacity, maximum deflection, and the total plastic deflection of the beams. It is to be noted that the deflection u_F displayed in Figure 8.23 to Figure 8.25 is the deflection under the point load and not the midpoint deflection on the beams.

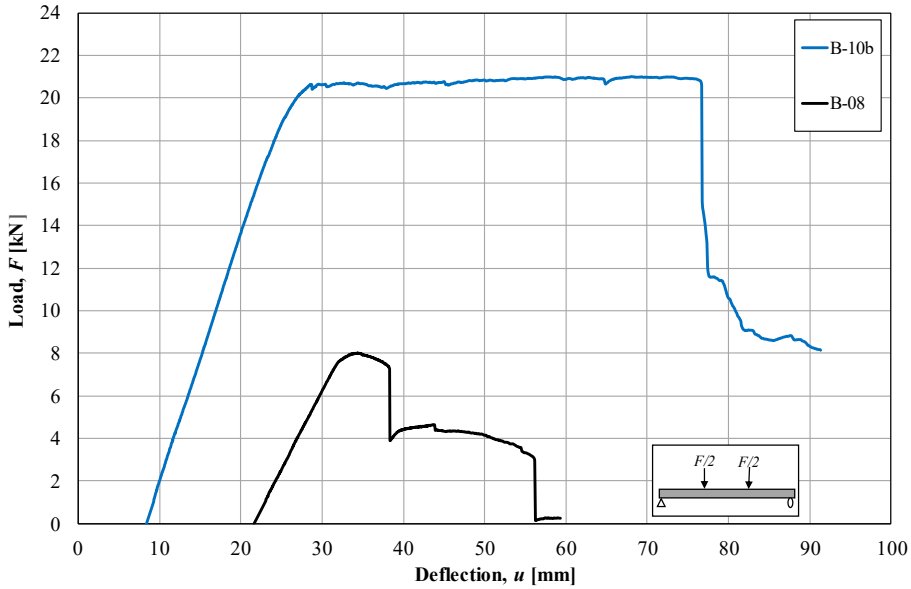

Figure 8.23 Illustration of the load-deflection curve of the damaged beams B-08 and B-10b.

The behaviour for the beams in series-I10 differ from each other, see Figure 8.23. The load increases linearly for beams B-08 and B-10b before reaching ultimate load capacity and plasticize almost linearly. Beam B-08 then displays a sudden drop after reaching maximum load capacity due to crushing of concrete and reaches failure by rupture of reinforcement. Beam B-10b illustrates a higher ultimate load capacity and a more ductile behaviour before reaching failure by crushing of concrete. Beam B-10b illustrates a higher internal work compared to beam B-08 as can be seen from the area under the curve and further explained Section 8.5.6.

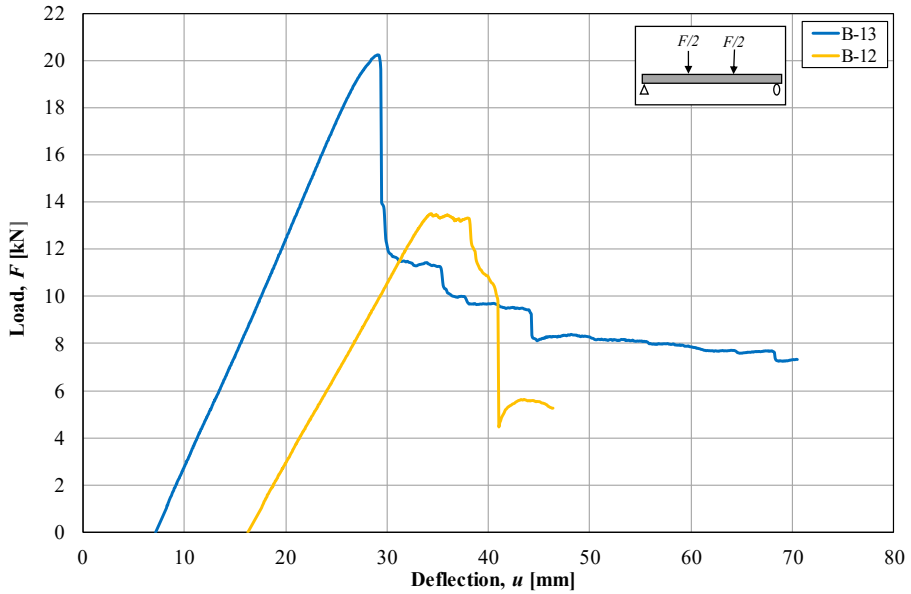

Figure 8.24 Illustration of the load-deflection curve of the damaged beams B-12 and B-13.

The behaviour for beams in series-I20 differ compared to series-I10, see Figure 8.24. However, the load increases linearly for both beams, until it reaches its ultimate load capacity. Beam B-12 and B-13 display a sudden drop after reaching its ultimate load capacity due to crushing of concrete. Although, beam B-13 illustrates a more ductile behaviour compared to B-12.

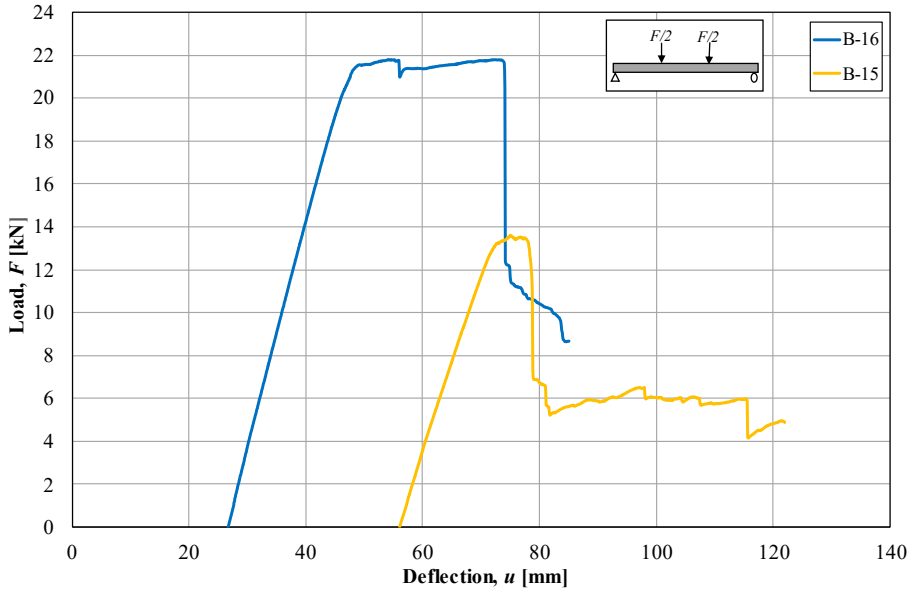

Figure 8.25 *Illustration of the load-deflection curve of the damaged beams B-15 and B-16.*

The behaviour for the beams in series-I40 differ from each other, illustrated in Figure 8.25. As seen previously, these beams also exhibit similar behaviour as before and the load increases linearly until reaching of ultimate loading capacity. Beam B-15 displays a sudden drop after reaching of ultimate load capacity due to crushing of concrete. Beam B-16 illustrates a higher ultimate load capacity and a more ductile behaviour before reaching of failure.

Table 8.5 *Summary of ultimate load capacity, stiffness in state II, maximum deflection, and plastic deflection.*

Beam	F/2 F/2			
	F_{max} [kN]	k_{II} [kN/mm]	u_{max} [mm]	u_{pl} [mm]
B-08	8.0	0.7	59	21.6
B-10b	21.0	1.1	91.4	8.4
B-12	13.5	0.7	46.4	16.3
B-13	20.2	0.9	70.4	7.2
B-15	13.6	0.8	121.9	56.1
B-16	21.8	1.0	85.1	26.6

8.5.5 Plastic Rotation

The plastic rotation for reference beams tested in 3- and 4-point bending can be seen in Figure 8.26 and Figure 8.27, respectively. A summary of the plastic rotation capacity for different load levels are presented in Table 8.6. The method used is described in a schematic illustration is presented in Appendix F.

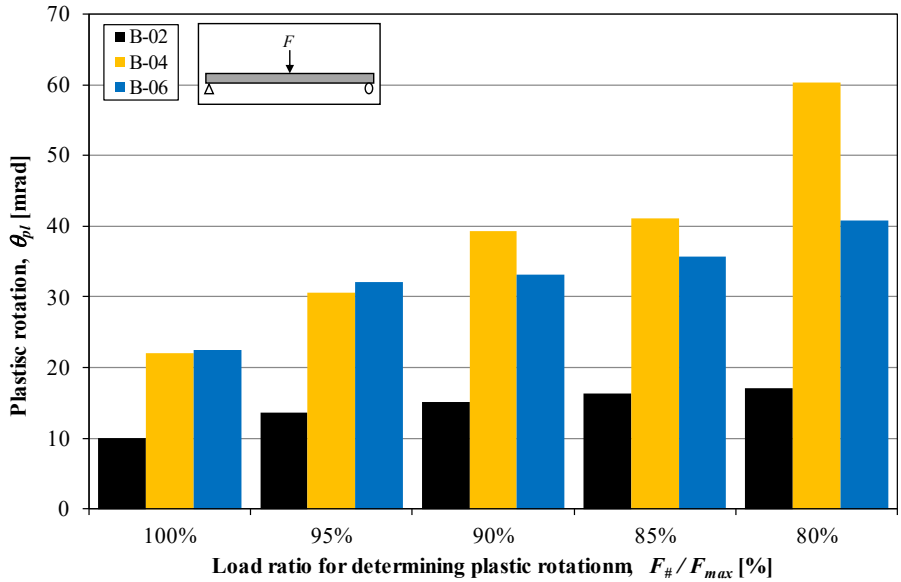

Figure 8.26 Plastic rotation capacity for the reference beams tested in 3-point bending test.

As illustrated in the Figure 8.26 the plastic rotation capacity is relatively similar for higher levels between beam B-04 and B-06. These beams exhibit similar behaviour during static testing. Beam B-02 displays a lower plastic rotation capacity compared to the other beams and reached failure due to rupture of reinforcement. Another observation for beam B-02 is that the plastic rotation capacity increases minorly for different levels. In contrast, beam B-04 displays a steady increment of plastic rotation capacity for different levels and a high value on plastic rotation for level 80 %. Beam B-06 displays a similar plastic rotation capacity between levels 95 % and 85 %.

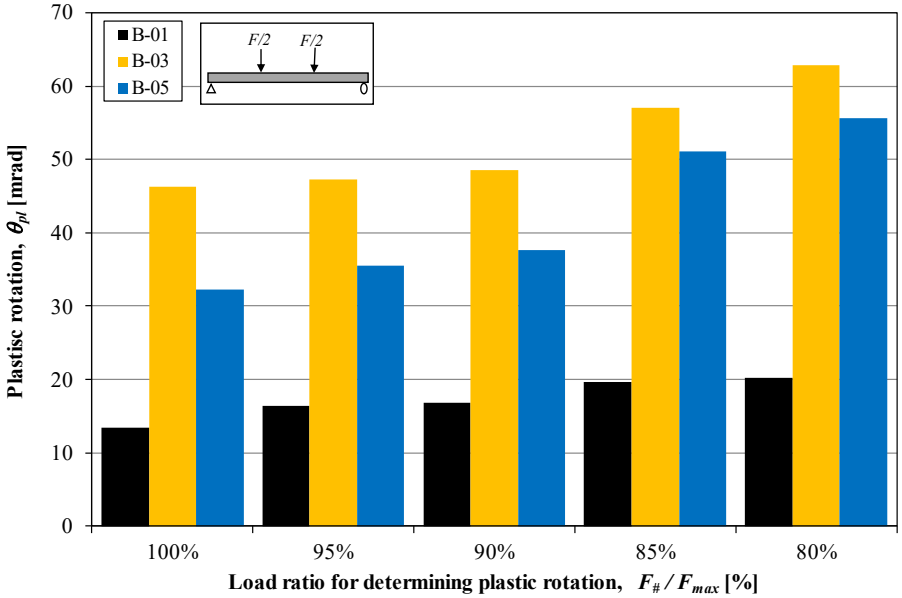

Figure 8.27 *Plastic rotation capacity for the reference beams tested in 4-point bending test.*

As can be seen in the Figure 8.27 the plastic rotation capacity for the beams differs from each other for all levels. Beam B-01 displays a lower plastic rotation capacity compared to the other beams. It can be observed for beam B-01 that the plastic rotation increases minorly for different levels and can be explained due to the brittle behaviour in the beam. Beam B-03 and B-05 displays higher plastic rotation capacity and increases for lower levels.

Table 8.6 *Summary of the plastic rotations for the reference beams for different load levels.*

Beams	**Loading configuration**	$\theta_{pl,100\%}$ **[mrad]**	$\theta_{pl,95\%}$ **[mrad]**	$\theta_{pl,90\%}$ **[mrad]**	$\theta_{pl,85\%}$ **[mrad]**	$\theta_{pl,80\%}$ **[mrad]**
B-02	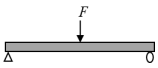	9.9	13.6	15.2	16.3	17.0
B-04		22.0	30.6	39.4	41.1	60.4
B-06		22.4	32.1	33.2	35.6	40.8
B-01	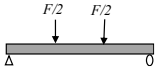	13.4	16.4	16.8	19.7	20.2
B-03		46.2	47.3	48.6	57.1	62.8
B-05		32.2	35.5	37.7	51.1	55.7

8.5.6 Internal Work

The internal work was determined both for the reference and dynamically tested beams. As explained in Section 8.5.1 the reference beams were divided into a 3- and 4-point bending test. The internal work was determined for different load levels starting at $F_{100\%}$, and descending down by 5 % to $F_{80\%}$, see Appendix H. In addition, the internal work was also determined for $F_{50\%}$. The internal work was determined as the area below the load-deflection curve and was calculated for each case, see Table 8.7. The total internal work for the beams that was tested dynamically was evaluated as static $W_{i,sta}$ combined with dynamic internal work $W_{i,imp}$. The stactic internal work is

calculated as the area below load-deflection curve and the dynamic internal work $W_{i,imp}$ is calculated based on Equation (4.23). For repeated impact the dynamic internal work is multiplied with the number of impacts during dynamic testing. The data for the calculation of dynamic internal work $W_{i,imp}$ is described in Appendix M. The method that was used to determine the internal work for reference beams is described in Section 4.4 and complemented with the method described in Appendix H. It is to be noted that the result from the drop-weight was not treated and the theoretical intial velocities $v_0 = 9.9$ m/s was used instead to evaluate the dynamic internal work.

The internal work for reference beams are presented in Figure 8.28 and Figure 8.29 and summarized in Table 8.7. The total plastic internal work for the beams is represented by the plastic internal work for levels 50 %.

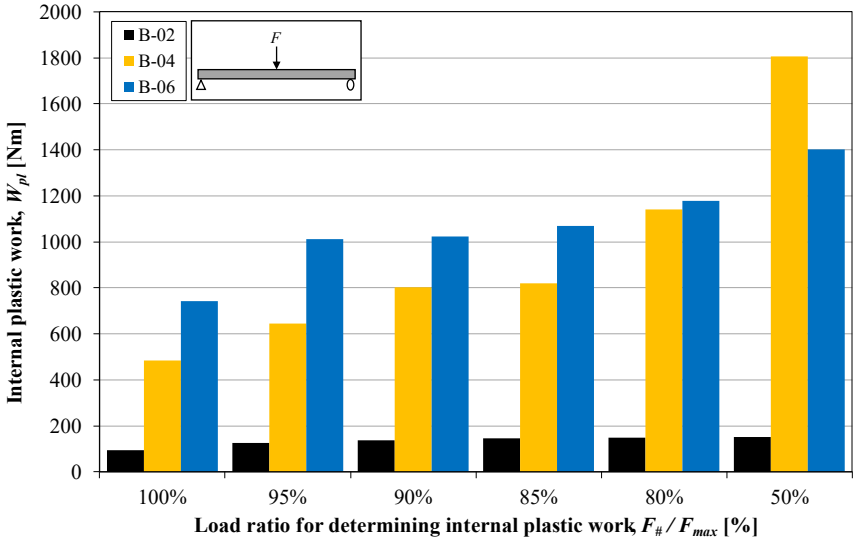

Figure 8.28 Comparison of the plastic internal work for the reference beams subjected to 3-point bending for different load levels.

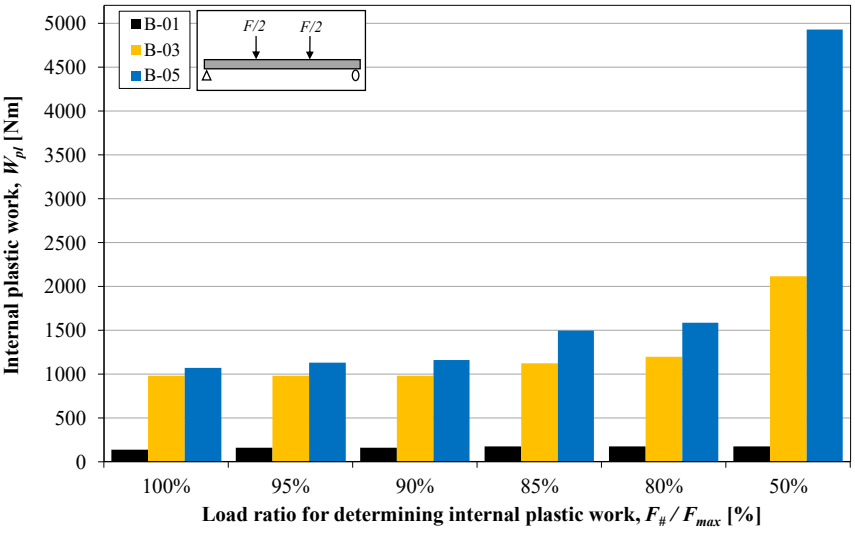

Figure 8.29 Comparison of the plastic internal work for the reference beams subjected to 4-point bending for different load levels.

Table 8.7 Summary of the plastic internal work for different levels for the reference beams subjected to both 3-point bending test and 4-point bending test.

Beam	Loading condition	W_{el} [Nm]	$W_{pl,100\%}$ [Nm]	$W_{pl,95\%}$ [Nm]	$W_{pl,90\%}$ [Nm]	$W_{pl,85\%}$ [Nm]	$W_{pl,80\%}$ [Nm]	$W_{pl,50\%}$ [Nm]
B-02	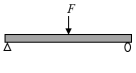	17	94	126	138	146	150	152
B-04		131	485	644	803	819	1142	1807
B-06		198	742	1012	1023	1068	1179	1402
B-01	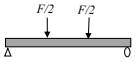	60	133	157	159	176	176	176
B-03		164	978	977	978	1117	1196	2110
B-05		262	1065	1130	1160	1497	1583	4925

The beams that were subjected to 3-point bending tests obtained less plastic internal work than the beams subjected to 4-point bending tests, see Figure 8.28 and Figure 8.29. The reason for this difference is explained in Section 3.6.2. Beams tested in 4-point bending test, generally result in longer plateu of ultimate load capacity which results in a larger area under the curve for the various load levels.

It can be observed that the internal energy increases with an increase in reinforcement diameter. Although, there is a clear distinction between reinforcement with 6 mm in comparison to the rest. The reason for this is the fact that reinforcement with 6 mm exhibited a poor tensile strength and reached failure by rupture of reinforcement, see Section 8.3.

An interesting observation can be made for beam B-04 compared to the beams in 3-point bending test. It illustrates a higher internal energy than the beam B-06 which has a larger reinforcement diameter. The reason behind this behaviour can be explained by the ductility in the reinforcement for beam B-04 which obtained a high yield strength.

Furthermore, there is a distinct difference between beams B-05 and B-06 as well, this could be explained that beam B-06 was stopped prematurely, i.e. before the reinforcement ruptured, and it is assumed that the beam would exhibit larger internal work before the reinforcement would rupture if the test had not been stopped.

The total internal work for reference beams and the beams tested dynamically are presented in Figure 8.30 and Table 8.8.

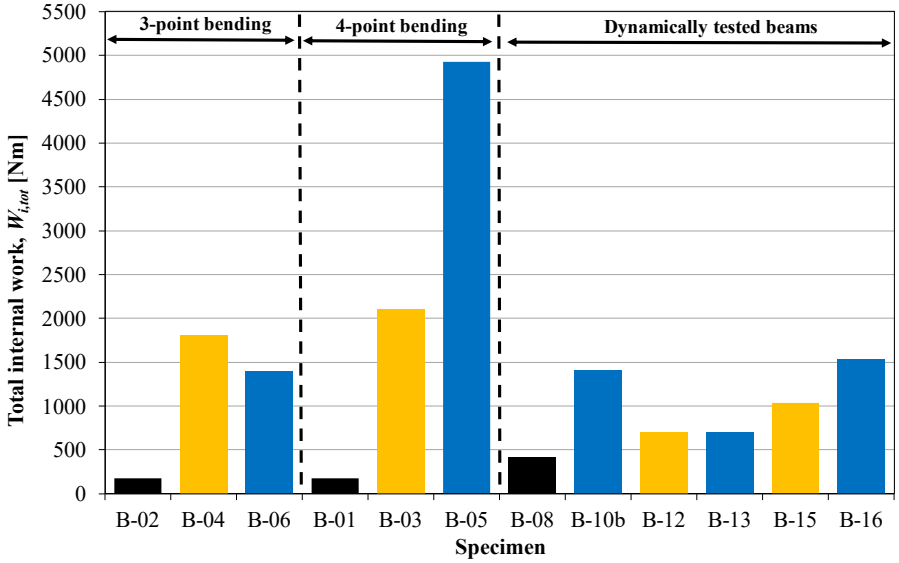

Figure 8.30 *An illustration of the total internal work for reference and the dynamically tested beams. The total plastic internal work is determined at 50 % of the ultimate load capacity.*

Table 8.8 *Summary of the static, dynamic, and total internal work for reference and dynamically tested beams.*

Beam	Loading configuration	$W_{i,sta}$ [Nm]	$W_{i,imp}$ [Nm]	$W_{i,tot}$ [Nm]
B-02	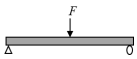	176	-	176
B-04		1807	-	1807
B-06		1402	-	1402
B-01		176	-	176
B-03		2110	-	2110
B-05		4925	-	4925
B-08	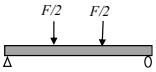	51	368	419
B-10b		1043	368	1410
B-12		80	619	700
B-13		80	619	700
B-15		93	941	1034
B-16		597	941	1538

For the reference beams, it can be observed that the total internal work increases with larger reinforcement, except for beam B-04 where it illustrates a higher internal work compared to B-06. It can be observed that beams tested dynamically resulted in lower internal work compared to the reference beams, except for beams with reinforcement diameters of 6 mm. The reason that the beams tested dynamically resulted in lower internal work is due to local damages to the compressive zone after repeated impact.

9 COMPARISONS OF EXPERIMENT RESULT WITH PREDICTIONS

9.1 Orientation

This chapter contains comparison between the measured load capacity and predicted load capacity, it also a comparison between the measured plastic rotation capacities and the different methods described in Section 3.7. Furthermore, a 2DOF model verification is evaluated to get a better understanding of the dynamic response.

9.2 Load Capacity

Load-deflection relationship for the reference beams are presented together with the predicted response, see Figure 9.1 and Figure 9.2. The stiffness in state I and II, and ultimate load capacity are summarized in Table 9.1 and Table 9.2, respectively. It can be noted that the dotted lines are the predicted using a tri-linear response.

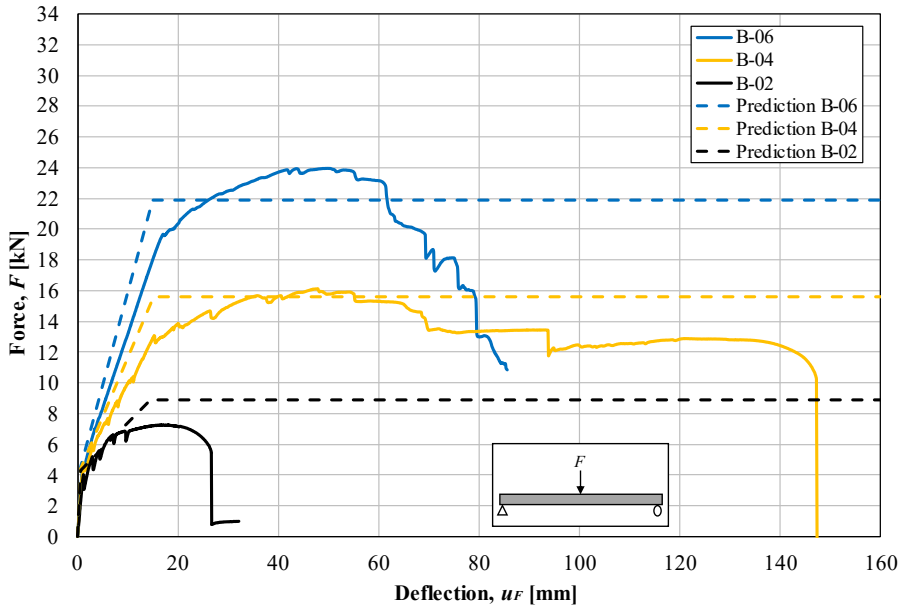

Figure 9.1 Load-deflection relationship for the reference beams subjected to a 3-point bending test plotted together with the predicted result.

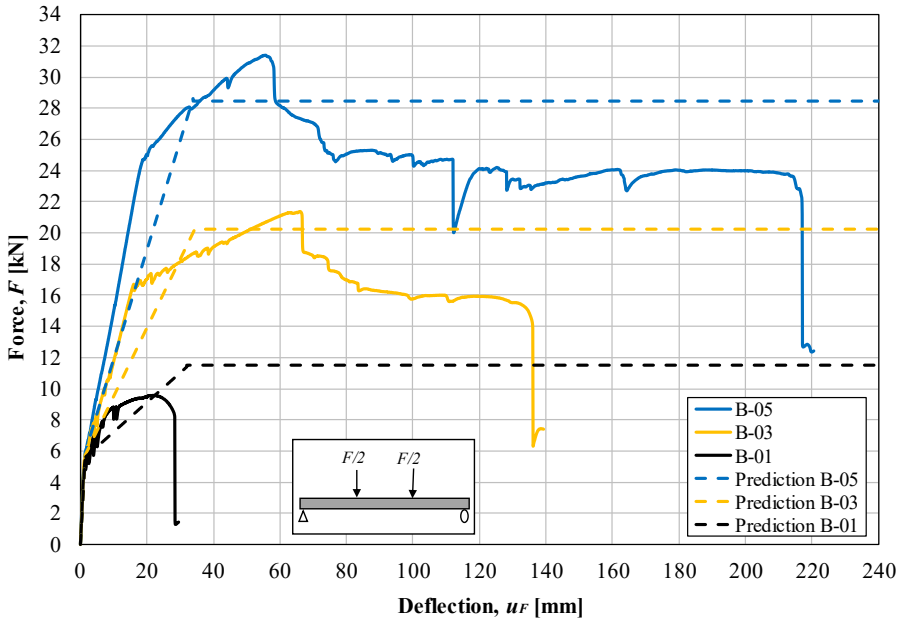

Figure 9.2 *Load-deflection relationship for the reference beams subjected to a 4-point bending test plotted together with the predicted result.*

Beams tested in a 3-point bending test is illustrated in Figure 9.1, the predicted response for beam B-02 overestimates the ultimate load capacity. Beam B-04 shows a good correlation between the ultimate load capacity and predicted response. However, the predicted response for beam B-06 underestimate the ultimate load capacity. There is a good correlation between the actual stiffness in state I and II with the predicted relationship for beams B-04 and B-06. The stiffness relation for beam B-02 does not correspond well.

Beams tested in a 4-point bending test are illustrated in Figure 9.2, it exhibits similar results between the predicted response and the measured structural response as in the case for beams tested in a 3-point bending. The ultimate load capacity is higher for beams tested in a 4-point bending test compared to a 3-point bending test. It can be observed that the stiffness for beams in 4-point bending is higher compared to beams in a 3-point bending test, see Table 9.1.

Table 9.1 Stiffness in state I and state II for reference beams subjected to 3- and 4-point bending test.

Beam	Loading condition	Method	k_I	k_{II} or k_{cy}
B-02	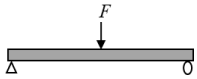	Measured	4.7	0.4
		Predicted	6.9	0.3
B-04		Measured	3.6	0.6
		Predicted	7.0	0.8
B-06		Measured	3.6	1.0
		Predicted	7.2	1.2
B-01	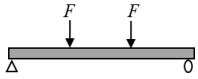	Measured	3.7	0.4
		Predicted	4.0	0.2
B-03		Measured	3.3	0.8
		Predicted	4.1	0.4
B-05		Measured	4.9	1.1
		Predicted	4.2	0.7

In Table 9.2 the ultimate load capacity from the testing and the predicted ultimate load capacity are presented. The ratio between the ultimate load capacity from experiment and the predicted ultimate load capacity are about the same for beams tested in 3-point bending compared to beams in 4-point bending.

Table 9.2 Ultimate load capacity for testing and predicted ultimate load capacity for reference beams.

Beams	Loading condition	$F_{u,exp}$ [kN]	$F_{u,pred.}$ [kN]	$\frac{F_{u,exp}}{F_{u,pred.}}$
B-02	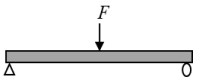	7.3	8.9	0.82
B-04		16.1	15.6	1.03
B-06		24.0	21.9	1.10
B-01	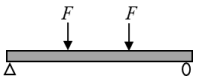	9.6	11.5	0.83
B-03		21.4	20.5	1.04
B-05		31.4	28.5	1.10

9.3 Plastic Rotation

The plastic rotation capacity for the reference beams subjected to a 3-point bending test are illustrated in Figure 9.3, Figure 9.4 and Figure 9.5. The plastic rotation capacity is presented for different levels together with different methods of plastic rotation explained in Section 3.7.

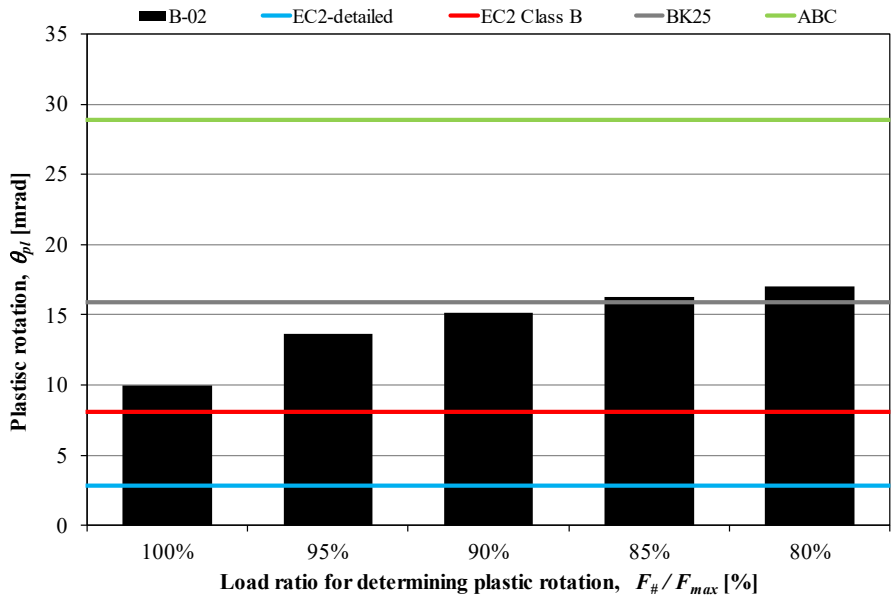

Figure 9.3 *The plastic rotation for a reference beam with a reinforcement diameter of 6 mm.*

For beam B-02, the ABC-method overestimate the plastic rotation capacity for all levels, see Figure 9.3. BK25-method overestimates the plastic rotation capacity for 100 % to 90 %, however, this method corresponds well for level 85 % and 80 %. EC2-method and EC2-detailed-method underestimates the plastic rotation for all levels except for level 100 % where EC2-method corresponds well.

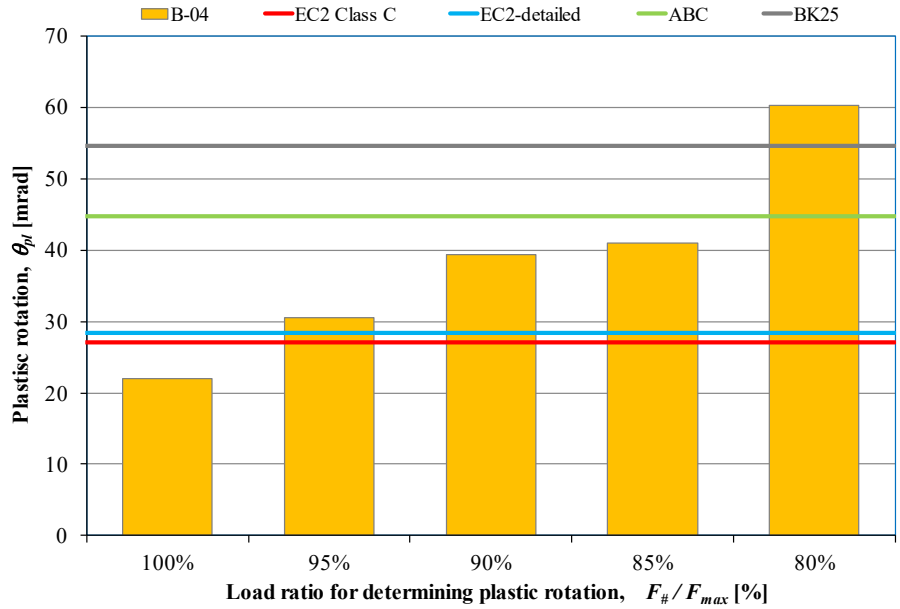

Figure 9.4 *The plastic rotation for a reference beam with a reinforcement diameter of 8 mm.*

As illustrated in Figure 9.4 the ABC-method and BK25-method overestimated the plastic rotation capacity for beam B-04 for all level except level 80 % where it underestimates. EC2-method and EC2-detailed-method underestimate the plastic rotation for all level except 100 % where it overestimates.

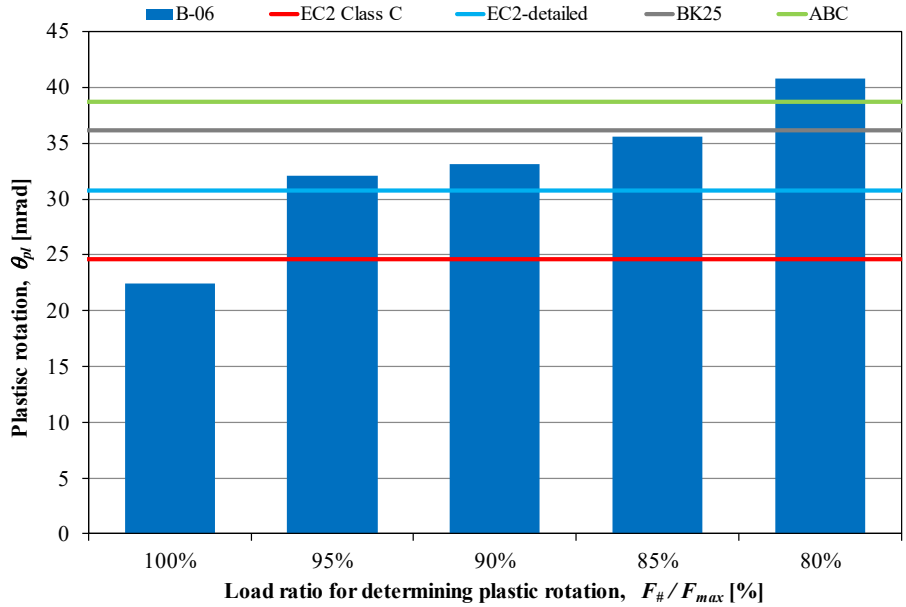

Figure 9.5 The plastic rotation for a reference beam with a reinforcement diameter of 10 mm.

As can be seen in Figure 9.5 the ABC-method overestimated the plastic rotation capacity for beam B-06 for all level except level 80 % where it corresponds well to the actual plastic rotation capacity. BK25-method overestimates for level 100 % to 90 %, and underestimate for 80 %. However, BK25-method corresponds well to level 85 %. EC2-method and EC2-detailed-method underestimates the plastic rotation capacity for all levels except 100 % where it overestimates.

9.4 Dynamic Response

Figure 9.6 to Figure 9.8 illustrates deflection over time for beams subjected to drop-weight impact in comparison with 2DOF prediction presented in Section 7.2.1 for the corresponding beams after first impact. It is to be noted that the 2DOF-model result in larger deflection over time compared to the tested beams most of the cases except for beams B-11a and B-12. One reason for the overestimation can be explained by the resisting force of the beam in 2DOF-model where it's assumed to be conservative.

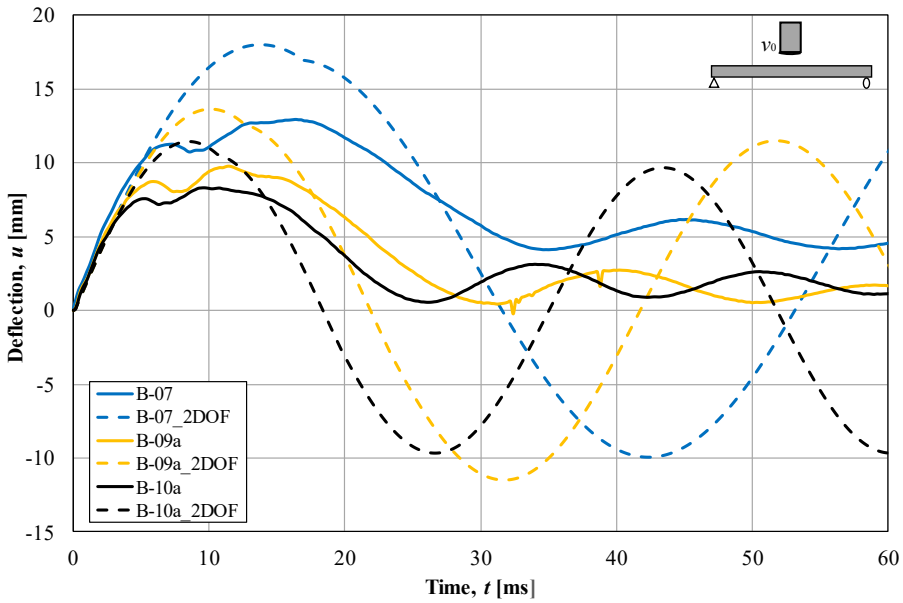

Figure 9.6 *Comparison of the relative deflection over time relation for the tested beams subjected to a drop-weight of 10 kg and the 2DOF model.*

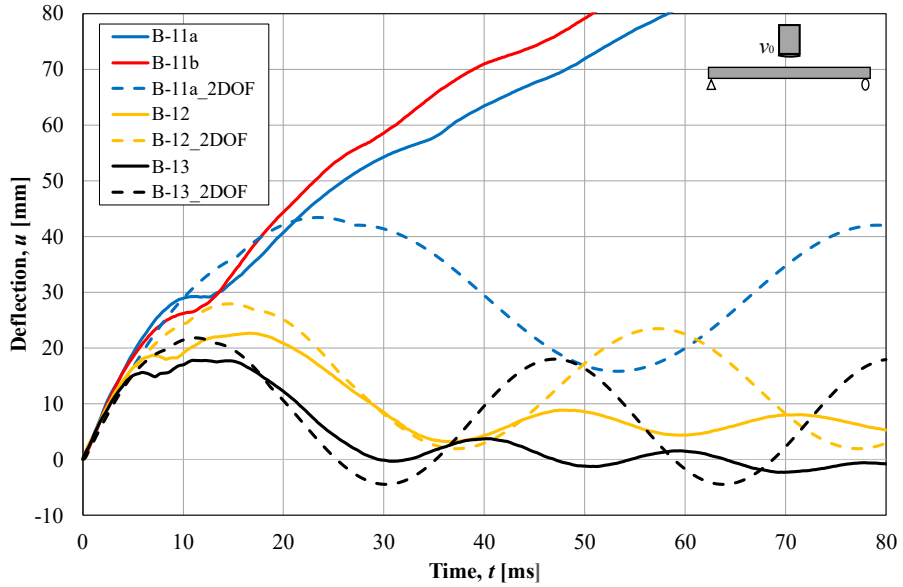

Figure 9.7 *Comparison of the relative deflection over time relation for the tested beams subjected to a drop-weight of 20 kg and the 2DOF model.*

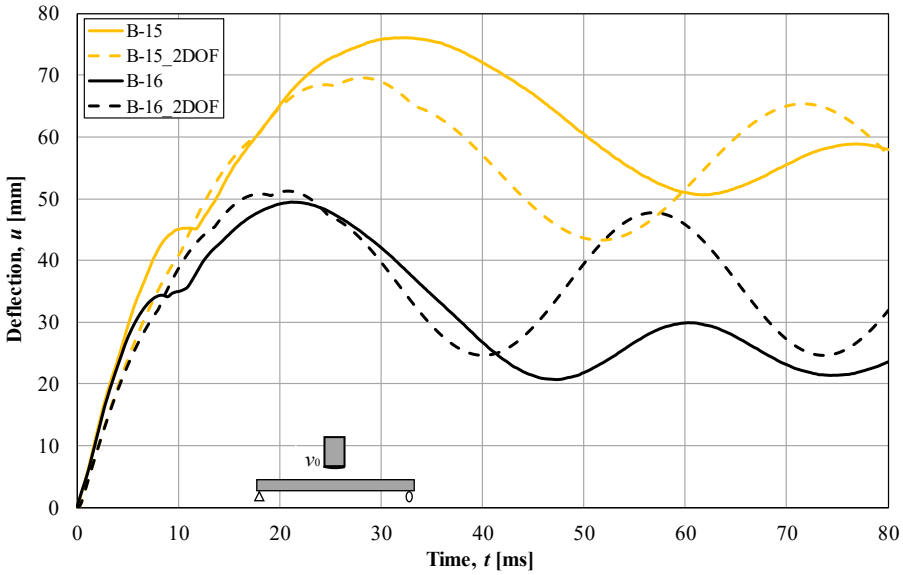

Figure 9.8 Comparison of the relative deflection over time relation for the tested beams subjected to a drop-weight of 40 kg and the 2DOF model.

In Table 9.3 the plastic deflection, total plastic deflection and maximum deflection are presented, respectively. The result for plastic deflection illustrates that the 2DOF-model underestimate for series-I10. For series-I20 and series-I40 the 2DOF model overestimate the plastic deflection. The result for total plastic deflection illustrates the same behaviour for the series, where the 2DOF model underestimate for series-I10 and overestimate for the other series.

The result for maximum deflection illustrates that the 2DOF-model overestimate compared to the tested beams. The overestimation of 2DOF can be explained by the assumed resistance of beams, where it is calculated conservatively. This will yield a higher deflection over time, higher plastic deflection and maximum deflection. Another explanation for this behaviour can be due to the strain rate of the beams that is not considered in the 2DOF-model. This strain rate effect would give a more representative behaviour of beams stiffness and strength in the material and result in lower deflection over time.

Table 9.3 Comparison of plastic deflections, total plastic deflections and maximum deflections for the tested beams and 2DOF models.

Series	Beam	u_{pl} [mm]	$u_{pl,2DOF}$ [mm]	$\frac{u_{pl}}{u_{pl,2DOF}}$ (%)	$u_{pl,tot}$ [mm]	$u_{pl,tot,2DOF}$ [mm]	$\frac{u_{pl,tot}}{u_{pl,tot,2DOF}}$ (%)	u_{max} [mm]	$u_{max,2DOF}$ [mm]	$\frac{u_{max}}{u_{max,2DOF}}$ (%)
I10	B-07	6.2	3.5	177	37.1	21.4	173	12.9	18.0	72
	B-09a	2.0	0	-	2.1	0	-	9.8	13.6	72
	B-10a	1.7	0	-	3.2	0	-	8.3	11.4	73
I20	B-11a [1)]	-	28.9	-	-	28.9	-	-	43.4	453
	B-12	6.7	12.7	53	14.2	26.7	53	22.6	27.9	81
	B-13	2.8	6.7	42	5.0	14.2	35	17.8	21.8	82
I40	B-15	55.2	54.3	102	55.2	54.3	102	76.0	69.5	109
	B-16	25.5	36.2	70	25.5	36.2	70	49.4	51.3	96

[1)] *B-11a reached failure after first impact loading.*

10 DISCUSSION

10.1 Material Properties

The concrete properties turned out to have somewhat higher compressive strength than expected. The concrete batch was aimed to be in class C40/50, the mean compressive strength indicate that the material was closer to a strength of C45/55.

The result for reinforcement properties showed that the reinforcement with diameters of 6 mm resulted in low ultimate strain properties. The behaviour was closer to a cold worked steel and showed low value in yielding strength, ultimate strength, and ultimate strain. By looking at Table 2.1 this reinforcement was categorized as class A. The low strength on the reinforcement with diameters of 6 mm could be noticeable in the result from static and dynamic testing.

10.2 DIC

Overall, it is noted that DIC proved to be a powerful tool when it comes to analysing strains and deformations of the beams. However, there are certain limitations, during the tests for repeated impact loading. The beams suffered major localized damage in the form of crushing of concrete at the top of the beam and occasional spalling under the beam which caused the speckly pattern not to be visible. In some instances, the spalling from the beams fell in front of the camera and during post processing in DIC this resulted in localized unreadable images. It is therefore suggested that if these experiments were to be performed again, a protective plate of e.g., rubber, would be placed on top of the beam and thus, would distribute the force in a more favourable way and local damages might be avoided. This was the case for beam B-11b; however, its behaviour was not investigated in detail. Another possible solution to this problem could be to repaint the damaged areas so that the beam can be evaluated during that impact. However, this would be a solution for each respective impact and would not fix the issues that occur when comparing different impacts.

When it comes to facet calibration, it would be interesting to perform tests and investigate how a change in facet settings affect the overall outcome of both deformation and strain fields. The facet settings that were used was based on a similar study performed by Eriksson and Gustafsson (2021) and was therefore, set to a facet distance of 15 pixels and a point distance of 5 pixels. Simultaneously, the strain % was also chosen to be between 2 % and 1.2 % based on a similar study performed by Jönsson and Stenseke (2018). However, when it comes to the strain images these were not as clear as the images from previous studies. Thus, it is unclear if these settings are optimal, as one thing to note is that the beams from previous studies are shorter and it is not necessarily the same calibration for the beams with longer spans.

10.3 Dynamic Testing

In Section 9.4 the deflection over time for the first impact of the beams was compared with the result from 2DOF prediction. The result from 2DOF model overestimated the deflection most of the cases except for beams B-11a and B-15, where it underestimated. The reason for the overestimation can be explained by the conservative assumption regarding the resistance of the beams. Another reason for the overestimation is that the

2DOF-model can be explained by the strain rate that is not considered in the 2DOF model. The strain rate in the model would have resulted in a greater stiffness of the beams and therefore given a more representative deflection over time. The actual plastic deflection for beam B-07a was higher than the 2DOF model which can also be explained by the resistance in the beam. For this case the predicted structural response overestimated the ultimate load capacity which made the 2DOF model less conservative.

One thing to discuss when it comes to the deflections and dynamic setup is that there are some impacts where the plastic deflections decrease after a successful impact. A possible reason for this might be that in between the impact, a hydraulic lift was used and placed right underneath the middle of the beam. Afterwards, the beam was lifted in place which could explain the reason for this behaviour, and it would need to be studied further.

Since there was delays in the lab, which postponed the post-processing of this thesis. The comparison between the drop-weight acceleration in DIC and the accelerometer was not performed. It is not entirely clear how the accelerometer data is supposed to get filtered to be compared to the DIC drop-weight data.

10.4 Strain Fields

The effect of reinforcement is discussed in Section 8.4.1.2 where beams with larger reinforcement resulted in smaller cracks for different time intervals. Bending cracks in the upper and lower regions was less visible and the beam B-10a also illustrated a horizontal crack. By studying the effect of drop-weight it can be observed that the beams subjected to a drop-weight of 20 kg compared to 10 kg resulted in more bending cracks, shear cracks and horizontal cracks. This could also be observed for beams subjected to 40 kg compared 10 kg. For the case with repeated impacts, the localized damage was visible after a few drops for a beam with reinforcement diameter of 6 mm. However, for the beams with reinforcement diameter of 8 mm and 10 mm, a horizontal crack was visible before local damages occurred. One thing to noted is that the localized spalling made it difficult to evaluate the cracks under the impact area.

10.5 Static Testing

Beams were tested both in 3- and 4-point loading to evaluate the structural response and residual capacity. It can be noted that all beams that were tested dynamically was not tested statically due to local damages that occurred in the impact area. It was preferred to only use 3-point bending tests for all beams to get a more representative behaviour of the response but was not possible due to local crushing in the compressive zone. The choice of 4-point bending test made it not possible to evaluate and compare the plastic rotation capacity with the predicted plastic rotation capacity.

The predicted structural response of the reference beams showed a varied result. The predicted response underestimates the ultimate load capacity for the beam with reinforcement diameters of 10 mm and 8 mm. The predicted response for beam with reinforcement diameters 6 mm overestimated which can be explained by reinforcement properties. Another explanation to overestimation can be due to the actual location of the reinforcement compared to nominal location. One theory is that the bottom

reinforcement in the beam has lifted due to use of vibrators during casting. The vibrators were used to even out the concrete in the form, it can also have pressed the reinforcement out of place because of the thin layer of steel wire it hanged on. However, this was not confirmed by measuring the final location of the steel reinforcement.

The plastic rotation capacity was predicted by using methods previously explained in Section 3.7. ABC-method and BK25 method overestimate for most levels. EC2-method and EC2-detailed-method underestimated for most of the levels. However, EC2-detailed corresponds well with level 95 % for beam B-04 and B-06.

The internal work for the reference beams showed larger internal work in 4-point bending test compared to 3-point bending test. This can be explained by the moment distribution for the different load configurations, a 4-point bending test is closer to a distributed load which would lead to a more ductile response, hence, a more effective way to absorb energy. The dynamically tested beams exhibit less internal work in comparison to the reference beams. This can be explained by the damaged that the dynamically beams experienced during repeated impacts.

11 CONCLUSIONS

11.1 General

The aim of this master thesis is to better understand the structural response of reinforced concrete subjected to single and repeated impact. This was achieved by performing experiment both dynamically and statically on reinforced concrete beams with varied reinforcement ratio. The dynamically tested beams where subjected to a drop-weight mass of 10-40 kg which was dropped a single or repeated times. Some of these beams were tested statically subsequently together with reference beams to evaluate the residual capacity. The response of the beams was captured using high-speed or ordinary cameras and evaluated with Digital Image Correlation (DIC).

The effect of reinforcement ratio, drop-weight mass and number of impacts could be seen in most of the result. The result indicates that a given impact energy, applied in the form of repeated impacts creates a more critical case than the loading from a single impact. From evaluation of the static response, it can be concluded that beams tested dynamically generally resulted in a decrease in the structure's energy absorption compared to the beams tested statically only. This was also the case for beams subjected to repeated impact.

DIC was used to evaluate single and repeated impact and was very useful to get an understanding of the deflection over time and the development of cracks for different time intervals.

The impact result was generally hard to predict regarding repeated impact. The beams that were subjected to single and repeated impact resulted in local damages in the compression zone. This made it difficult to perform analysis in the DIC to get a representative behaviour of the beam and different methods was used to compensate for these difficulties.

The 2DOF model overestimated deflection over time compared to experimental results. This could be explained by the assumed resistance of the beams in 2DOF model. However, 2DOF model prediction is on the safe side and can be used to get a general understanding of the response.

The predicted structural response underestimated the ultimate load capacity for beams with reinforcement diameters of 8 mm and 10 mm while beam with reinforcement diameters of 6 mm overestimated the load capacity. The predicted stiffness, though, corresponded well with that in tests.

It was found that static loading in 4-point bending resulted in a higher plastic rotation capacities and energy absorption capacities compared to static loading in 3-point bending. The plastic rotation capacity could be estimated well using a more detailed version of the method described in Eurocode, it was concluded that EC2-detailed-method corresponded well with beams with reinforcement diameters of 8 mm and 10 mm.

11.2 Further Studies

In this thesis the effects of a reinforced concrete beam subjected to both single and repeated impact loading have been studied. However, there are several aspects which were not studied in detail and could be examined in either a later stage or in a new study.

The experimental setup could be changed in a way to avoid crushing of concrete in the compressive zone. This would prevent that the dynamic tests to be stopped early due to damages in the compressive zone. Another reason for this change, is that the residual capacity of the damaged beams can be tested in a 3-point bending test instead of a 4-point bending test. This could then be built further upon, and the residual capacity could be tested after each drop, which could then be compared to each other to determine when the most damaging impact occurs.

Additionally, the response of the drop-weight could be evaluated and analysed. A comparison between the drop-weight in DIC and the accelerometer could then be performed. Once this has been completed, it would be interesting to see if repeated loading can be implemented in a Finite Element analysis. Then a study between the experimental data and the Finite Element analysis can be carried out and analysed.

Calculations on the plastic rotation capacity has only been evaluated for the case where the beams are subjected to a 3-point bending test. It would be interesting to see these calculations and evaluation to be performed for the case where the beams are subjected to a 4-point bending test. Another interesting aspect would be to place the position of the top of the beam reinforcement higher, to have the reinforcement acting in compression instead in tension. It would be interesting to see a study between the original position of reinforcement in comparison to the one with a smaller concrete cover.

12 REFERENCES

Al-Emrani, M., Engström, B., Johansson, M., & Johansson, P. (2013). *Bärande konstruktioner Del 1* (Rapport 2013:1, Vol. 2013, Issue 1). Chalmers University of Technology.

Andersson, M., Pettersson, E. (2019). Reinforced Concrete Beams Subjected to Drop-Weight Impact Experimental study of the influence of reinforcement properties on the structural response (Master's thesis, Chalmers University of Technology, Institution of Architecture and Civil Engineering).

Betonghandboken. (1990). *Betonghandboken – Konstruktion* (K. Cederwall, M. Lorentsen, & L. Östlund, Eds.; utgåva 2). Svensk Byggtjänst.

CEN. (2005). *SS-EN 1992-1-1:2005: Eurocode 2: Design of concrete structures – Part 1-1: General rules and rules for buildings* (Edition 1). European Committee of Standardization. www.sis.se

CEN (2009). SS-EN 12390-3:2001: Testing Hardened Concrete – Part 3: Compressive strength of test specimens.

Engström, B. (2015). *Design and analysis of continuous beams and columns* (Edition 2015). Chalmers University of Technology.

Eriksson, E., & Gustafsson, V. (2021). *FRP Strengthened Reinforced Concrete Beams Subjected to Drop Weight Impact and Static load.* Chalmers University of Technology.

Fortifikationsförvaltningen. (1973). *Provisoriska anvisningar för dimensionering av armerade betongkonstruktioner som skydd mot verkan av konventionella vapen inom närmissområde.: Vol. Publ nr 25:1*. Befästningsavdelningen.

Goodno, B. J., & Gere, J. M. (2021). *Mechanics of Materials* (Ninth Edition). Cengage Learning.

Johansson, M. (2000). *Structural Behaviour in Concrete Frame Corners of Civil Defence Shelters Non-linear Finite Element Analyses and Experiments*. Chalmers University of Technology.

Johansson, M. (2012). *Beräkning av impulsbelastad konstruktion 1 (4) Beräkningsanvisning för strukturrespons Central differensmetod 1 Orientering 1*.

Johansson, M. (2014). *Johansson (2014) - Beräkningsmetodik stötlast_MJ_140505b_sid 8-32*.

Johansson, M., & Ekengren, B. (2014). *Beräkning av impulsbelastad konstruktion 1 (15) Beräkningsanvisning för strukturrespons Strukturrespons vid impulsbelastning*. Swedish Civil Contingencies Agency.

Johansson, M., Hallgren, M., Ansell, A., & Leppänen, J. (2021). *Plastisk deformationsförmåga och tvärkraftsrespons hos impuls-belastade betongkonstruktioner*.

Johansson, M., & Laine, L. (2012). *Bebyggelsens motståndsförmåga mot extrem dynamisk belastning, Del 3-Kapacitet hos byggnader*. Swedish Civil Contingencies Agency.

Jönsson, J., & Stenseke, A. (2018). *Concrete Beams Subjected to Repeated Drop-Weight Impact and Static Load Assessment of structural response in experimental testing and predicted response with numerical analyses*. Chalmers University of Technology.

Lovén, J., & Svavarsdóttir, E. S. (2016). *Comparison of experimental data and numerical modelling*. Chalmers University of Technology.

Lozano, F. M., & Makdesi, J. A. (2017). *Concrete Beams Subjected to Drop-Weight Impact and Static Load Structural Behavior and Plastic Rotational Capacity from Experiments and Finite Element Analysis*. Chalmers University of Technology.

Löfgren, I., Olesen, J. F., Flansbjer, M. (2004) Application of WST-method for fracture testing of fibre-reinforced concrete.

Nigani, Y. Z., & Nordström, G. (2020). *FRP Strengthened RC Beams Subjected to Drop Weight Impact and Static load*. Chalmers University of Technology.

Nozad, A., & Steiner, M. (2021). *Average reinforcement strain in reinforced concrete structures loaded until failure*. Chalmers University of Technology.

Software GOM Correlate. n.d. http://www.gom.com/3d-software/gom-correlate.html

Zilch, K., & Zehetmaier, G. (2010). Bemessung im konstruktiven Betonbau (2nd edition). Springer Verlag.

APPENDIX A Construction of Concrete Forms

There were two identical forms made of form plywood. The reasoning for this choice of material was to obtain a smooth concrete surface. The form-plywood board that was used were of the dimensions 3000x1500x18 mm, which were then sawn into longitudinal pieces of 2800x200 mm with a wall saw.

After this, the pieces on the short side of the form were created. These boards were of the size 1080x200 mm, where holes for the reinforcement were made. The holes were marked with a centre-to-centre distance of 40 mm to ensure a concrete cover of 37, 36 and 35 mm vertically. In contrast to this, the horizontal concrete cover was marked with a line of 20 mm. The holes were then drilled with a distancer of 9 mm, this was used since the holes needed to be all the same length as it made the cutting of the reinforcement easier.

Lastly, before the assembly of the forms. Distancers were created as a rectangle from the left-over form-plywood pieces with a width of 100 mm and a height of 200 mm. This was used to ease the process of maintaining 90 degrees between the longitudinal pieces and to ensure that the width and height were consistent. The overlaying supports with an inner distance of 1080 mm were created; these were used on top of the forms to ensure that the outer longitudinal boards do not buckle when concrete is poured.

The assembly started with marking and predrilling holes on a 3000x1500x18 mm board. This was done to know where the longitudinal boards were supposed to be placed and then drilled from underneath. It was done for all 10 longitudinal pieces of wood, where the horizontal distance between the screws was 118 mm to get a second insurance of the width of each respective beam. The board on the short side was drilled onto a platform and then clamps were used to hold the first longitudinal board into place. This method was a safe method to use since it insures an angle of 90 degrees between the platform and boards. Further, after the first longitudinal had been screwed into place, the rectangular distancers were clamped together with the next board before screwing them into the platform from underneath. This was performed to maintain the 90-degree angle and keep the width as close to 100 mm as possible. Finally, the boards on the short side were unscrewed from underneath and new screws were drilled into the longitudinal ones, this was done to ease the process of getting the concrete beams out of the mould. The finished mould can be seen in Figure A.1.

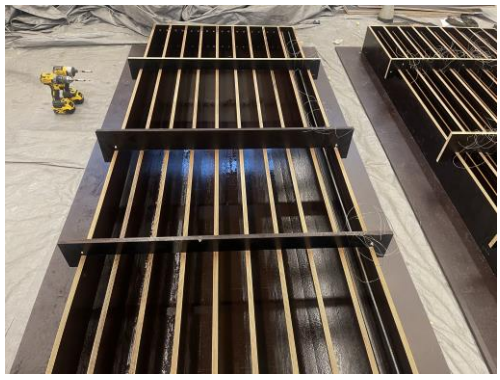

Figure A.1 Finalized mould with the overlaying support drilled on top.

APPENDIX B Reinforcement Tensile Tests

The reinforcing steel was aimed at a quality of class C and the reinforcement bars were tested in a tensile strength. The results can be seen in Figure B.1, Figure B.2 and Figure B.3 for reinforcement diameter of 6 mm, 8 mm, and 10 mm, respectively. The results are summarized in Table B.1 to B.4. The reinforcement diameter of 8 mm and 10 mm met the quality of class C, however, the reinforcement diameter of 6 mm did not and is in line with class A, see Section 2.2.

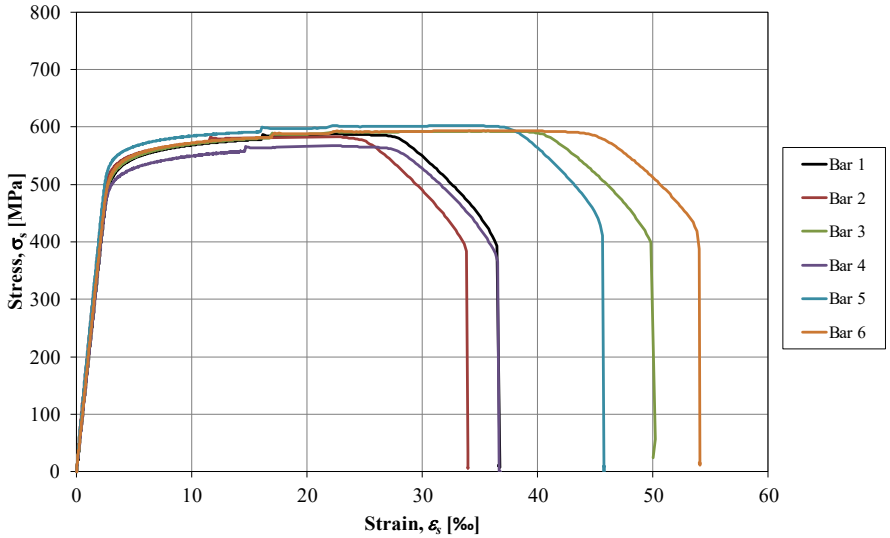

Figure B.1 Stress-strain curves for six reinforcement bars with 6 mm diameter.

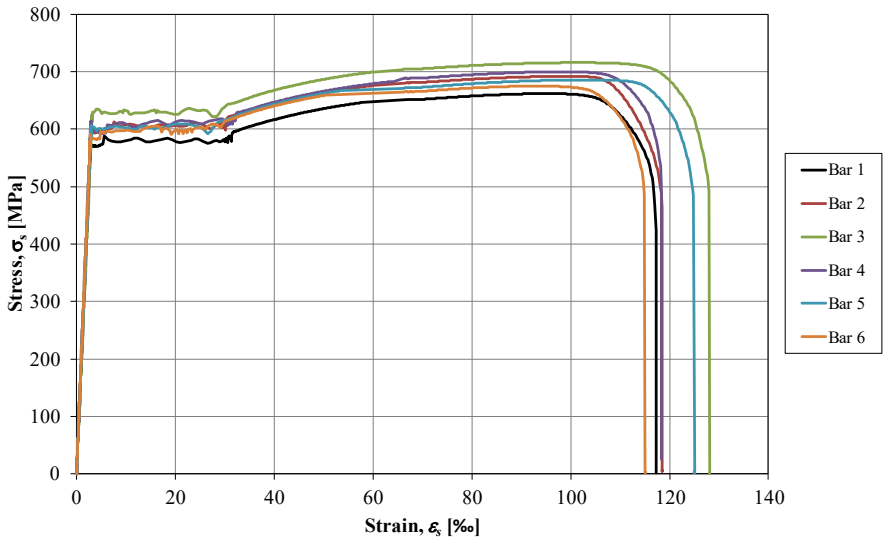

Figure B.2 Stress-strain curves for six reinforcement bars with 8 mm diameter.

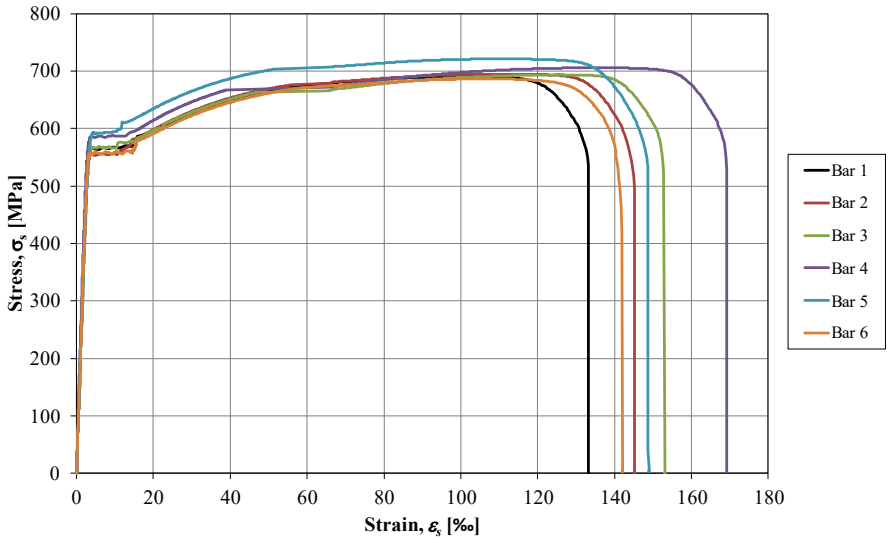

Figure B.3 Stress-strain curves six reinforcement bars with 10 mm diameter.

Table B.1 Steel properties for reinforcement with a diameter of 6 mm.

Specimen Ø6 *mm*	$\varepsilon_{0.2}$ **[%]**	ε_{su} **[%]**	$f_{0.2}$ **[MPa]**	f_u **[MPa]**	$f_u/f_{0.2}$ **[-]**	E_s **[GPa]**
1	0.49	2.2	545	588	1.08	187
2	0.46	2.3	549	583	1.06	219
3	0.48	3.6	546	593	1.09	192
4	0.47	2.2	526	568	1.08	187
5	0.47	3.3	564	602	1.07	221
6	0.48	3.6	550	594	1.08	195
Average	0.48	2.9	547	588	1.08	200

Table B.2 Steel properties for reinforcement with a diameter of 8 mm.

Specimen Ø8 *mm*	ε_{sy} **[%]**	ε_{su} **[%]**	f_y **[MPa]**	f_u **[MPa]**	f_u/f_y **[-]**	E_s **[GPa]**
1	0.28	9.5	566	662	1.17	201
2	0.29	9.9	597	692	1.16	206
3	0.31	10.1	621	716	1.15	195
4	0.29	9.9	614	700	1.14	211
5	0.27	10.3	559	686	1.23	210
6	0.27	9.3	574	675	1.18	215
Average	0.29	9.8	588	688	1.17	206

Table B.3 Steel properties for reinforcement with a diameter of 10 mm.

Specimen ∅10 mm	ε_{sy} **[%]**	ε_{su} **[%]**	f_y **[MPa]**	f_u **[MPa]**	f_u/f_y **[-]**	E_s **[GPa]**
1	0.40	10.2	566	691	1.22	201
2	0.41	11.2	557	695	1.25	198
3	0.35	12.6	567	694	1.22	202
4	0.31	13.6	572	706	1.23	227
5	0.43	11.0	593	721	1.22	191
6	0.49	10.7	559	686	1.23	198
Average	0.40	11.6	569	699	1.23	203

Table B.4 Summary of mean values for reinforcement steel.

Property	**Mean Values [ϕ6 mm]**	**Mean Values [ϕ8 mm]**	**Mean Values [ϕ10 mm]**	**K500A**	**K500B**	**K500C**
$f_{0,2}$ or f_y [MPa]	546	588	569	500	500	500
f_u [MPa]	588	688	699	525	540	575
f_u/f_y [-]	1.08	1.17	1.23	1.05	1.08	1.15
ε_{su} [‰]	29	98	116	25	50	75
E_s [GPa]	200	206	203	200	200	200

APPENDIX C Concrete Material Tests

The concrete strength was aimed at C40/50 and the compressive strength was tested at 28, 57 and 64 days which can be seen in Table C.1 to C.4. A wedge-splitting test was also performed at 57 days and can be seen in Table C.5 and in Figure C.1.

Table C.1 Summary of density and compressive strength tested for a cube at 28 days.

Name	**Age [Days]**	**Density** $\left[\frac{kg}{m^3}\right]$	**Compressive strength cube,** $f_{cm,cube}$ **[MPa]**
Specimen 1	28	2376	66.4
Specimen 2	28	2372	66.0
Specimen 3	28	2390	65.7
Average	28	2379	66.0

Table C.2 Summary of density and compressive strength tested for a cube at 57 days.

Name	**Age [Days]**	**Density** $\left[\frac{kg}{m^3}\right]$	**Compressive strength cube,** $f_{cm,cube}$ **[MPa]**
Specimen 4	57	2391	72.0
Specimen 5	57	2383	68.0
Specimen 6	57	2383	69.8
Average	57	2386	69.9

Table C.3 Summary of density and compressive strength tested for a cube at 64 days.

Name	**Age [Days]**	**Density** $\left[\frac{kg}{m^3}\right]$	**Compressive strength cube,** $f_{cm,cube}$ **[MPa]**
Specimen 7	64	2348	71.3
Specimen 8	64	2356	68.9
Specimen 9	64	2383	71.1
Average	64	2362	70.4

Table C.4 Summary of average concrete properties for specimens at 28, 57 and 64 days.

Days	Mean compressive strength, f_{cm} [MPa]	Mean tensile strength, f_{ctm} [MPa]	Modulus of Elasticity, E_{cm} [GPa]
28	55.0	3.9	36.7
57	58.3	4.1	37.3
64	58.7	4.1	37.4
Average	57.3	4.0	37.1

Table C.5 Summary of wedge-splitting properties for specimens at 57 days.

Specimen ID	Accumulated fracture energy, G_F [Nm/m^2]	$F_{sp,max}$ [kN]
WST-1	175	6.5
WST-2	141	6.3
WST-3	133	6.0
Average	150	6.3

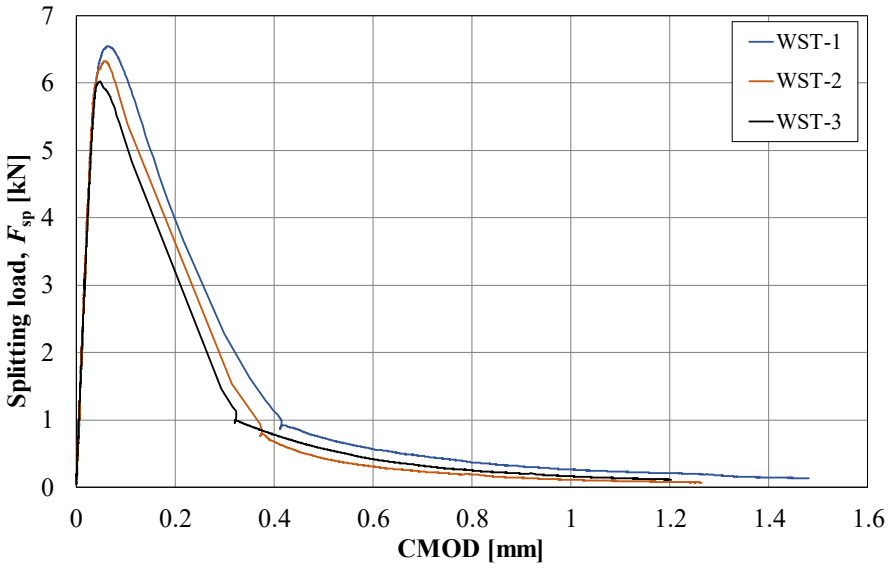

Figure C.1 The graph for the different wedge-splitting tests.

APPENDIX D Determination of Plastic Deflection with DIC

The plastic deflection on the dynamically tested beams was determined by using an image sequence method in GOM Correlate 2019 (GOM, 2019). A image of every beam was captured before impact and was used as a reference image. After impact loading an image was captured when the beams had stopped moving. These images where used together with calculation points to determine the plastic deflection for every impact, see Figure D.1.

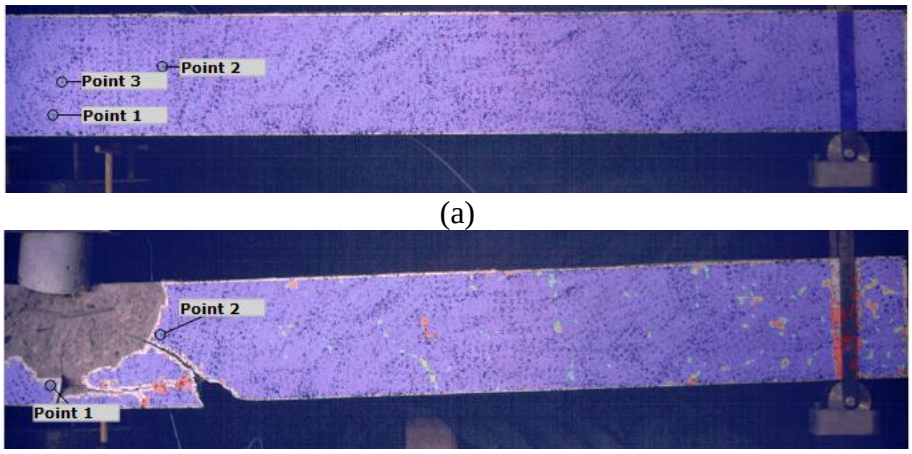

Figure D.1 Images of beam B-07: (a) before impact and (b) after fifth impact.

APPENDIX E Weight Loss after Dynamic Testing

The dynamically tested beams suffered crushing of concrete in the compressive zone and spalling underneath the beam. The weight loss is registered after each impact that caused damage to the beam is presented in Table E.1.

Table E.1 Summary of weight loss after repeated impact loading.

Beam	Impact	Weight loss after impact loading [kg]
B-07	2	1.06
	3	0.06
	4	0.28
	5	1.44
B-08	1	0.22
B-09a	5	9.74
	6	2.78
B-09b	5	6.10
	6	3.06
B-10a	3	0.28
	4	0.64
	5	2.04
B-10b	4	0.90
B-11a	1	0.82
B-12	2	1.91
B-13	2	1.86
B-15	1	0.22
B-16	1	0.04

APPENDIX F Determination of Plastic Rotation Capacity

The plastic rotation capacity at different load levels was determined by the schematic illustration, see Figure F.1.

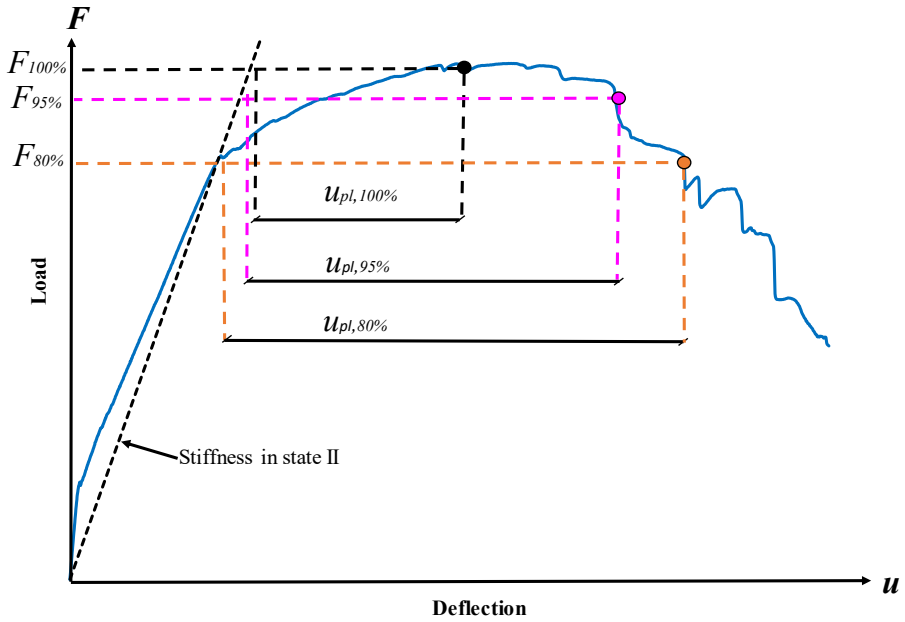

Figure F.1 *Schematic illustration of how the plastic rotation capacity for different load levels are determined.*

Table F.1 *Plastic deflections for different load levels for reference beams subjected to 3-point bending and 4-point bending test.*

Beam	Loading condition	$u_{pl,100\%}$ [mm]	$u_{pl,95\%}$ [mm]	$u_{pl,90\%}$ [mm]	$u_{pl,85\%}$ [mm]	$u_{pl,80\%}$ [mm]
B-02	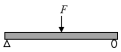	13	18	20	21	22
B-04		29	40	51	53	78
B-06		29	42	43	46	53
B-01	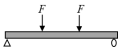	13	16	17	20	20
B-03		46	47	49	57	63
B-05		32	36	38	51	56

APPENDIX G Determination of Stiffness

The stiffness was evaluated in different stages: state I k_I and state II k_{II}, and determined by schematically illustration in Figure G.1 and Figure G.2. The calculations are based on the load-deflection relation for all beams tested statically. The stiffness in different stages are calculated as the ratio between the difference in load ΔF and difference in deflection Δu, see Equation (G.1).

$$k_i = \frac{\Delta F}{\Delta u} \tag{G.1}$$

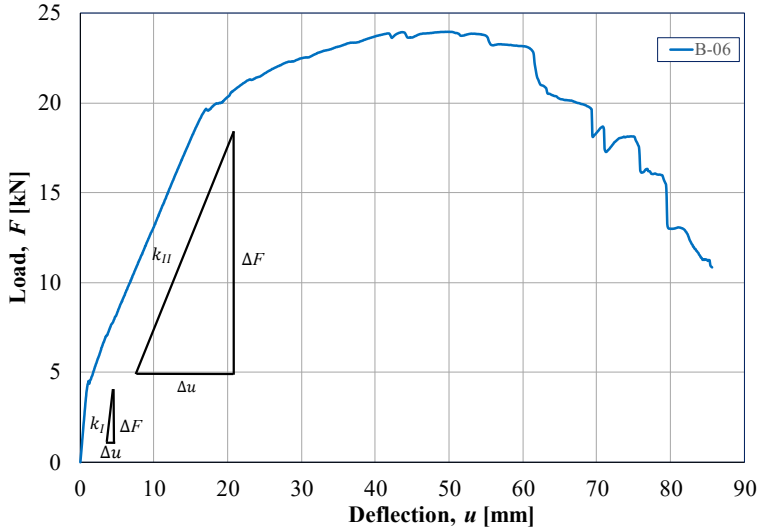

Figure G.1 The calculation procedure for stiffness in k_I and k_{II}.

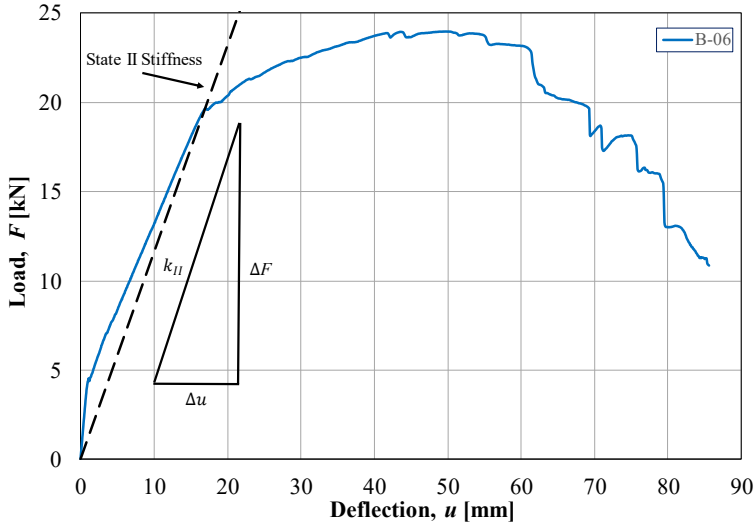

Figure G.2 The calculation procedure for stiffness in k_{II}.

APPENDIX H Internal Work Calculation

The internal work is calculated as the area under the load-deflection curve, see Figure H.1 and Figure H.2. The graphical procedure, which was used to calculate the internal work, was to first find the different load-levels which started at the maximum load $F_{100\%}$, and then decreased with 5 % intervals down to $F_{80\%}$. The area under the curve was divided into an elastic part marked in blue and plastic part marked in yellow.

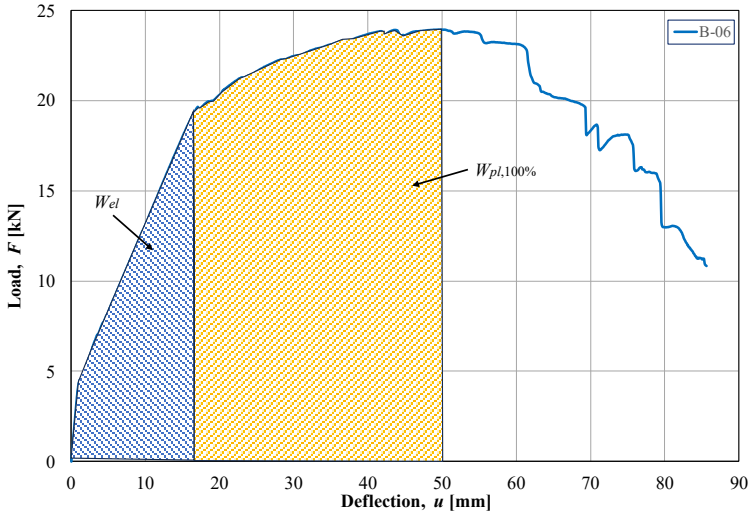

Plastic internal work level 100 %

Figure H.1 Schematic illustration of the calculation procedure for internal work of level 100 %.

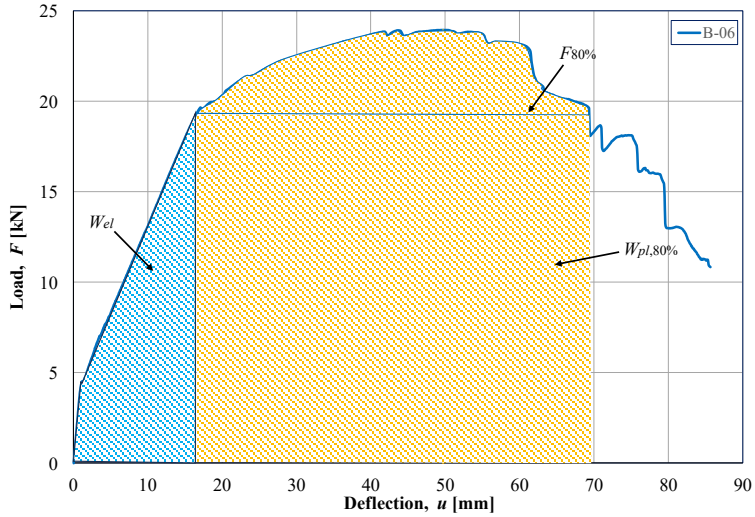

Plastic internal work level 80 %

Figure H.2 Schematic illustration of the calculation procedure for internal work of level 80 %.

APPENDIX I Strains Fields

The strains fields result for beams tested dynamically are presented in this section. It is to be noted that there are some strain fields results missing due errors occurred in the experiment.

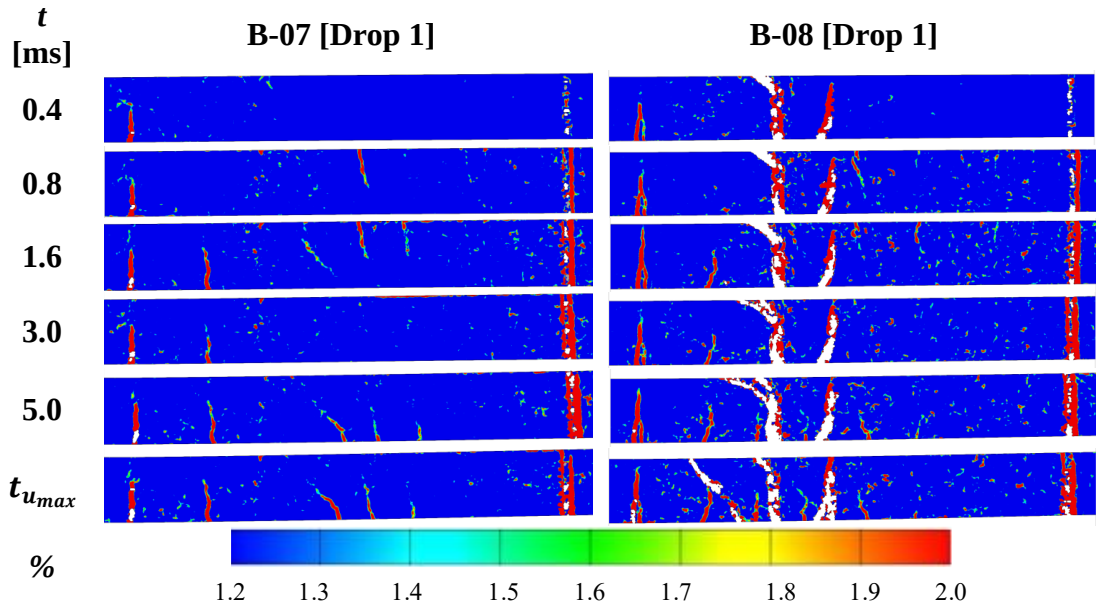

Figure I.1 *The strain fields for different time intervals for beams of reinforcement diameter 6 mm and drop-weight of 10 kg after first impact.*

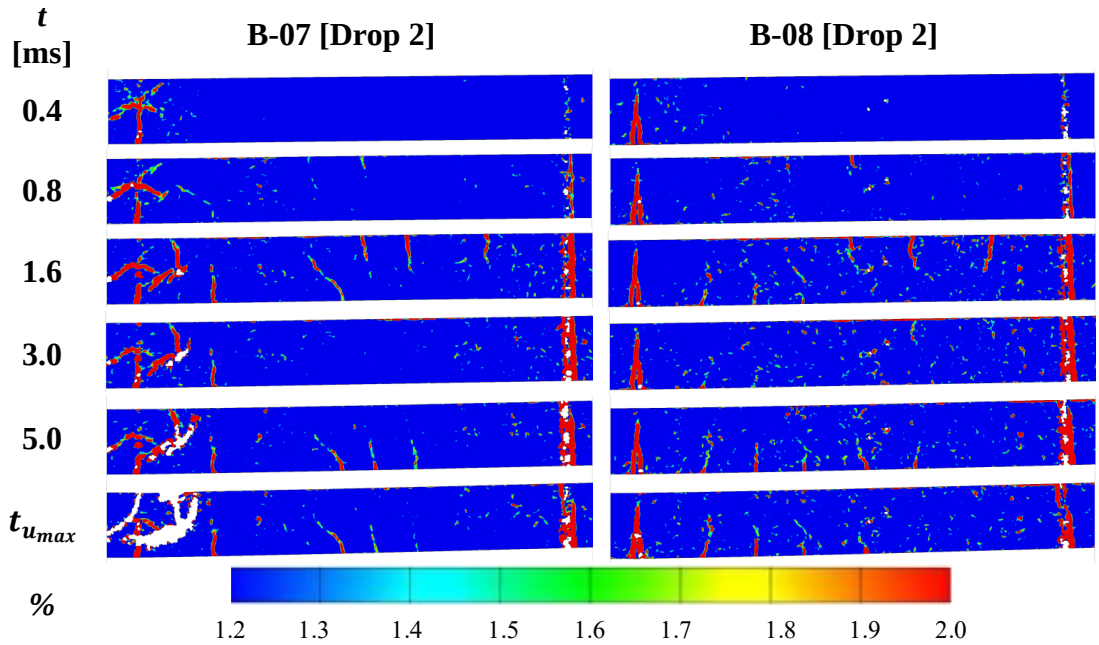

Figure I.2 *The strain fields for different time intervals for beams of reinforcement diameter 6 mm and drop-weight of 10 kg after second impact.*

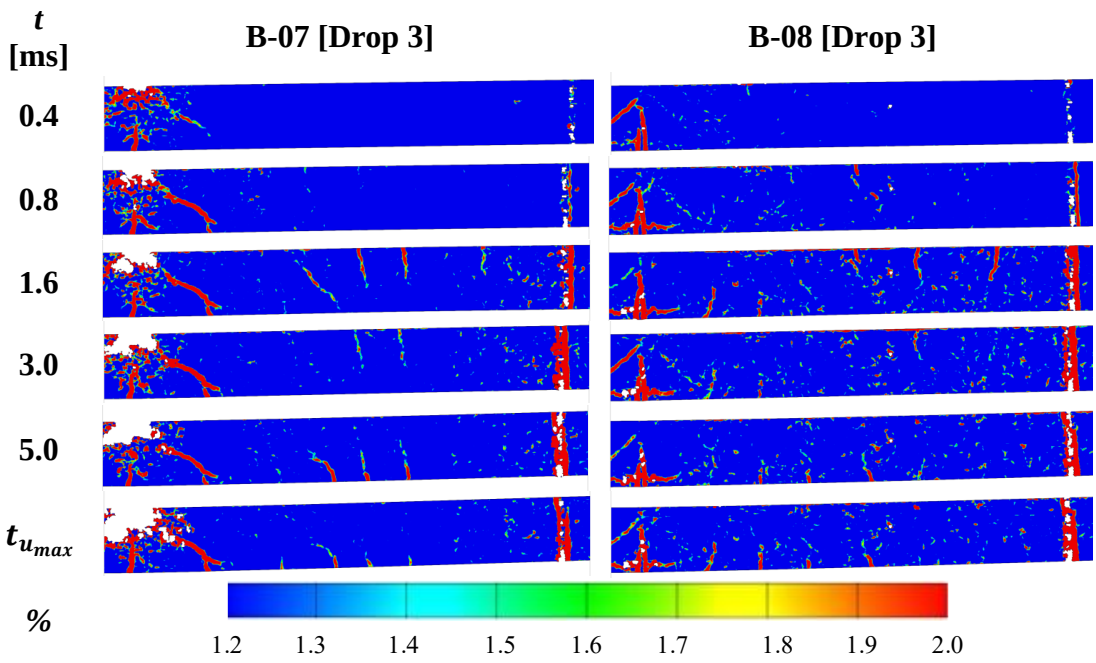

Figure I.3 *The strain fields for different time intervals for beams of reinforcement diameter 6 mm and drop-weight of 10 kg after third impact.*

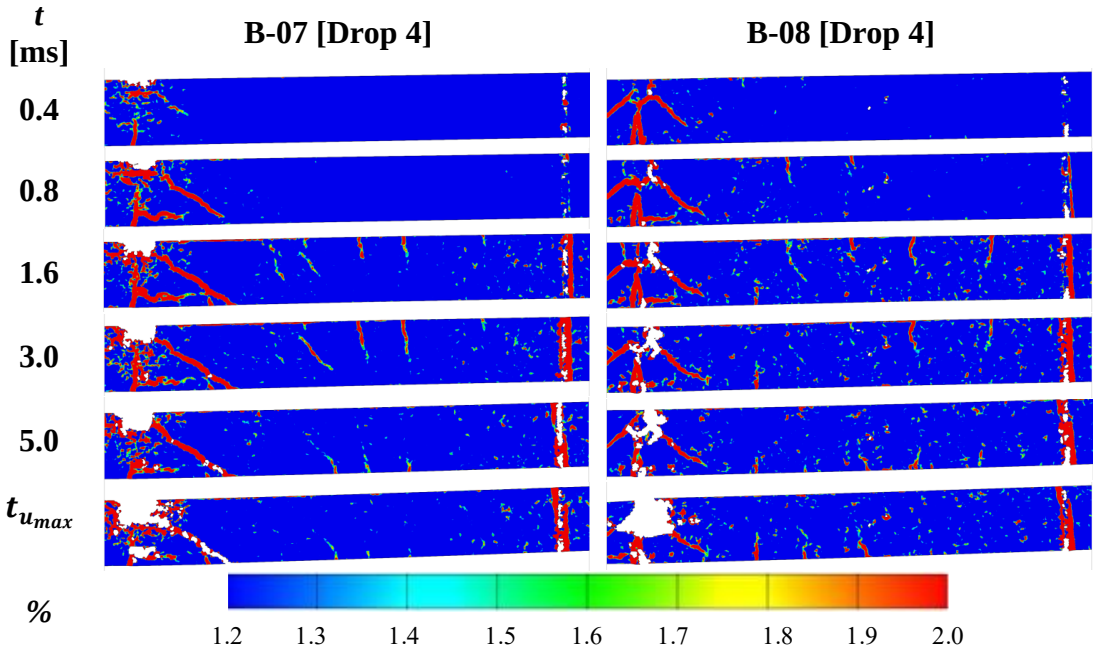

Figure I.4 *The strain fields for different time intervals for beams of reinforcement diameter 6 mm and drop-weight of 10 kg after fourth impact.*

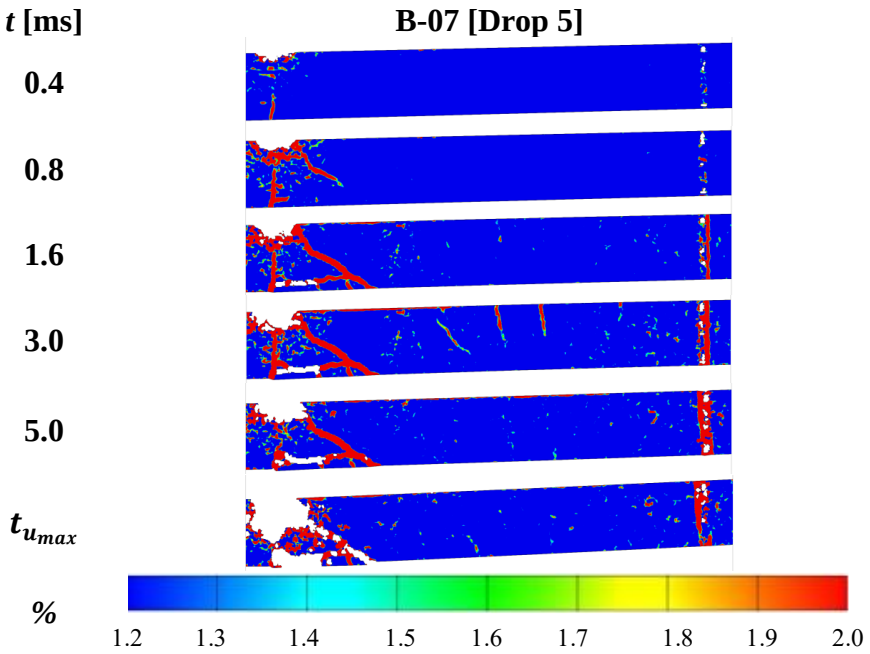

Figure I.5 *The strain fields for different time intervals for beams of reinforcement diameter 6 mm and drop-weight of 10 kg after fifth impact.*

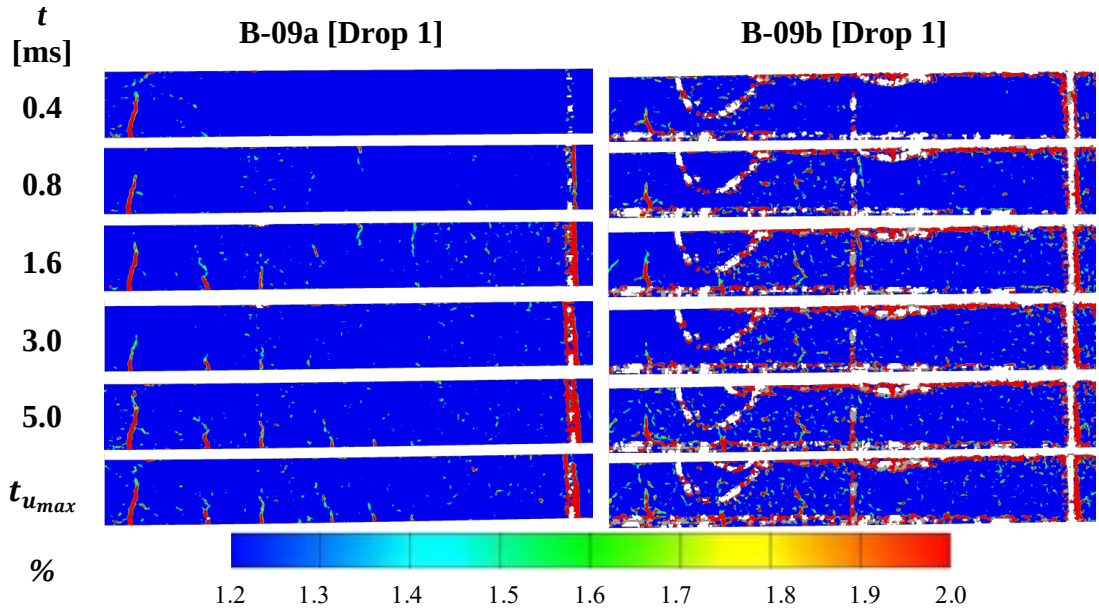

Figure I.6 *The strain fields for different time intervals for beams of reinforcement diameter 8 mm and drop-weight of 10 kg after first impact.*

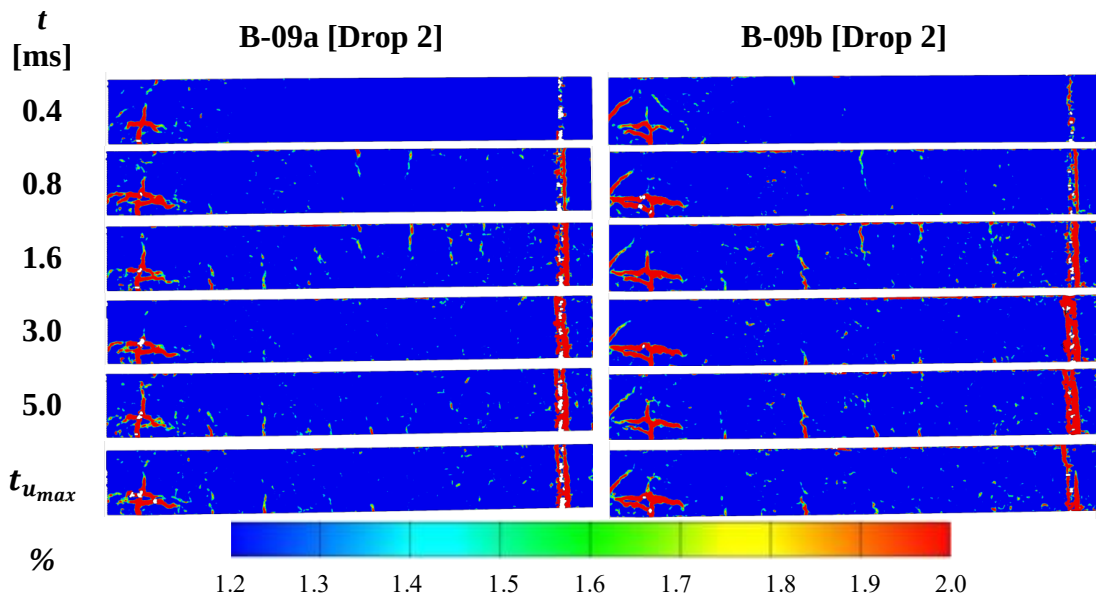

Figure I.7 *The strain fields for different time intervals for beams of reinforcement diameter 8 mm and drop-weight of 10 kg after second impact.*

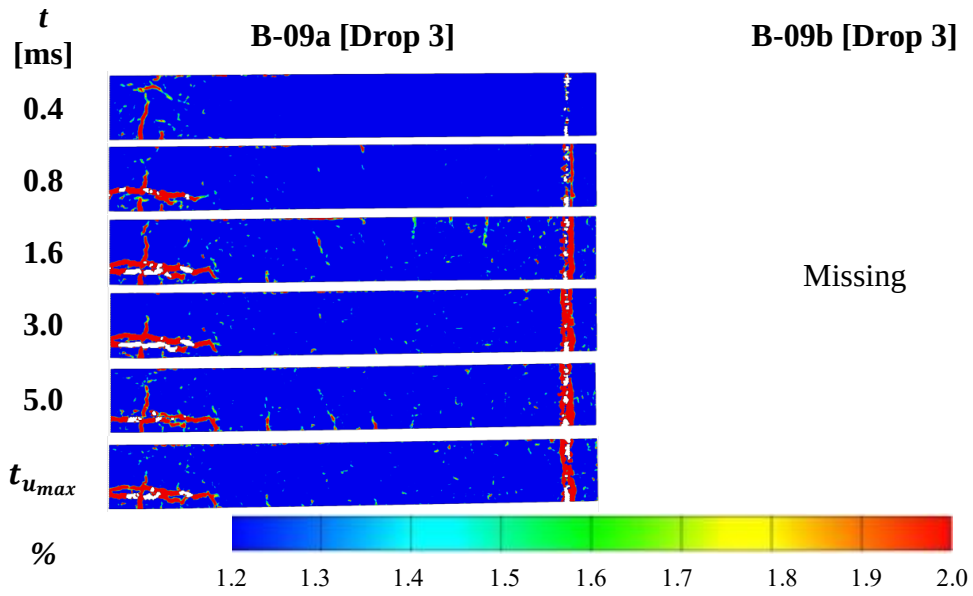

Figure I.8 *The strain fields for different time intervals for beams of reinforcement diameter 8 mm and drop-weight of 10 kg after third impact.*

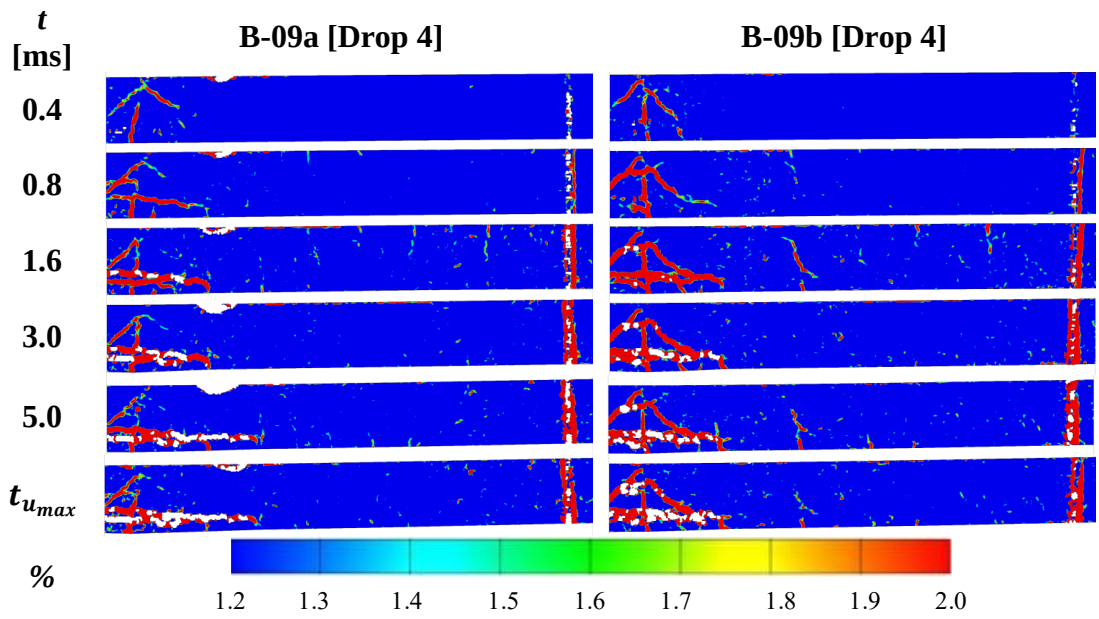

Figure I.9 *The strain fields for different time intervals for beams of reinforcement diameter 8 mm and drop-weight of 10 kg after fourth impact.*

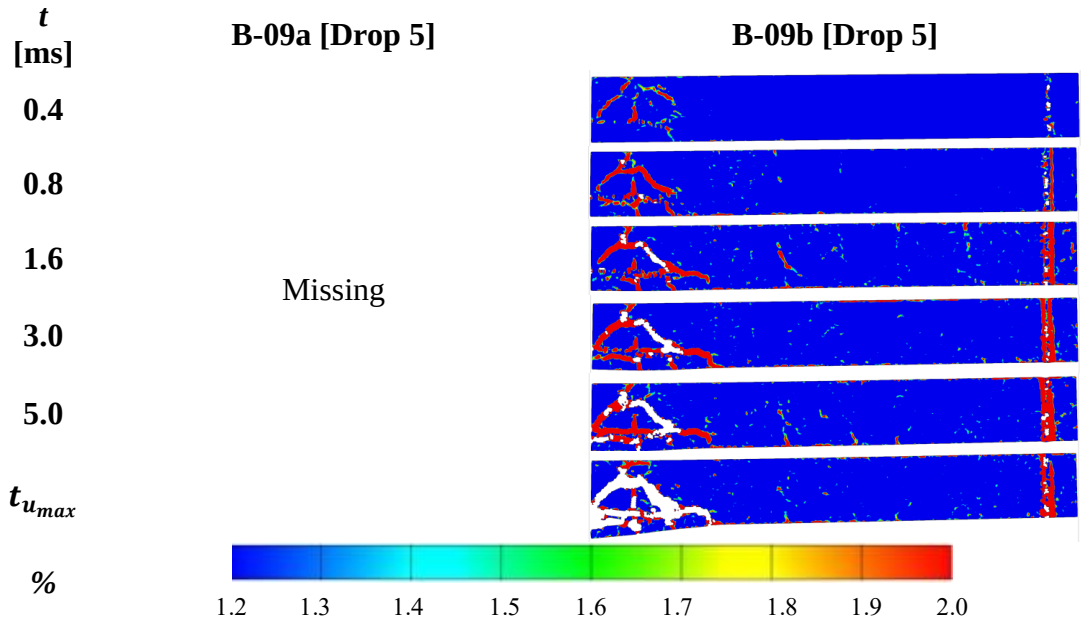

Figure I.10 *The strain fields for different time intervals for beams of reinforcement diameter 8 mm and drop-weight of 10 kg after fifth impact.*

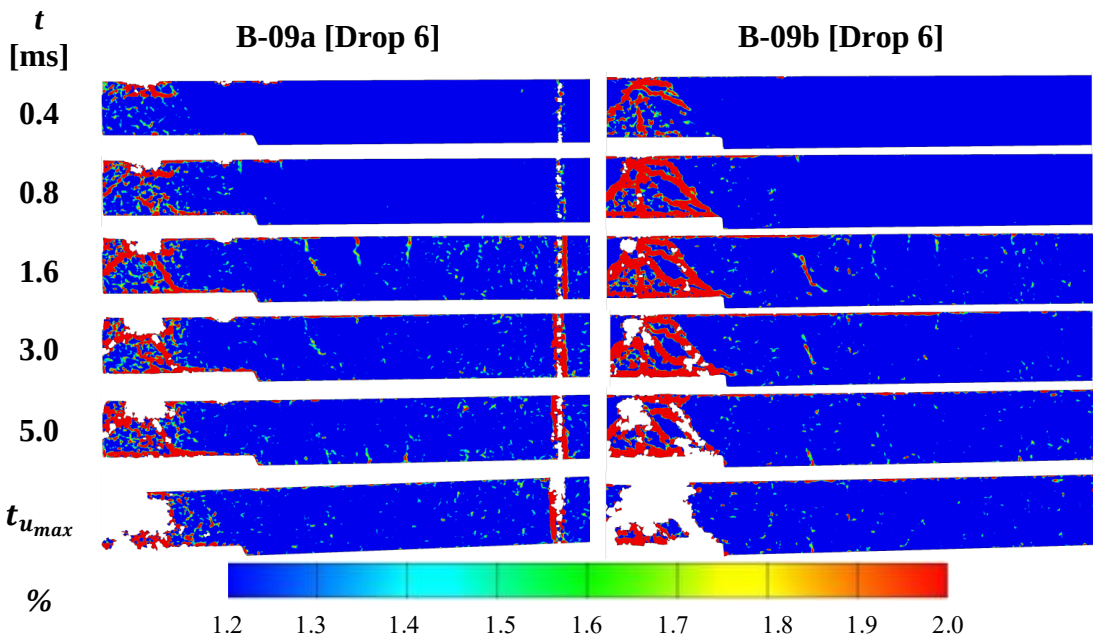

Figure I.11 *The strain fields for different time intervals for beams of reinforcement diameter 8 mm and drop-weight of 10 kg after sixth impact.*

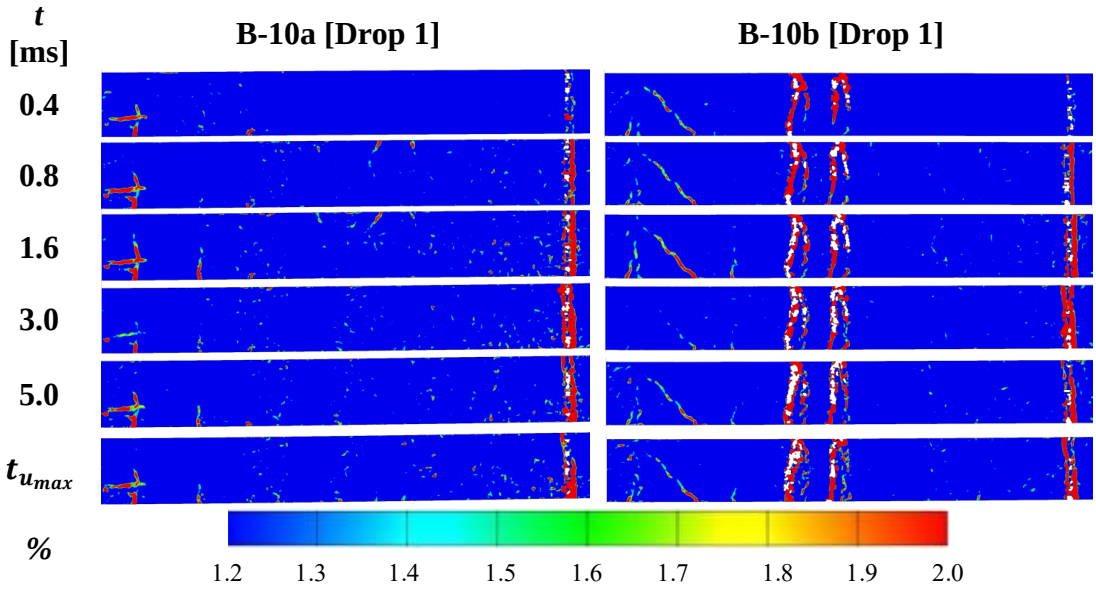

Figure I.12 *The strain fields for different time intervals for beams of reinforcement diameter 10 mm and drop-weight of 10 kg after first impact.*

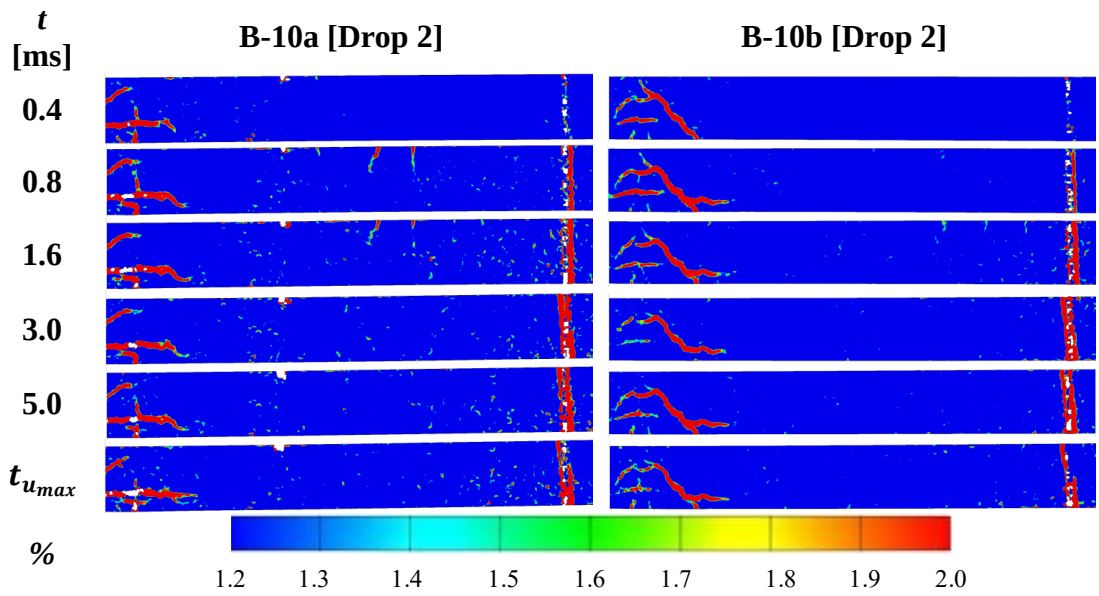

Figure I.13 *The strain fields for different time intervals for beams of reinforcement diameter 10 mm and drop-weight of 10 kg after second impact.*

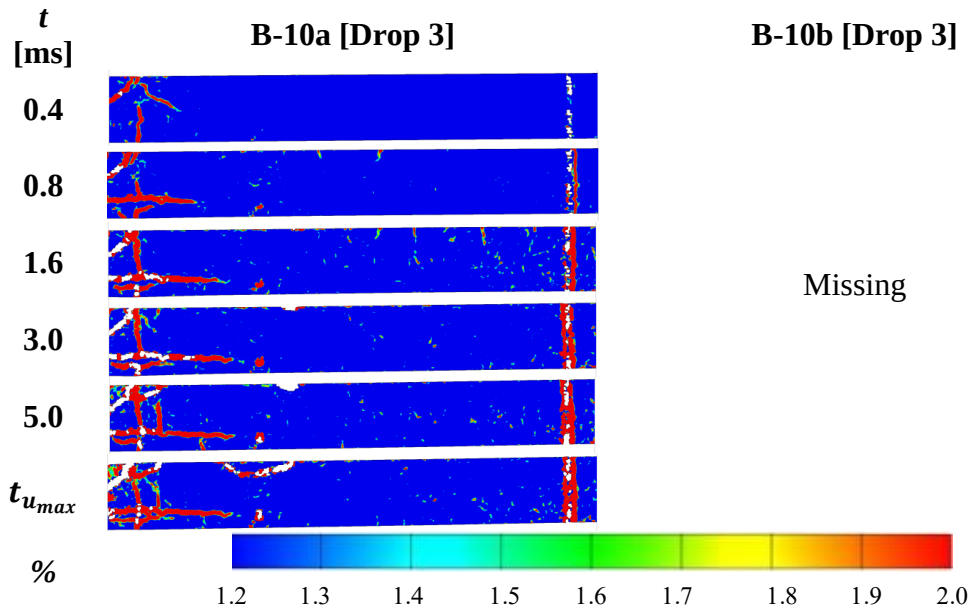

Figure I.14 *The strain fields for different time intervals for beams of reinforcement diameter 10 mm and drop-weight of 10 kg after third impact.*

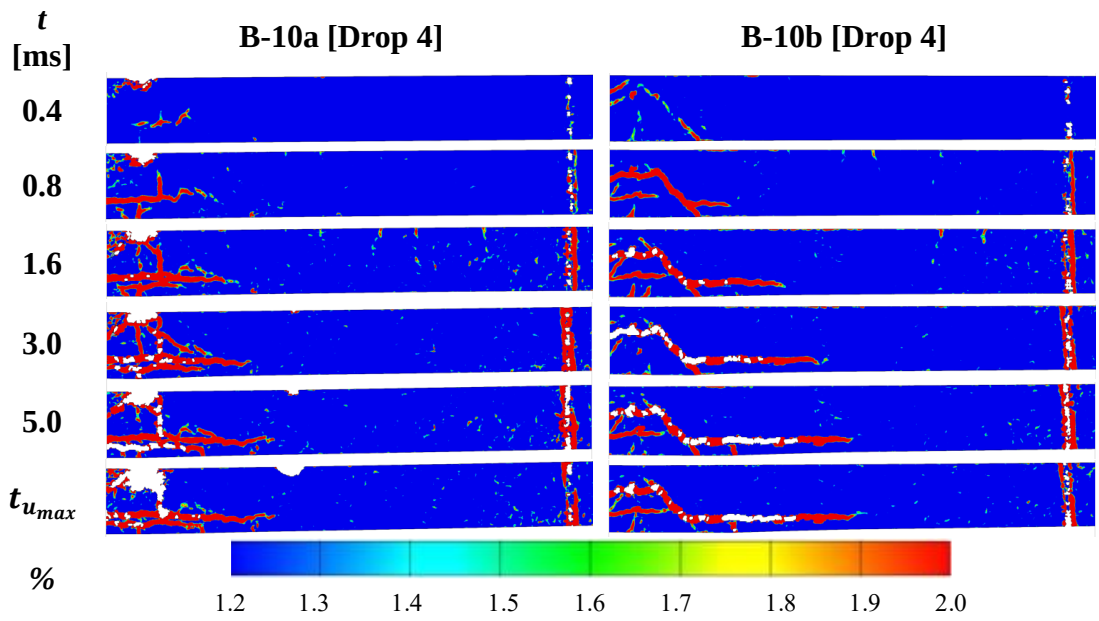

Figure I.15 *The strain fields for different time intervals for beams of reinforcement diameter 10 mm and drop-weight of 10 kg after fourth impact.*

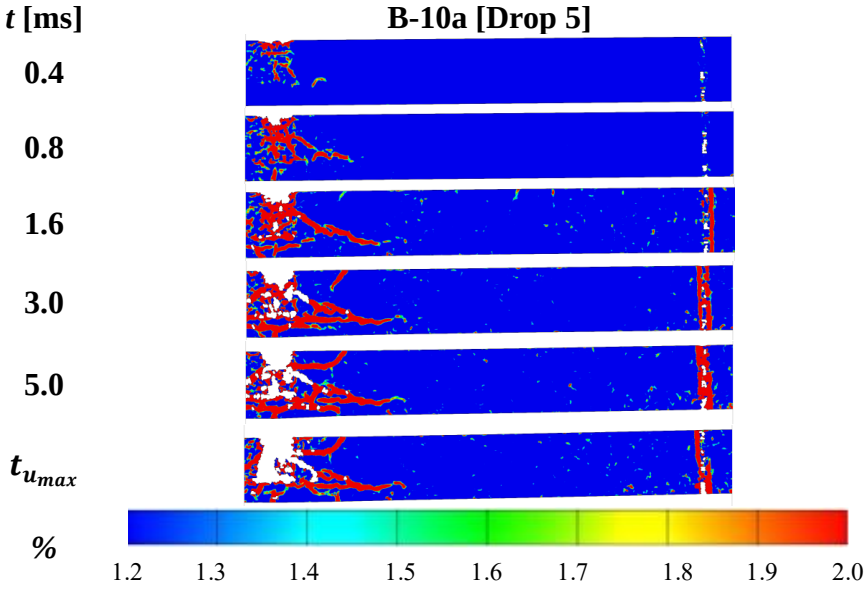

Figure I.16 *The strain fields for different time intervals for beams of reinforcement diameter 10 mm and drop-weight of 10 kg after fifth impact.*

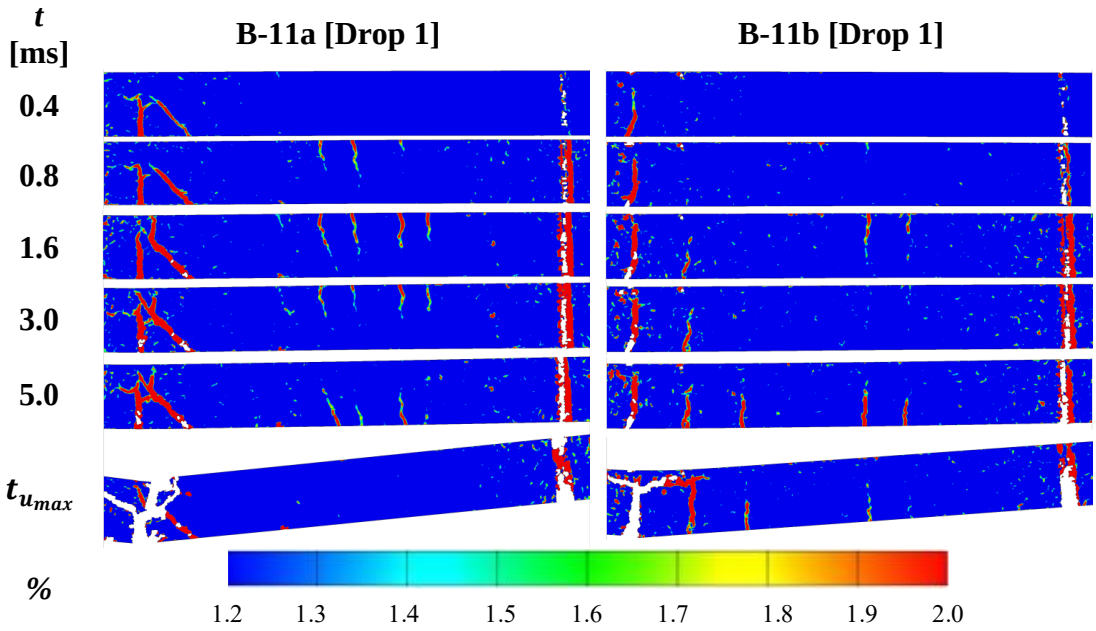

Figure I.17 *The strain fields for different time intervals for beams of reinforcement diameter 6 mm and drop-weight of 20 kg after first impact.*

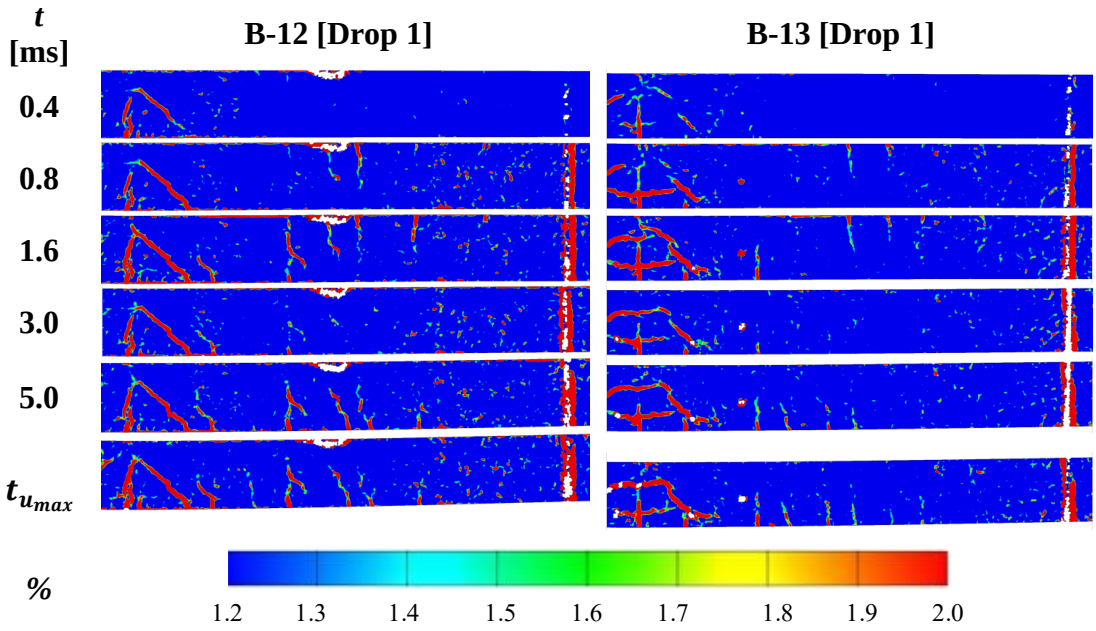

Figure I.18 *The strain fields for different time intervals for beams of reinforcement diameter 8 mm and 10 mm and drop-weight of 20 kg after first impact.*

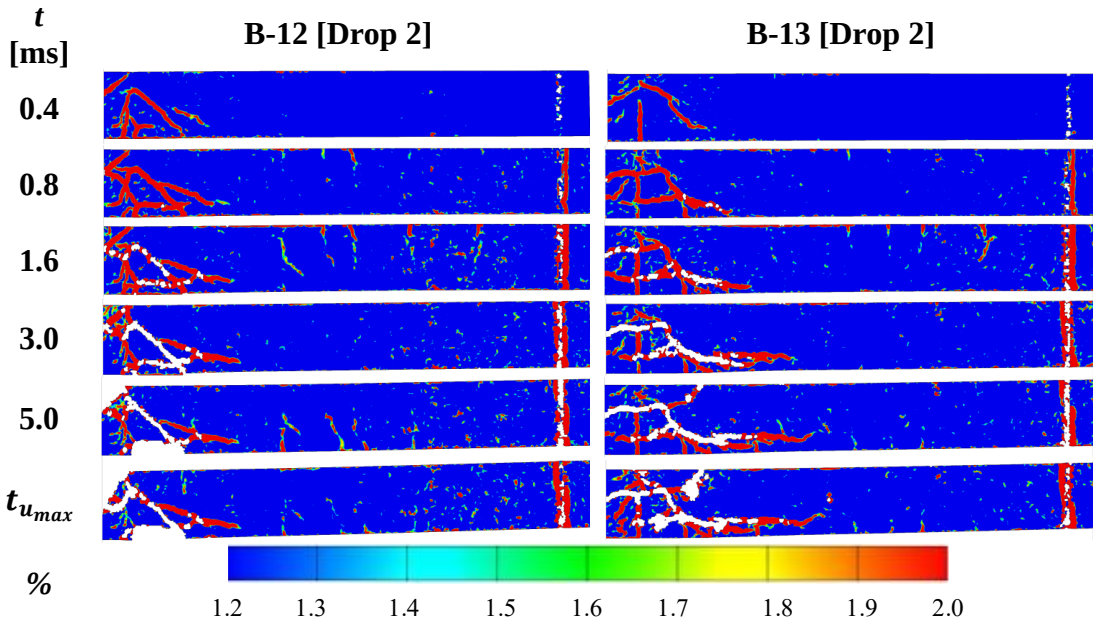

Figure I.19 *The strain fields for different time intervals for beams of reinforcement diameter 8 mm and 10 mm and drop-weight of 20 kg after second impact.*

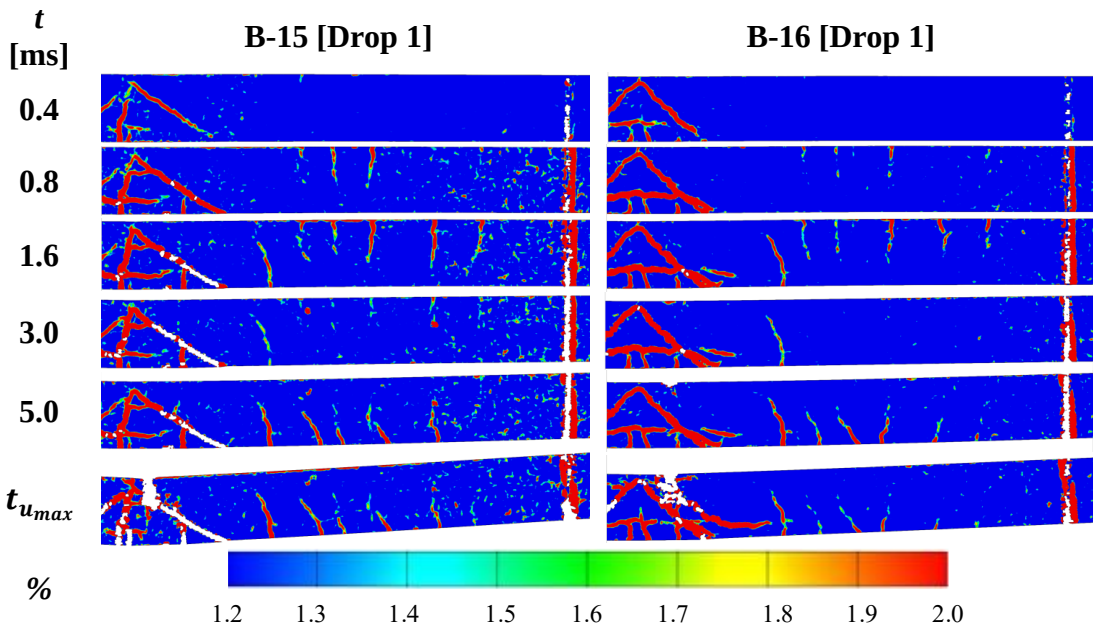

Figure I.20 *The strain fields for different time intervals for beams of reinforcement diameter 8 mm and 10 mm and drop-weight of 40 kg after first impact.*

APPENDIX J Pictures of Dynamically Tested Beams

In this section pictures of dynamically tested beams were taken after each impact of either the whole, half or middle of the beam depending on what produced the best visual result.

Impact	B-07	Beam part
0	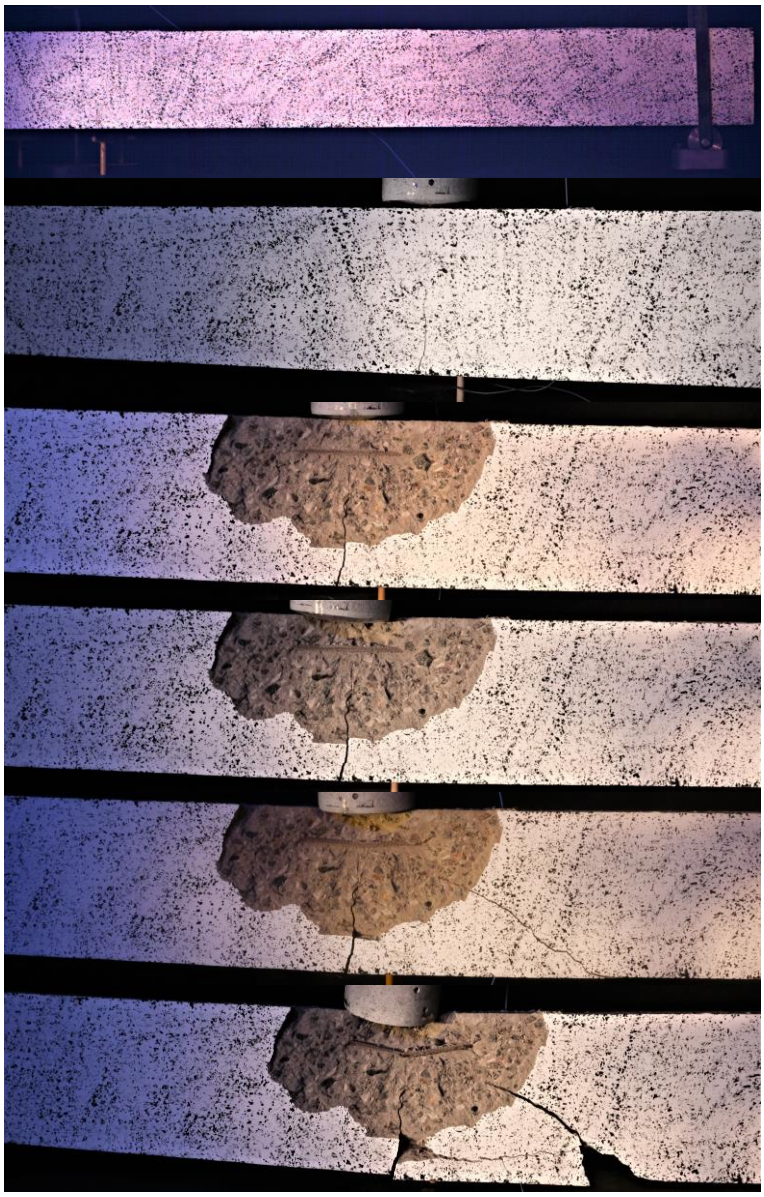	Half
1		Middle
2		Middle
3		Middle
4		Middle
5		Middle

Figure J.1 Images of beam B-07 after repeated impact loading.

Impact	B-08	Beam part
0	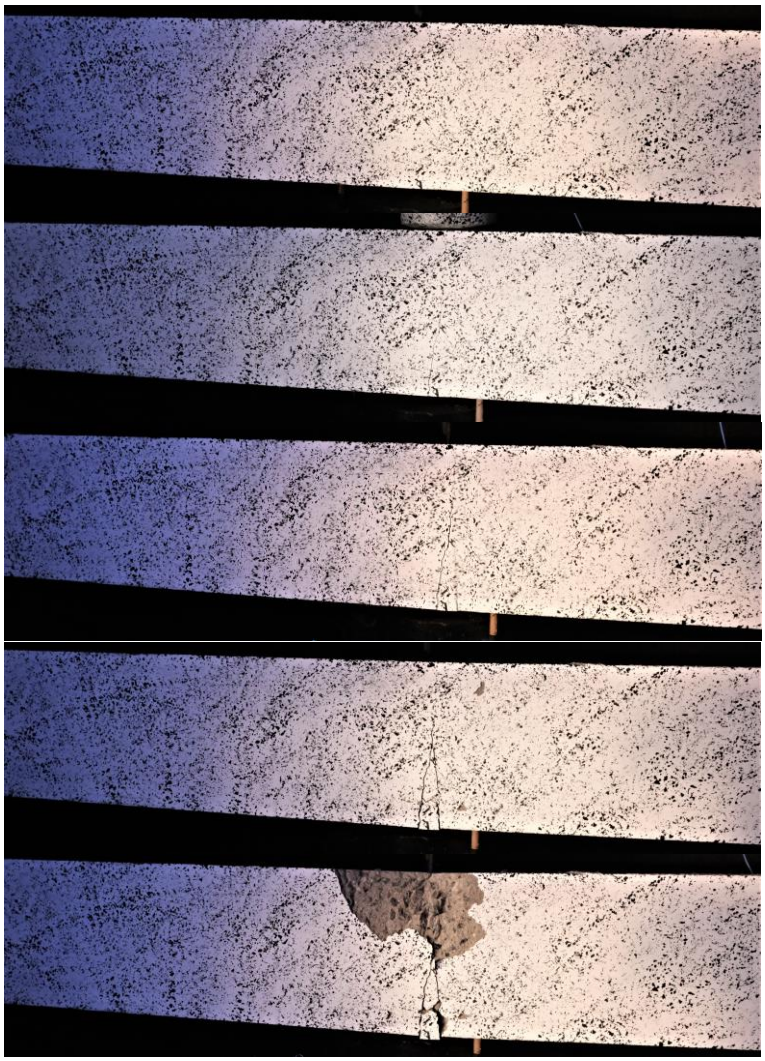	Middle
1		Middle
2		Middle
3		Middle
4		Middle

Figure J.2 Images of beam B-08 after repeated impact loading.

Impact	B-09a	Beam part
0		Middle
1		Middle
2		Middle
3		Middle
4		Middle
5		Middle
6		Middle

Figure J.3 Images of beam B-09a after repeated impact loading.

Drops	B-09b	Beam part
0	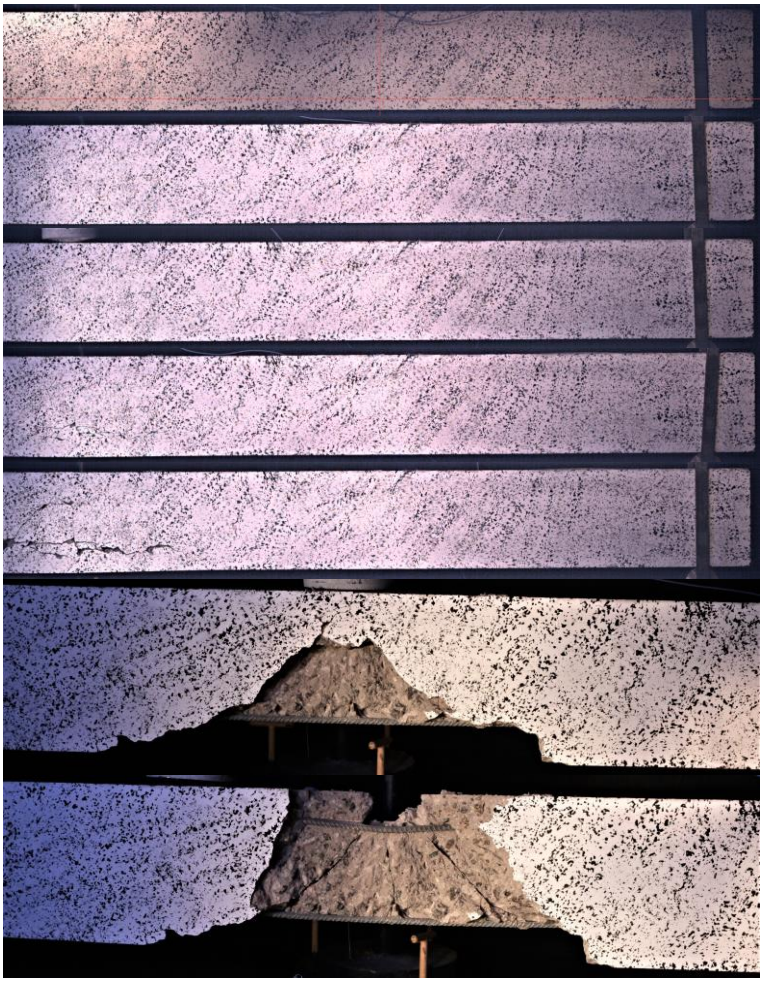	Half
1		Half
2		Half
3		Half
4		Half
5		Middle
6		Middle

Figure J.4 Images of beam B-09b after repeated impact loading.

Drops	B-10a	Beam part
0		Half
1		Middle
2		Middle
3		Middle
4		Middle
5		Middle

Figure J.5 Images of beam B-10a after repeated impact loading.

Drops	B-10b	Beam part
0		Middle
1		Middle
2		Middle
3		Middle
4		Middle

Figure J.6 Images of beam B-10b after repeated impact loading.

Drops	B-11a	Beam part
0	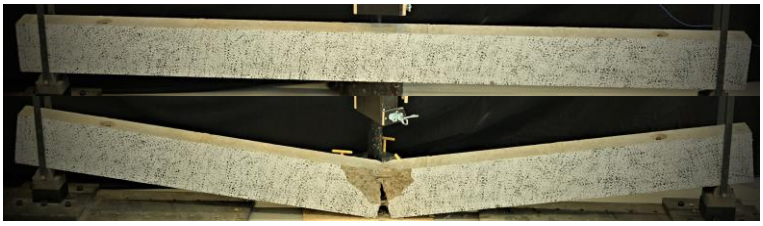	Whole
1		Whole

Figure J.7 Images of beam B-11a after repeated impact loading.

Drops	B-11b	Beam part
0		Whole
1		Whole

Figure J.8 Images of beam B-11b after repeated impact loading.

Drops	B-12	Beam part
0	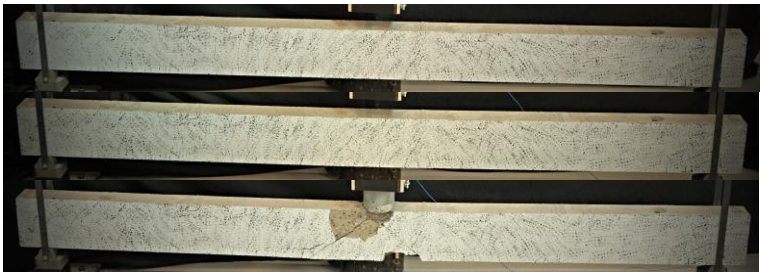	Whole
1		Whole
2		Whole

Figure J.9 Images of beam B-12 after repeated impact loading.

Drops	B-13	Beam part
0		Whole
1		Whole
2		Whole

Figure J.10 Images of beam B-13 after repeated impact loading.

Drops	B-15	Beam part
0		Whole
1		Whole

Figure J.11 Images of beam B-15 after repeated impact loading.

Drops	B-16	Beam part
0		Whole
1		Whole

Figure J.12 Images of beam B-16 after repeated impact loading.

APPENDIX K Pictures of Statically Tested Beams

For the statically tested beams images were taken before and after the tests.

B-02

Before

After

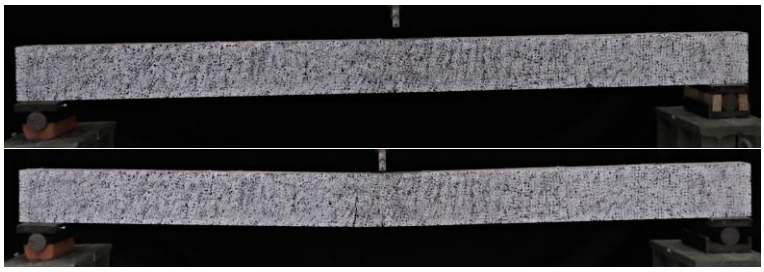

Figure K.1 Images of beam B-02 before and after static loading.

B-04

Before

After

Figure K.2 Images of beam B-04 before and after static loading.

B-06

Before

After

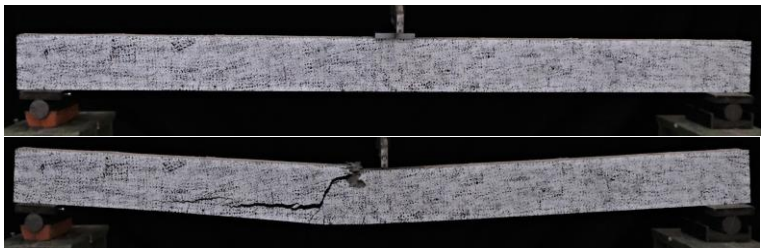

Figure K.3 Images of beam B-06 before and after static loading.

B-01

Before Missing

After

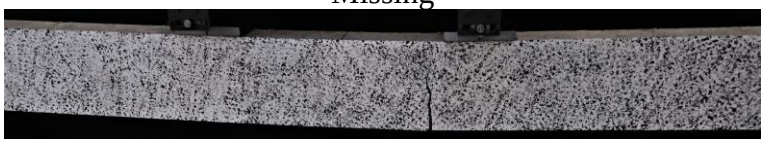

Figure K.4 Images of beam B-01 before and after static loading.

B-03

Before

After

Figure K.5 Images of beam B-03 before and after static loading.

B-05

Before

After

Figure K.6 Images of beam B-05 before and after static loading.

APPENDIX L Picture of Dynamically Tested Beams after Subsequently Static Testing

Images of dynamically tested beams followed by subsequent static test are presented in this section.

B-08

Before

After

Figure L.1 Images of beam B-08 before and after static loading.

B-10b

Before

After

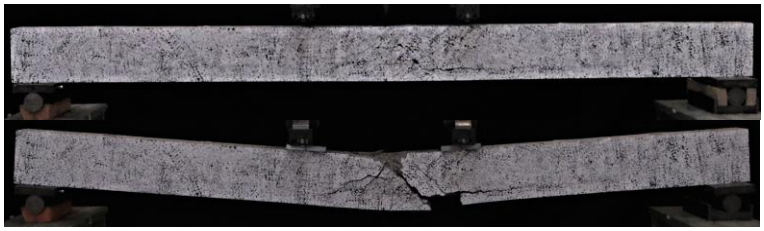

Figure L.2 Images of beam B-10b before and after static loading.

B-12

Before

After

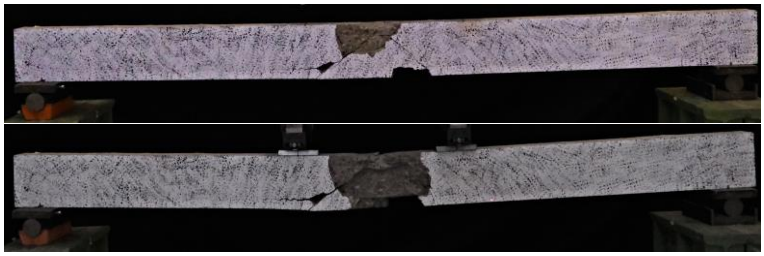

Figure L.3 Images of beam B-12 before and after static loading.

B-13

Before

After

Figure L.4 Images of beam B-13 before and after static loading.

B-15

Before

After

Figure L.5 Images of beam B-15 before and after static loading.

B-16

Before

After

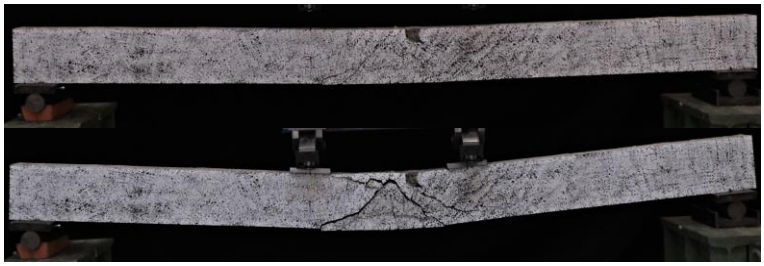

Figure L.6 Images of beam B-16 before and after static loading.

Appendix M Mathcad Calculations

Calculations for predicted response

Load Capacity of Reinforced Concrete Beam

Based on the calculation from FABIO MENDOZA and JOSEF APHRAM

Input data

Geometry

Beam height: $h := 0.2\ m$

Beam width: $b := 0.1\ m$

Cross-section area: $A_c := b \cdot h = 0.02\ m^2$

Distance for applied load for 3- and 4-point bending : $l_0 := 1.3\ m$, $L_F := 1\ m$

Effective span length: $L := 2.6\ m$

bar diameter: $\phi := 6\ mm$

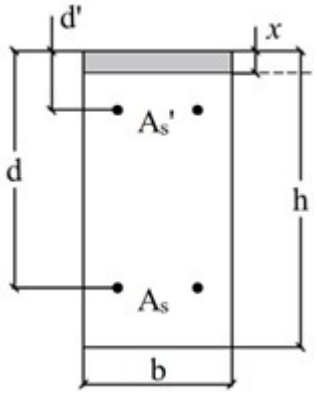

Density of reinforced concrete: $\rho := 2500 \cdot \frac{kg}{m^3}$

Self-weight $g_1 := g \cdot \rho \cdot A_c = 0.49\ \frac{kN}{m}$

Area of reinforcement bar: $A_{bar} := \pi \cdot \frac{\phi^2}{4} = 28.27\ mm^2$

Number of bars in the top: $n' := 2$

Number of bars in the bottom: $n := 2$

Area of top reinforcement: $A'_s := n' \cdot A_{bar} = 56.55\ mm^2$

Area of bottom reinforcement: $A_s := n \cdot A_{bar} = 56.55\ mm^2$

Concrete cover: $c := 0.040\ m - \frac{\phi}{2} = 37\ mm$

Position of top reinforcement from top edge: $d' := \left(\frac{\phi}{2} + c\right) = 40\ mm$

Position of bottom reinforcement from top edge: $d := h - \left(\frac{\phi}{2} + c\right) = 160\ mm$

Material properties

Concrete C40/50 at 28 days:

Mean compressive strength: $f_{cm} := 55.01\ MPa$

Mean tensile strength: $f_{ctm} := 3.91\ MPa$

Mean modulus of elasticity: $E_{cm} := 36.69\ GPa$

Steel:

Mean yield strength: $f_{ym} := 546\ MPa$

Ultimate tensile strength: $f_u := 588\ MPa$

Mean modulus of elasticity: $E_{sm} := 200\ GPa$

Stress-strain relationship of concrete

Parameters for concrete classes
Concrete strain at maximum strength:

Ultimate concrete strain: $\varepsilon_{c2} := 0.002$

$\varepsilon_{cu2} := 0.003005$

Exponent used in concrete stress-function: $n_{¤} := 2$

Strain-vector used in concrete stress-function: $\varepsilon_c := 0, 0.0001 .. \varepsilon_{cu2}$

Stress-strain relationship:

Stress-strain relationship for concrete

$$\sigma_c(\varepsilon_c) := \begin{cases} \left(1 - \left(1 - \frac{\varepsilon_c}{\varepsilon_{c2}}\right)^{n_{¤}}\right) \cdot f_{cm} & \text{if } 0 \le \varepsilon_c \le \varepsilon_{c2} \\ f_{cm} & \text{else if } \varepsilon_{c2} \le \varepsilon_c \le \varepsilon_{cu2} \end{cases}$$

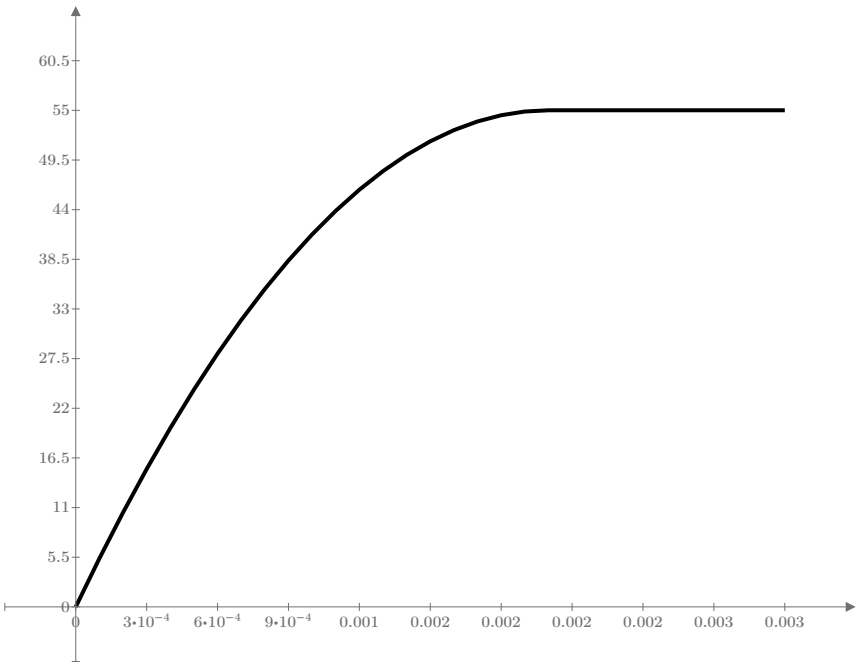

$\sigma_c(\varepsilon_c)$ (*MPa*)

ε_c

Determination of block factors

Area under the curve for a given value of strain:

$$Area(\varepsilon_c) := \int_0^{\varepsilon_c} \sigma_c(\varepsilon_c)\, d\varepsilon_c$$

Area under the curve multiplied by the distance from the origin to the center of gravity of area:

$$A_\varepsilon(\varepsilon_c) := \int_0^{\varepsilon_c} \sigma_c(\varepsilon_c) \cdot \varepsilon_c\, d\varepsilon_c$$

Determination of factors αR.S and βR.S

$$\alpha_{R.S}(\varepsilon_c) := \frac{Area(\varepsilon_c)}{f_{cm} \cdot \varepsilon_c} \qquad \beta_{R.S}(\varepsilon_c) := \frac{\varepsilon_c - \frac{A_\varepsilon(\varepsilon_c)}{Area(\varepsilon_c)}}{\varepsilon_c}$$

$$\alpha_{R.S}(\varepsilon_{cu2}) = 0.778 \qquad \beta_{R.S}(\varepsilon_{cu2}) = 0.405$$

Stress-strain relationship of reinforcing steel

Ultimate steel strain: $\varepsilon_{su} := 0.029$ Yield strain: $\varepsilon_{sy} := \frac{f_{ym}}{E_{sm}} = 2.73 \cdot 10^{-3}$

Relationship parameters: $\rho_1(\varepsilon_s) := \frac{\varepsilon_s - \varepsilon_{sy}}{\varepsilon_{su} - \varepsilon_{sy}}$ Steel strain vector: $\varepsilon_s := 0, 0.001 .. \varepsilon_{su}$

Stress-strain relationship:

$$\sigma_s(\varepsilon_s) := \begin{cases} E_{sm} \cdot \varepsilon_s & \text{if } \varepsilon_s \le \varepsilon_{sy} \\ f_{ym} + \rho_1(\varepsilon_s) \cdot (f_u - f_{ym}) & \text{else if } \varepsilon_{sy} \le \varepsilon_s \end{cases}$$

Graphic representation of the stress-strain relationship for reinforcing steel:

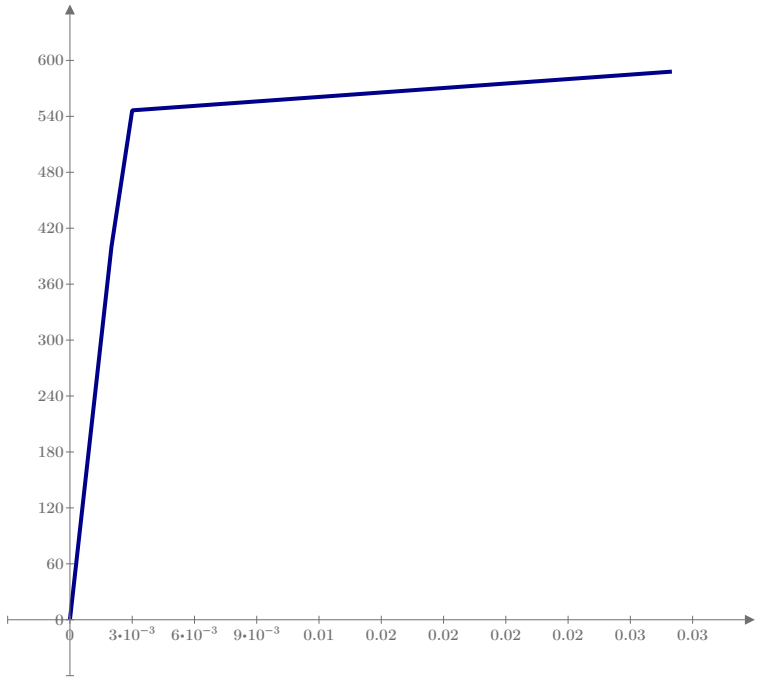

Design Strength Values

Concrete

Partial factor: $\gamma_c := 1.0$ Design compressive strength: $f_{cd} := \frac{f_{cm}}{\gamma_c} = 55.01$ **MPa**

Concrete ultimate strain: $\varepsilon_{cu} := 0.003006$

Stress block factors: $\alpha_R := \alpha_{R.S}(\varepsilon_{cu2}) = 0.778$ $\beta_R := \beta_{R.S}(\varepsilon_{cu2}) = 0.4$

5%-fractile tensile strength: $f_{ctk0.05} := 0.7 \cdot f_{ctm} = 2.74$ **MPa**

Flexural tensile strength: $f_{ct.fl} := \kappa \cdot f_{ctm} = 4.68$ **MPa**

$$\kappa := 0.6 + \frac{0.4}{\sqrt[4]{\frac{h}{m}}} = 1.2$$

Reinforcing steel:

Partial factor: $\gamma_s := 1.0$ Design yield stress: $f_{yd} := \frac{f_{ym}}{\gamma_s} = 546$ **MPa**

Load Capacity in Ultimate Limit State

Analysis of field section without top reinforcement

Number of bars in the top: $n_1' := 0$ Number of bars in the bottom: $n_1 := 2$

Assume yielding: $\varepsilon_{s.1} > \varepsilon_{sy}$ $\varepsilon_{s.1} := \frac{d - x_1}{x_1} \varepsilon_{cu}$

Position of neutral axis:

Initial assumption: $x_1 := 0.01 \cdot m$

Calculated value:

$$x_1 := \mathbf{root}\left(\alpha_R \cdot f_{cd} \cdot b \cdot x_1 - \sigma_s\left(\frac{(d - x_1)}{x_1} \cdot \varepsilon_{cu}\right) \cdot n_1 \cdot A_{bar}, x_1\right)$$

$x_1 = 8.31\ mm$

Check the strain in the reinforcement bars:

$$\varepsilon_{s.1} := \frac{d - x_1}{x_1} \cdot \varepsilon_{cu} = 0.05485 \quad > \quad \varepsilon_{sy} = 2.73 \cdot 10^{-3}$$

Calculation of load capacity:

$$M_{u.1} := \alpha_R \cdot f_{cd} \cdot b \cdot x_1 \cdot (d - \beta_R \cdot x_1) = 5.57\ kN \cdot m$$

$$M_g := \frac{g_1 \cdot L^2}{8} = 0.41\ kN \cdot m$$

$$M_{u.1.red} := M_{u.1} - M_g = 5.16\ kN \cdot m$$

$$F_{u.3.without} := \frac{4 \cdot M_{u.1.red}}{L} = 7.94\ kN$$

Ultimate load capacity for 3-point bending

$$F_{u.4.without} := \frac{M_{u.1.red}}{L_F} = 5.16\ kN$$

$$F_{u.4.without.tot} := 2 \cdot F_{u.4.without} = 10.32\ kN$$

Ultimate load capacity for 4-point bending

Calculation of stress in the steel bars:

$$\sigma_{s.1} := \sigma_s(\varepsilon_{s.1}) = 629.32\ MPa$$

Calculation of curvature at failure:

$$\varphi_{u.1} := \frac{\varepsilon_{s.1}}{d - x_1} = 0.36\ \frac{1}{m}$$

Analysis of field section including top reinforcement

Number of bars in the top: $n'_2 := 2$

Number of bars in the bottom: $n_2 := 2$

Strain in top reinforcement:

$$\varepsilon'_{s.2} := \frac{d' - x_2}{x_2} \cdot \varepsilon_{cu}$$

Strain in bottom reinforcement:

$$\varepsilon_{s.2} := \frac{d - x_2}{x_2} \cdot \varepsilon_{cu}$$

Position of neutral axis:

Initial assumption: $x_2 := 0.02 \cdot m$

Calculated value:

$$x_2 := \mathbf{root}\left(\alpha_R \cdot f_{cd} \cdot b \cdot x_2 - \sigma_s\left(\frac{d' - x_2}{x_2} \cdot \varepsilon_{cu}\right) \cdot n'_2 \cdot A_{bar} - \sigma_s\left(\frac{d - x_2}{x_2} \cdot \varepsilon_{cu}\right) \cdot n_2 \cdot A_{bar}, x_2\right)$$

$x_2 = 15.03\ mm$

The neutral axis is located above the top reinforcement. Top bars are subjected to tensile stress.

Check the strain in the reinforcement bars:

$$\varepsilon'_{s.2} := \frac{d' - x_2}{x_2} \cdot \varepsilon_{cu} = 4.99 \cdot 10^{-3} \quad > \quad \varepsilon_{sy} = 0.003$$

$$\varepsilon_{s.2} := \frac{d - x_2}{x_2} \cdot \varepsilon_{cu} = 0.029 \quad > \quad \varepsilon_{sy} = 0.003$$

Calculation of moment and load capacity:

$$M_{u.2} := \alpha_R \cdot f_{cd} \cdot b \cdot x_2 \cdot (d - \beta_R \cdot x_2) - \sigma_s\left(\frac{d' - x_2}{x_2} \cdot \varepsilon_{cu}\right) \cdot A'_s \cdot (d - d') = 6.17\ kN \cdot m$$

$$M_{u.2.red} := M_{u.2} - M_g = 5.76\ kN \cdot m$$

$$F_{u.3.with} := \frac{4 \cdot M_{u.2.red}}{L} = 8.86\ kN$$

Ultimate load capacity for 3-point bending

$$F_{u.4.with} := \frac{M_{u.2.red}}{L_F} = 5.76\ kN$$

$$F_{u.4.with.tot} := 2 \cdot F_{u.4.with} = 11.51\ kN$$

Ultimate load capacity for 4-point bending

Calculation of stress in the steel bars:

$$\sigma'_{s.2} := \sigma_s\left(\varepsilon'_{s.2}\right) = 549.62\ MPa$$

$$\sigma_{s.2} := \sigma_s\left(\varepsilon_{s.2}\right) = 588\ MPa$$

Calculation of curvature at failure:

$$\varphi_{u.2} := \frac{\varepsilon_{s.2}}{d - x_2} = 0.2\ \frac{1}{m}$$

Moment and Curvature at Onset of Yielding

Analysis of field section without top reinforcement

Yielding strain: $\varepsilon_{sy} = 2.73 \cdot 10^{-3}$

Definition of strain in the compressed edge: $\varepsilon_{cc.y.1} := \frac{x_{y.1}}{d - x_{y.1}} \cdot \varepsilon_{sy}$

Tensile force in the bottom reinforcement: $F_{sy} := f_{yd} \cdot n \cdot A_{bar} = 30.88\ kN$

Equivalent compressive force in concrete: $F_{c.y.1} := \alpha_{R.y} \cdot f_{yd} \cdot b \cdot x_{y.1}$

$\alpha_{R.y} := \alpha_{R.S}\left(\varepsilon_{cc.y.1}\right)$

Horizontal equilibrium condition:

$F_{sy} \quad = \quad F_{c.y.1}$

Assume: $x_{y.1} := 24.635\ mm$ finding $x_{y.1}$ iterative

Total tensile force: $F_{sy} = 30.88\ kN$

Total compressive force: $F_{C.y.1} := \alpha_{R.S}\left(\frac{x_{y.1}}{d - x_{y.1}} \cdot \varepsilon_{sy}\right) \cdot f_{cd} \cdot b \cdot x_{y.1} = 30.88\ kN$

Check that ΔF=0:

Calculation of strains: $\Delta F := F_{C.y.1} - F_{sy} = \left(1.39 \cdot 10^{-3}\right)\ kN$ Close to = 0

$\varepsilon_{cc.y.1} := \frac{x_{y.1}}{d - x_{y.1}} \cdot \varepsilon_{sy} = 4.97 \cdot 10^{-4} \quad < \varepsilon_{c2} = 2 \cdot 10^{-3}$

Calculation of moment at yielding:

$\alpha_{R.y} := \alpha_{R.S}\left(\varepsilon_{cc.y.1}\right) = 0.23 \qquad \beta_{R.y} := \beta_{R.S}\left(\varepsilon_{cc.y.1}\right) = 0.34$

$M_{y.1} := \alpha_{R.y} \cdot f_{cd} \cdot b \cdot x_{y.1} \cdot \left(d - \beta_{R.y} \cdot x_{y.1}\right) = 4.68\ kN \cdot m$

$M_{y.1.red} := M_{y.1} - M_g = 4.27\ kN \cdot m$

$F_{y.3.without} := \frac{4 \cdot M_{y.1.red}}{L} = 6.56\ kN$

$F_{y.4.without} := \frac{M_{y.1.red}}{L_F} = 4.27\ kN$

$F_{y.4.without.tot} := 2 \cdot F_{y.4.without} = 8.53\ kN$

Determination of stresses in the reinforcement bars: $\sigma_{s.y.1} := \sigma_s\left(\varepsilon_{sy}\right) = 546\ MPa$

Curvature at yielding: $\varphi_{y.1} := \frac{\varepsilon_{sy}}{d - x_{y.1}} = 0.02\ \frac{1}{m}$

Analysis of field section including top reinforcement

Assume tension in the top reinforcement bars

Yielding strain: $\varepsilon_{sy} = 2.73 \cdot 10^{-3}$

Strain in the compressed edge and top reinforcement:

$$\varepsilon_{cc.y.2} := \frac{x_{y.2}}{d - x_{y.2}} \cdot \varepsilon_{sy} \qquad \varepsilon'_{cc.y.2} := \frac{d' - x_{y.2}}{d - x_{y.2}} \cdot \varepsilon_{sy}$$

Total tensile force in reinforcement :

Top reinforcement: $F'_{sy.2} := \sigma\left(\varepsilon'_{s.y.2}\right) \cdot A'_s$

Bottom reinforcement: $F_{sy} := f_{yd} \cdot A_s = 30.88\ \boldsymbol{kN}$

Equivalent compressive force in concrete:

$F_{c.y.2} := \alpha_{R.y} \cdot f_{yd} \cdot b \cdot x_{y.2}$ $\qquad \alpha_{R.y} := \alpha_{R.S}\left(\varepsilon_{cc.y.2}\right)$

Horizontal equilibrium condition:

$F'_{sy.2} + F_{sy} \quad = \quad F_{c.y.2}$

Assume: $x_{y.2} := 25.855\ \boldsymbol{mm}$ finding $x_{y.2}$ iterative

Total tensile force: $F_{T.y.2} := F_{sy} + \sigma_s\left(\frac{d' - x_{y.2}}{d - x_{y.2}} \cdot \varepsilon_{sy}\right) \cdot A'_s = 34.13\ \boldsymbol{kN}$

Total compressive force: $F_{c.y.2} := \alpha_{R.S}\left(\frac{x_{y.2}}{d - x_{y.2}} \cdot \varepsilon_{sy}\right) \cdot f_{cd} \cdot b \cdot x_{y.2} = 34.14\ \boldsymbol{kN}$

Check that ΔF_2 =0:

$\Delta F_2 := F_{c.y.2} - F_{T.y.2} = \left(5.97 \cdot 10^{-3}\right)\ \boldsymbol{kN}$ Close to = 0

Calculation of strains:

$$\varepsilon_{cc.y.2} := \frac{x_{y.2}}{d - x_{y.2}} \cdot \varepsilon_{sy} = 5.26 \cdot 10^{-4} \qquad \varepsilon'_{sy.2} := \frac{d' - x_{y.2}}{x_{y.2}} \cdot \varepsilon_{cc.y.2} = 2.88 \cdot 10^{-4}$$

$\varepsilon_{cc.y.2} < \varepsilon_{c2} = 2 \cdot 10^{-3}$

Calculation of moment and load at yielding:

$\alpha_{R.y.2} := \alpha_{R.S}\left(\varepsilon_{cc.y.2}\right) = 0.24$ $\qquad \beta_{R.y.2} := \beta_{R.S}\left(\varepsilon_{cc.y.2}\right) = 0.34$

$$M_{y.2} := \alpha_{R.y.2} \cdot f_{cd} \cdot b \cdot x_{y.2} \cdot \left(d - \beta_{R.y.2} \cdot x_{y.2}\right) - \sigma_s\left(\frac{d' - x_{y.2}}{x_{y.2}} \cdot \varepsilon_{cc.y.2}\right) \cdot A'_s \cdot \left(d - d'\right) = 4.77\ \textit{kN} \cdot \textit{m}$$

$$M_{y.2.red} := M_{y.2} - M_g = 4.36\ \textit{kN} \cdot \textit{m}$$

$$F_{y.3.with} := \frac{4 \cdot M_{y.2.red}}{L} = 6.7\ \textit{kN}$$

$$F_{y.4.with} := \frac{M_{y.2.red}}{L_F} = 4.36\ \textit{kN}$$

$$F_{y.4.with.tot} := 2 \cdot F_{y.4.with} = 8.71\ \textit{kN}$$

Determination of stresses in the reinforcement bars:

Top reinforcement: $\sigma'_{s.y.2} := \sigma_s\left(\varepsilon'_{sy.2}\right) = 57.57\ \textit{MPa}$

Bottom reinforcement: $\sigma_{s.y.2} := \sigma_s\left(\varepsilon_{sy}\right) = 546\ \textit{MPa}$

Curvature at yielding: $\varphi_{y.2} := \frac{\varepsilon_{sy}}{d - x_{y.2}} = 0.02\ \frac{1}{\textit{m}}$

Shear capacity of reinforced concrete beam

Indata

Tensile strength: $f_{ctm} = 3.91\ \textit{MPa}$ 5%-fractile tensile strength: $f_{ctk0.05} = 2.74\ \textit{MPa}$

Factor: $\kappa_V := 1$ Partial design factor: $\gamma_c := 1$

$$\tau_{Rd} := 0.25 \cdot \frac{f_{ctk0.05}}{\gamma_c} = 0.68\ \textit{MPa}$$

Tensile reinforcement ratio:

Area of tensile reinforcement: $A_s = 56.55\ \textit{mm}^2$ $\rho_1 := \frac{A_s}{b \cdot d} = 3.53 \cdot 10^{-3}$

Calculation:

Design Shear Strength: $f_v := \tau_{Rd} \cdot \kappa_V \cdot \left(1.2 + 40 \cdot \rho_1\right) = 0.92\ \textit{MPa}$

Design Shear Capacity: $V_c := b \cdot d \cdot f_v = 14.69\ \textit{kN}$

Ultimate External Load: $F_{V.c} := 2 \cdot V_c = 29.37\ \textit{kN}$

Summary

Moment and curvature at yielding without consideration of top reinforcement

$M_{y.1.red} = 4.27\ kN \cdot m$ $\quad x_{y.1} = 24.64\ mm$

$F_{y.3.without} = 6.56\ kN$

$F_{y.4.without.tot} = 8.53\ kN$ $\quad \varphi_{y.1} = 0.02\ \frac{1}{m}$

Moment and curvature at yielding considering both top and bottom reinforcement

$M_{y.2.red} = 4.36\ kN \cdot m$ $\quad x_{y.2} = 25.86\ mm$

$F_{y.3.with} = 6.7\ kN$

$F_{y.4.with.tot} = 8.71\ kN$ $\quad \varphi_{y.2} = 0.02\ \frac{1}{m}$

Load Capacity at Ultimate State without consideration of top reinforcement

$M_{u.1.red} = 5.16\ kN \cdot m$ $\quad x_1 = 8.31\ mm$

$F_{u.3.without} = 7.94\ kN$

$F_{u.4.without.tot} = 10.32\ kN$ $\quad \varphi_{u.1} = 0.36\ \frac{1}{m}$

Load Capacity at Ultimate State considering both top and bottom reinforcement

$M_{u.2.red} = 5.76\ kN \cdot m$ $\quad x_2 = 15.03\ mm$

$F_{u.3.with} = 8.86\ kN$

$F_{u.4.with.tot} = 11.51\ kN$ $\quad \varphi_{u.2} = 0.2\ \frac{1}{m}$

Increase in load capacity if top reinforcement is considered:

$$\frac{F_{u.3.with} - F_{u.3.without}}{F_{u.3.without}} = 11.583\%$$

Shear capacity

$V_c = 14.69\ kN$

$F_{V.c} = 29.37\ kN$

$F_{V.c} = 29.37\ kN > F_{u.4.with.tot} = 11.51\ kN$

Shear capacity is larger than the load capacity. The dominant failure mode is bending failure.

Theoretical Load vs Deformation Relationship

Determination of Cracking Moment and Cracking Curvature:

Modular ratio: $\alpha_s := \frac{E_{sm}}{E_{cm}} = 5.45$

Moment of inertia in State I: $I_I := \frac{b \cdot h^3}{12} + (\alpha_s - 1) \cdot 2 \cdot n \cdot A_{bar} \cdot \left(d - \frac{h}{2}\right)^2 = \left(6.85 \cdot 10^7\right)\ mm^4$

Cracking moment: $M_{cr} := \frac{f_{ct.fl} \cdot I_I}{\frac{h}{2}} = 3.21\ kN \cdot m$

Reduced cracking moment: $M_{cr.red} := M_{cr} - M_g = 2.79\ kN \cdot m$

Cracking force: $F_{cr.3} := \frac{4\ M_{cr.red}}{L} = 4.3\ kN$

$F_{cr.4} := \frac{M_{cr.red}}{L_F} = 2.79\ kN$ $F_{cr.4.tot} := 2 \cdot F_{cr.4} = 5.59\ kN$

Determination of Moment of Inertia in State II

Calculation of position of neutral axis:

Consider first moment of area around the neutral axis:

$\frac{b \cdot x_{II}^{\ 2}}{2} + (\alpha_s - 1) \cdot A'_s \cdot (x_{II} - d') = \alpha_s \cdot A_s \cdot (d - x_{II})$

Initial assumption: $x_{II} := 35\ mm$

$x_{II} := \mathbf{root}\left(\frac{b \cdot x_{II}^{\ 2}}{2} - \alpha_s \cdot A'_s \cdot (d' - x_{II}) - \alpha_s \cdot A_s \cdot (d - x_{II}), x_{II}\right)$

$x_{II} = 0.03\ m$

Moment of inertia:

$I_{II} := \frac{b \cdot x_{II}^{\ 3}}{3} + \alpha_s \cdot A'_s \cdot (d' - x_{II})^2 + \alpha_s \cdot A_s \cdot (d - x_{II})^2$

$I_{II} = \left(6.14 \cdot 10^{-6}\right)\ m^4$

Load-Deformation plot

Determination of equivalent stiffness

Stiffness in State I 3-point bending :

$$K_{I.3} := \frac{48 \cdot E_{cm} \cdot I_I}{L^3} = 6.86 \ \frac{kN}{mm}$$

Stiffness in State II 3-point bending :

$$K_{II.3} := \frac{48 \cdot E_{cm} \cdot I_{II}}{L^3} = 0.62 \ \frac{kN}{mm}$$

Stiffness in State I 4-point bending :

$$K_{I.4} := \frac{6 \cdot E_{cm} \cdot I_I}{{L_F}^2 \cdot L \cdot \left(3 - \frac{4 \cdot L_F}{L}\right)} = 3.97 \ \frac{kN}{mm}$$

Stiffness in State II 4-point bending :

$$K_{II.4} := \frac{6 \cdot E_{cm} \cdot I_{II}}{{L_F}^2 \cdot L \cdot \left(3 - \frac{4 \cdot L_F}{L}\right)} = 0.36 \ \frac{kN}{mm}$$

Deformation considering only State II until ultimate load

Peak load:

$$F_{u.3.with} = 8.86 \ kN$$

$$F_{u.4.with.tot} = 11.51 \ kN$$

Deflection at peak load:

$$u_{II.3} := \frac{F_{u.3.with}}{K_{II.3}} = 14.4 \ mm$$

$$u_{II.4} := \frac{F_{u.4.with.tot}}{K_{II.4}} = 32.38 \ mm$$

Deformation vector

$$u := 0 \ mm, 0.01 \ mm .. 60 \ mm$$

Load as a function of displacement:

$$Force.3.b(u) := \begin{cases} u \cdot K_{II.3} & \text{if } u < u_{II.3} \\ F_{u.3.with} & \text{else if } u > u_{II.3} \end{cases}$$

$$Force.4.b(u) := \begin{cases} u \cdot K_{II.4} & \text{if } u < u_{II.4} \\ F_{u.4.with.tot} & \text{else if } u > u_{II.4} \end{cases}$$

Deformation considering State I and State II

Cracking load:

$F_{cr.3} = 4.3\ kN$ $F_{cr.4.tot} = 5.59\ kN$

Deflection when cracking occurs:

$u_{cr.3} := \frac{F_{cr.3}}{K_{I.3}} = 0.63\ mm$ $u_{cr.4} := \frac{F_{cr.4.tot}}{K_{I.4}} = 1.41\ mm$

Peak load: $F_{u.3.with} = 8.86\ kN$ Deflection at peak load: $u_{II.3} = 14.4\ mm$

$F_{u.4.with} = 5.76\ kN$ $u_{II.4} = 32.38\ mm$

Stiffness between cracking and yielding: $K_{cy.3} := \frac{F_{u.3.with} - F_{cr.3}}{u_{II.3} - u_{cr.3}} = 0.33\ \frac{kN}{mm}$

$K_{cy.4} := \frac{F_{u.4.with.tot} - F_{cr.4.tot}}{u_{II.4} - u_{cr.4}} = 0.19\ \frac{kN}{mm}$

Load as a function of displacement:

$$Force.3.a(u) := \begin{cases} u \cdot K_{I.3} & \text{if } u < u_{cr.3} \\ F_{u.3.with} & \text{else if } u > u_{II.3} \\ F_{cr.3} + (u - u_{cr.3}) \cdot K_{cy.3} & \text{else if } u > u_{cr.3} \end{cases}$$

$$Force.4.a(u) := \begin{cases} u \cdot K_{I.4} & \text{if } u < u_{cr.4} \\ F_{u.4.with.tot} & \text{else if } u > u_{II.4} \\ F_{cr.4.tot} + (u - u_{cr.4}) \cdot K_{cy.4} & \text{else if } u > u_{cr.4} \end{cases}$$

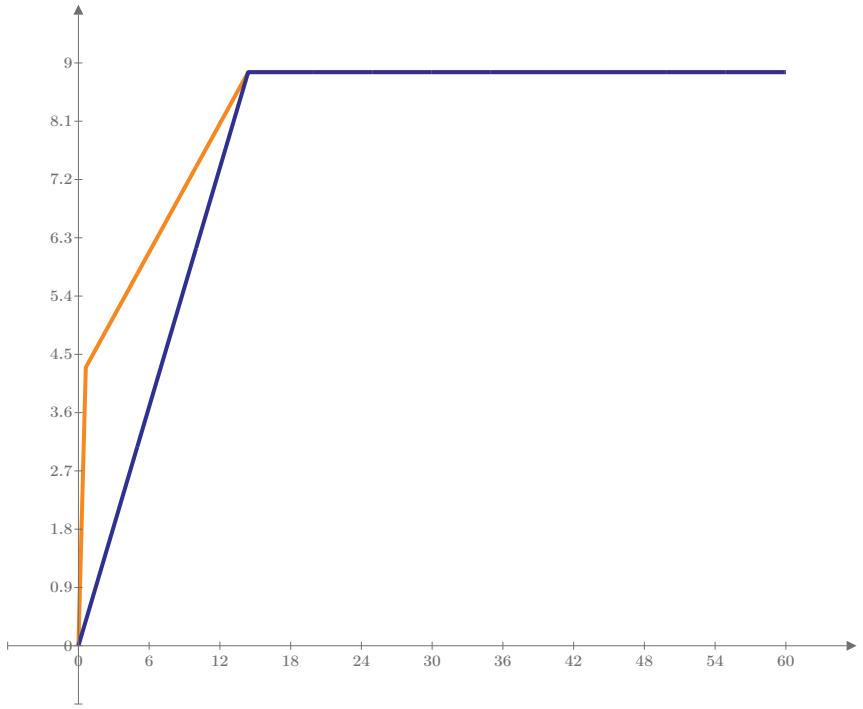

$u\ \ (mm)$

$Force.3.a(u)\ \ (kN)$

$Force.3.b(u)\ \ (kN)$

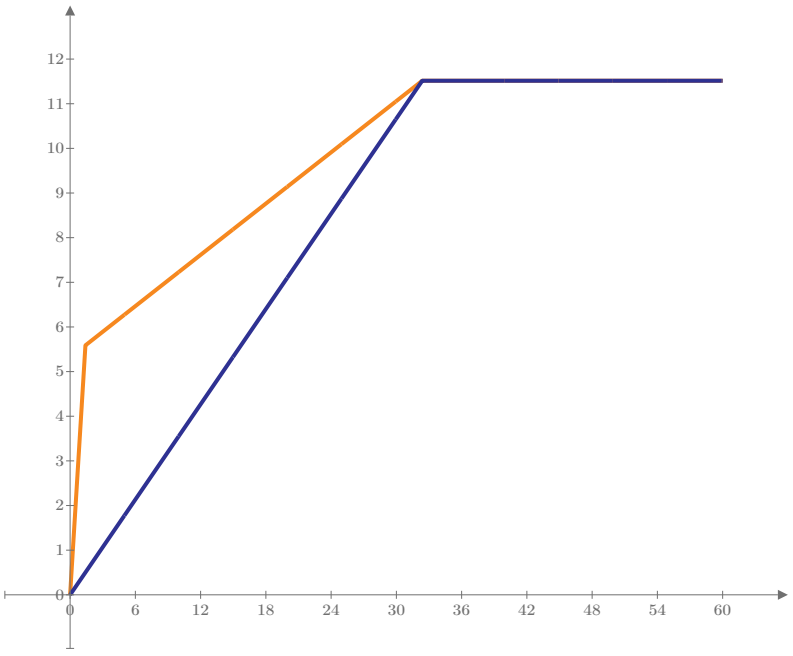

$u\ \ (mm)$

$Force.4.a(u)\ \ (kN)$

$Force.4.b(u)\ \ (kN)$

Prediction of Plastic Rotational Capacity

The plastic rotational capacity of a simply-supported reinforced concrete beam is to be determine according to different equations.

$d = 0.16\ m$ $\quad l_0 := \frac{L}{2} = 1.3\ m$ $\quad \varepsilon_{s.p} := 0.03$

Distance to critical section from support for 3-point and 4-point:

Rotation Capacity According to Eurocode 2

Determine allowable rotation for reference beam (λ = 3):

$x_u := x_2 = (1.503 \cdot 10)\ mm$ $\quad \frac{x_u}{d} = 0.0939$

$$\theta_{pl.C} := \begin{cases} \left(206.25 \cdot \frac{x_u}{d} + 17\right) \cdot 10^{-3} & \text{if } \frac{x_u}{d} \le 0.080 \\ \left(-70.270 \cdot \frac{x_u}{d} + 39.122\right) \cdot 10^{-3} & \text{else if } \frac{x_u}{d} > 0.080 \end{cases}$$

$$\theta_{pl.B} := \begin{cases} \left(42.593 \cdot \frac{x_u}{d} + 7.3\right) \cdot 10^{-3} & \text{if } \frac{x_u}{d} \le 0.162 \\ \left(-30.556 \cdot \frac{x_u}{d} + 19.15\right) \cdot 10^{-3} & \text{else if } \frac{x_u}{d} > 0.162 \end{cases}$$

$\theta_{pl.C} = 0.0325$ $\quad \theta_{pl.B} = 0.0113$

Rotation capacity from the chart:

$\theta_{total.EC2.R} := \theta_{pl.B}$ Class B

Correction for different values of shear slenderness:

$\lambda := \frac{l_0}{d} = 8.13$ $\quad \kappa_\lambda := \sqrt{\frac{\lambda}{3}} = 1.65$

$\theta_{total.EC2} := \kappa_\lambda \cdot \theta_{total.EC2.R} = \left(1.86 \cdot 10^{-2}\right)\ rad$

Consider: $\theta_{total.EC2} = 2 \cdot \theta_{pl.EC2}$

Rotational capacity according to Eurocode 2:

$\theta_{pl.EC2} := \frac{\theta_{total.EC2}}{2} = \left(9.3 \cdot 10^{-3}\right)\ rad$ $\quad u_{pl.EC2} := \theta_{pl.EC2} \cdot l_0 = 12.09\ mm$

MSB

$\theta_{Rd.MSB} := 2 \cdot \theta_{pl.EC2} = 0.019$ **rad**

$u_{pl.MSB} := \theta_{Rd.MSB} \cdot l_0 = 24.18$ **mm**

BK25

$\varepsilon_{s.1} := \varepsilon_{su} \cdot 0.4 = 0.01$

Plastic hinge over the support 3-point bending: $l_{p.Bk25.s.3} := 0.5 \cdot d + 0.1 \cdot l_0 = 210$ **mm**

Critical mechanical reinforcement ratio: $\omega_{s.crit} := \frac{0.8 \cdot \varepsilon_{cu}}{\varepsilon_{cu} + \varepsilon_{s.1}} = 0.16$ $\omega_s < \omega_{s.crit}$

Mechanical reinforcement ratio: $\omega_s := \frac{A_s}{b \cdot d} \cdot \frac{f_{ym}}{f_{cm}} = 0.0351$ Rupture of reinforcement dominant failure mode

Plastic rotation over support:

Crushing of concrete 3-point bending: $\theta_{pl.Bk25.s.1} := \frac{0.4 \cdot \varepsilon_{cu}}{\omega_s} \left(1 + 0.1 \cdot \frac{L}{d}\right) = 0.09$ **rad**

Rupture of reinforcement 3-point bending : $\theta_{pl.Bk25.s.2} := \frac{0.4 \cdot \varepsilon_{s.1}}{0.8 - \omega_s} \left(1 + 0.1 \cdot \frac{L}{d}\right) = \left(1.59 \cdot 10^{-2}\right)$ **rad**

$\theta_{pl.Bk25.s} := min\left(\theta_{pl.Bk25.s.1}, \theta_{pl.Bk25.s.2}\right) = \left(1.59 \cdot 10^{-2}\right)$ **rad**

Deflection over support:

$u_{pl.Bk25.s} := \theta_{pl.Bk25.s} \cdot l_0 = 20.7$ **mm**

ABC-method

Material properties

$f_{cc} := f_{cm}$ $\quad f_{su} := f_t$ $\quad \varepsilon_{cu} = 3.01 \cdot 10^{-3}$ $\quad \varepsilon_{su} = 2.9 \cdot 10^{-2}$

$f_{st} := f_{yd}$ $\quad E_s := E_{sm}$ $\quad \varepsilon_s := \frac{f_{yd}}{E_{sm}} = 2.73 \cdot 10^{-3}$

Without top reinforcement and stirrups

$\omega_v := 0$ No shear reinforcement

$\omega'_s := 0$ top reinforcement is subjected to tensile force

$\omega_s = 0.04$

$\omega_{bal} := \frac{0.8 \cdot \varepsilon_{cu}}{\varepsilon_{cu} + \varepsilon_s} = 0.42$

$A := 1 + 0.6 \cdot \omega_v + 1.7 \cdot \omega'_s - 1.4 \cdot \frac{\omega_s}{\omega_{bal}} = 0.88$ $\quad$ 0.05≤A ≤2.30

$B := 0.6$

$AB := min(A \cdot B, 0.5) = 0.5$

$C := 7 \cdot \frac{l_0}{d} = 56.88$

$\theta_{pl.ABC} := A \cdot B \cdot C \cdot 10^{-3} = (3.01 \cdot 10^{-2})$ ***rad*** $\quad u_{pl.ABC} := \theta_{pl.ABC} \cdot l_0 = 39.17$ ***mm***

With top reinforcement

$\omega_{v2} := 0$ No shear reinforcement

$\omega'_{s2} := \frac{A'_s}{b \cdot d} \cdot \frac{f_{st}}{f_{cc}} = 3.51 \cdot 10^{-2}$ top reinforcement is subjected to compression force

$\omega_{s2} := \frac{A_s}{b \cdot d} \cdot \frac{f_{st}}{f_{cc}} = 0.04$ $\quad \omega_{bal2} := \frac{0.8 \cdot \varepsilon_{cu}}{\varepsilon_{cu} + \varepsilon_s} = 0.42$

$A_2 := 1 + 0.6 \cdot \omega_{v2} + 1.7 \cdot \omega'_{s2} - 1.4 \cdot \frac{\omega_{s2}}{\omega_{bal}} = 0.94$ $\quad$ 0.05≤ A_2 ≤2.30

$B_2 := 1$

$A_2 B_2 := min(A_2 \cdot B_2, 0.5) = 0.5$

$C = 56.88$

$\theta_{pl.ABC.with} := A_2 \cdot B_2 \cdot C \cdot 10^{-3} = 0.054$ ***rad*** $\quad u_{pl.ABC.with} := \theta_{pl.ABC.with} \cdot l_0 = 69.69$ ***mm***

Summary of plastic rotation

Eurocode 2

$\theta_{pl.EC2} = \left(9.3 \cdot 10^{-3}\right)\ rad$ $u_{pl.EC2} = 12.09\ mm$

MSB

$\theta_{Rd.MSB} = \left(1.86 \cdot 10^{-2}\right)\ rad$ $u_{pl.MSB} = 24.18\ mm$

BK25

$\theta_{pl.Bk25.s} = \left(1.59 \cdot 10^{-2}\right)\ rad$ $u_{pl.Bk25.s} = 20.7\ mm$

ABC-method

Without top reinforcement

$\theta_{pl.ABC} = \left(3.01 \cdot 10^{-2}\right)\ rad$ $u_{pl.ABC} = 39.17\ mm$

With top reinforcement

$\theta_{pl.ABC.with} = \left(5.36 \cdot 10^{-2}\right)\ rad$ $u_{pl.ABC.with} = 69.69\ mm$

Internal work (dynamic part)

Indata

Width: $b = 0.1\ m$
Height: $h = 0.2\ m$
Length: $L = 2.6\ m$
Desnity: $\rho = \left(2.5 \cdot 10^3\right)\ \frac{kg}{m^3}$

Initial theoretical velocities of drop-weight $v_0 := 9.9\ \frac{m}{s}$

Transformation factor for beam: $\kappa_{mf} := 0.333$

Mass of beam: $m_b := b \cdot h \cdot L \cdot \rho = 130\ kg$

Number of impacts:

Drop-weight [10kg]: $m_{w10} := 10\ kg$ $n_{\phi 6} := 4$

Drop-weight [20kg]: $m_{w20} := 20\ kg$ $n_{\phi 8} := 2$

Drop-weight [40kg]: $m_{w40} := 40\ kg$ $n_{\phi 10} := 1$

Kinetic energy of drop-weight:

$$E_{k.0.a} := \frac{m_{w10} \cdot {v_0}^2}{2} = 490.05\ J$$

$$E_{k.0.b} := \frac{m_{w20} \cdot {v_0}^2}{2} = 980.1\ J$$

$$E_{k.0.c} := \frac{m_{w40} \cdot {v_0}^2}{2} = 1960.2\ J$$

External work on the beam:

$$W_{e.imp.10} := \frac{m_{w10}}{m_{w10} + m_b \cdot \kappa_{mf}} \cdot E_{k.0.a} = 91.96\ J$$

$$W_{e.imp.20} := \frac{m_{w20}}{m_{w20} + m_b \cdot \kappa_{mf}} \cdot E_{k.0.b} = 309.72\ J$$

$$W_{e.imp.40} := \frac{m_{w40}}{m_{w40} + m_b \cdot \kappa_{mf}} \cdot E_{k.0.c} = 941.39\ J$$

Total external work on the beam after *n* impacts:

$$W_{e.imp.10.tot} := n_{\phi 6} \cdot W_{e.imp.10} = 367.84\ J$$

$$W_{e.imp.20.tot} := n_{\phi 8} \cdot W_{e.imp.20} = 619.43\ J$$

$$W_{e.imp.40.tot} := n_{\phi 10} \cdot W_{e.imp.40} = 941.39\ J$$

ARCHITECTURE AND CIVIL ENGINEERING
DIVISION OF STRUCTURAL ENGINEERING
CHALMERS UNIVERSITY OF TECHNOLOGY
Gothenburg, Sweden 2023
www.chalmers.se

CHALMERS
UNIVERSITY OF TECHNOLOGY